2017

Evaluation, Analysis, and Application of HF Radar Wave and Current Measurements

Lopez, Guiomar

Evaluation, Analysis, and Application of HF Radar Wave and Current Measurements

by

Guiomar Lopez

A thesis submitted to Plymouth University in partial fulfilment for

the degree of

DOCTOR OF PHILOSOPHY

School of Marine Science and Engineering

Faculty of Science and Engineering

April 2017

This copy of the thesis has been supplied on condition that anyone who consults it is understood to recognise that its copyright rests with its author and that no quotation from the thesis and no information derived from it may be published without the author's prior consent.

EVALUATION, ANALYSIS, AND APPLICATION OF HF RADAR WAVE AND CURRENT MEASUREMENTS

Guiomar Lopez

ABSTRACT

This study investigates the accuracy of the wave products retrieved by a 12-MHz high-frequency (HF) phased-array radar, and establishes their potential to characterise wave-current interactions. The two stations composing the system were deployed in 2011 to overlook the Wave Hub, a test site for marine renewable energy devices located on the south-western coast of the United Kingdom. The system was conceived and configured to reduce the inaccuracies introduced by short time averaging and minimal overlap between stations, both associated with the most traditional HF radar deployments, whose primary activity is current measurement. Wave spectra were retrieved by two independent inversion algorithms, which were evaluated both independently and relative to each other. This process helped determining the errors associated to the algorithm used, and differentiated them from those inherent to the radar technology itself.

The first method investigated was a semi-empirical algorithm distributed with Wellen Radars (WERA), which was calibrated using in situ measurements collected within the radar footprint. Evaluated through comparison against measurements acquired by three in situ devices, the results revealed estimates of significant wave height with biases below 9 cm, Pearson correlations higher than 0.9, and RMS errors that range from 29 to 44 cm. The relative error of wave energy period comparisons was within 10% for periods between 8 and 13 s, while both under- and overestimations were observed above and below that range, respectively. The validation demonstrated that when locally calibrated, the algorithm

performs better than in its original form in all metrics considered. Observed discrepancies were mainly attributable to single-site estimations, antenna sidelobes, and the effect of the second-harmonic peaks of the Doppler spectrum.

As opposed to the semi-empirical inversion, the second method evaluated in this work provides estimates of the full directional spectrum. Compared against the in situ measurements, the radar spectra were more spread over frequencies and directions, and had a lower energy content at the peak of the spectrum. In terms of parameter estimation, this was generally translated in a slight underestimation of wave periods, but accurate estimates of significant wave heights. Pearson correlations between these parameters and the in situ measurements for the bulk of the spectrum were higher than 0.9, and both types of measurements resulted in similar standard deviations. The inversion algorithm showed a high skill estimating mean wave directions, which revealed linear correlations higher than 0.8, when compared to the in situ devices. Overall, the inversion algorithm has shown to be capable of providing accurate estimates of directional spectra and the parameters derived from them, and at present the main drawback of the method is the data return, which due to the high data quality requirements of the algorithm, did not exceed 55% over the 8-month period studied here.

In the second part of this work, the validated measurements were examined to determine their ability to reproduce the effects of wave-current interactions. The fine structure of the surface current was first evaluated, and revealed a circulation dominated by tides. The residual flow was seen to respond to the wind, as well as to the stratification present in the area during the spring and summer months. These data were then used to assess their contribution to wave refraction over the radar domain. The results show modulations in the wave phase parameters, which resulted from both the temporal and spatial derivatives of the surface current velocities.

The evaluation of HF radar wave measurements provided in this work has shown that, properly configured, this technology can produce accurate estimates of several statistical descriptors of the wave field. Together with the highly accurate surface currents also measured by this device, the spatial wave data obtained has proved to have great potential for studying wave-current interactions; a skill that can be of support to coastal wave modelling.

AUTHOR'S DECLARATION

At no time during the registration for the degree of Doctor of Philosophy has the author been registered for any other university award without prior agreement of the graduate committee. Work submitted for this research degree at Plymouth University has not formed part of any other degree either at Plymouth University of at another establishment. This studentship was funded through contributions from the EU project MARINET (Marine Renewables Infrastructure Network for Emerging Energy Technologies), and the School of Marine Science and Engineering at Plymouth University.

Relevant scientific seminars and conferences were regularly attended at which work from this project was often presented. The author attended specialist courses as part of research training. Work from the project and collaborations established during this project lead to a number of manuscripts that will be or have been submitted for peer review publication.

Word count of the main body of the thesis: 43 891

Scientific publications

- Lopez G, Conley D, Magagna D and Greaves DM, 2013. Adjusting An Empirical Algorithm for Extracting Wave Height from HF Radar Measurements at the Wave Hub. Proceedings of EWTEC 2013, Aalborg, Denmark.

- Lopez G, Conley DC and Greaves DM, 2016. Calibration, Validation, and Analysis of an Empirical Algorithm for the Retrieval of Wave Spectra from HF Radar Sea Echo. J. Atmos. Oceanic Technol., 33, 245261, doi: 10.1175/JTECH-D-15-0159.1.

Oral Presentations

- Spatial Validation of HF Radar Wave Measurements in the Northern Coast of Cornwall. International Coastal Symposium, Plymouth April 2013.

- Spatial variability of ocean waves from in-situ measurements. Ashton et al. (2013) paper discussion. Coastal Processes Research Group Meeting May 2013.

- Adjusting an empirical algorithm for extracting wave height from HF radar measurements at the Wave Hub. European Wave and Tidal Energy Conference, Aalborg, Denmark September 2013.

- Measuring waves with HF radar. Plymouth Marine Science and Education Foundation, Making Waves 2013 - Maritime Conference for PhD Students and early career scientists. Plymouth Marine Laboratory, Plymouth Nov 2013.

- Investigation of HF radar as a wave assessment tool. PRIMaRE conference. Plymouth University, Plymouth June 2014.

Poster Presentations

- Spatial and temporal validation of a refined empirical algorithm to derive wave spectra from HF radar measurements. Ocean Sciences Meeting, Honolulu, Hawaii February 2014.

- Investigation of HF radar as a wave assessment tool. PRIMaRE conference. Plymouth University, Plymouth June 2014.

Workshops Attended

- WERA Operators Seminar, Kaltenkirchen, Germany Dec 2013.

- ROWH. University of Hawaii, Manoa, USA February 2014.

- Radio Oceanography Workshop, Savannah, Georgia, USA May 2014.

Contribution to Reports

- Processing and analysis of HF radar measurements of currents and sea states in the Iroise and Celtic Seas. MERIFIC deliverable 3.1.4.

- Non-intrusive wave field measurement. MARINET deliverable D4

Signed:..

Date:..

Contents

List of Figures

List of Tables

Acknowledgements

Firstly, I would like to thank my supervisors Dr. Daniel Conley and Prof. Deborah Greaves for giving me the opportunity of doing this PhD. Special thanks to Daniel for his invaluable guidance, patience, and encouragement. Without your ideas, and excitement for this research, I would not have finished this work. Thank you.

This thesis would not have been possible without the support from the European project MaRINET, and the School of Marine Science and Engineering at Plymouth University, which have jointly fund this research.

I am indebted to Megan Sheridan, Davide Magagna and Peter Ganderton for their involvement in the deployment of the devices which provided the data underpinning this research. I would also like to show my appreciation to Andrea, Erwin, Olivier, Robin, and Liam for their hard work in "fighting" the cow damage at Pendeen. Thank you to all my office mates who have been there for the occasional distraction, and the sometimes very much needed visit to the pub. Thanks also to my friends outside the office, both in Plymouth and Asturias, who provided the support, joy, and distractions essential to maintain my mental sanity.

Last, but definitely not least, I would like to thank my parents. Without your encouragement and continuous support, I certainly wouldn't be writing this now. Dedicating this thesis to you is the very least I can do to give back a tiny part of what you have given, and continue to give me every day of my life. Thank you from the bottom of my heart.

Chapter 1

Introduction

1.1 Motivation

Knowledge of the offshore and coastal wave climate is crucial for ensuring the successful outcome of several human activities such as marine operations, coastal defence, or marine energy extraction. Most of the projects associated to these activities require high quality data, with good temporal and spatial resolution, at several stages of their development. One of the preferred methods used to meet the wave data demands is the in situ measurement conducted with wave buoys, which are probably the most used and trusted method for wave measurement. However, they only provide information at a single point, and alternative techniques have to be used to provide spatial coverage. This can be achieved using remote sensing techniques such as Synthetic Aperture Radar (SAR), which has emerged as the main alternative to fill in the spatial gap in wave observation (Li and Saulter, 2012). However, the temporal resolution of the satellite products tends to be sporadic (Venugopal et al., 2011). As a result, all those research questions requiring spatial wave information in order to be answered, have come to rely on wave model results, which in spite of significant improvements over the

past years, are sometimes limited by a lack of good-quality boundary condition data (offshore directional waves, winds, currents and bathymetry) (Folley et al., 2012), and are always constrained by low spatial resolution in either their computational grid, boundary conditions, or both. Furthermore, in coastal areas where the physical processes caused by the interaction between waves, currents and the bottom become important, the spatial wave properties are strongly variable, and model uncertainty increases (Lehner et al., 2012). However, in such a dynamic environment the knowledge of these complex physical processes and their interactions constitutes an essential piece of information for most activities. This is particularly true for marine renewable energy (MRE) projects, to which surface currents, wind, or ocean waves do not only constitute the resource to be exploited, but also factors affecting the survivability and performance of the devices deployed in the marine environment. Therefore, an in-depth knowledge of the met-ocean conditions at high spatio-temporal resolution, is not just needed for resource assessment (Boudiere et al., 2013), but essential for all the stages of the project development (Venugopal et al., 2011).

Among all the existing remote sensing techniques able to produce this type of spatial data, the only capable of providing a relatively large coverage with high temporal and spatial resolution is HF radar, which could therefore play an essential role in monitoring surface currents and waves for several applications, including MRE (Wyatt, 2007, 2012). This technology has the capability of measuring surface currents, waves and wind direction from locations up to 200 km offshore, depending on the radar's operating frequency and geometry, and the variable being measured. Results are provided in near-real time with a spatial resolution that depends on the allocated bandwidth and antenna design, and varies from 250 m to 15 km (Wyatt et al., 2011). This kind of information could be extremely useful for marine renewable energy, which would benefit from spatial measurements when assessing the resources, and monitoring the wave energy sites. The near-real time

data provided by this technology can be of assistance to operational activities such as performance assessment, short-term wave forecasting, device tuning, or marine operations. The synoptic measurements of both currents and wave heights would allow near-real-time identification of regions where the combination of the two can pose a hazard to maritime activities (Haus et al., 2006), and also aid the characterization of wave-current interactions, which have been found to play an important role in wave resource estimates (Hashemi and Neill, 2014). Moreover, the assimilation of radar partitioned wave spectra into a wave model has resulted in improvements during a stormy period with turning winds (Waters et al., 2013), and the assimilation of surface currents has been recognised to be useful in correcting the baroclinic oceanic forcings hence improving modelled results (Marmain et al., 2014).

The different data products obtained with HF radar are, however, not equally perceived and accepted within the scientific community. Measured surface currents have gained a strong reputation over the last 40 years, and are considered reliable measurements, which are routinely used for oceanographic studies and operational applications. The strong signal produced by the resonant first-order Bragg waves, together with the simplicity of the relation between their Doppler shift and the velocity of the surface current, provide a robust and reliable HF radar measurement of the latter. On the other hand, the second-order spectrum embodying the information about the wave field is characterized by a weaker signal that can be buried in noise; thus, the inversion is in this case a further constrained problem. In addition, this part of the spectrum arises from non-linear wave interactions that make the interpretation of the radar signal an intricate process not as straightforward as the estimation of surface current radial velocities. Consequently, the inversion of the second-order part of the backscatter spectrum into meaningful wave data is an area of active research, and the validity of the radar wave products is still under scrutiny. Current measurement is therefore the primary activity

of the majority of HF radars installed worldwide, which have accordingly been optimized for this purpose (Voulgaris et al., 2008; Haus, 2007; Haus et al., 2010; Ramos et al., 2009; Savidge et al., 2011). Using data acquired by these systems for wave processing can, however, have negative implications in the extent and quality of the wave estimates, and has probably contributed to delay the acceptance of wave measurements. For example, the substantial alongshore separation between radars, which is sometimes required to maximize coverage for current measurement, can result in a minimal overlap across the short ranges where wave measurements are possible (i.e., Voulgaris et al., 2008). This often entails the use of only one station to obtain wave estimates, which are consequently restricted to non-directional wave products due to the intrinsic direction ambiguity associated with a technique based on radial measurements. Moreover, the integration time for measurements is normally restricted to a few minutes, in order to allow resolution of the rapidly changing conditions sometimes related to surface currents. This implies data samples that are not long enough to reduce sampling variability impacts on wave calculations (Wyatt et al., 2009), and it has been found to result in noisy estimates (Voulgaris et al., 2008). Furthermore, because radar results are derived from an area rather than a point, the differences between these and in situ measurements are foreseen to be larger than those expected from sampling variability. Because the spatial averaging is inherent to the HF radar technique, adjusting the integration time to match that of the in situ instrumentation, is the best alternative to obtain measurements whose variances are as close as possible to those of the point measurements, hence favouring the comparison of the results obtained with the two different approaches.

The credibility of the radar's wave measurements is therefore still not supported by enough data collected by radars adequately configured for such task. Without these data, and their validation against well established wave measuring techniques, it is not possible to identify the appropriate error bounds for the HF radar

wave measurements, and advance their operational use.

1.2   Objectives

In response to the needs identified on the previous section, an HF radar system was conceived and deployed in 2011 with the main aim of acquiring wave information over an area designed for testing wave energy devices. The arrangement of the two radars that compose the system is such that it maximizes their beam overlap across the ranges where wave measurements are possible, and the data collection was adjusted to periods similar to those commonly used by other wave measurement techniques. This sampling scheme is better suited for wave measurement (Wyatt et al., 2009), and the products obtained with this system are expected to provide a better idea of the HF radar capabilities for such purpose. Validation of the results against in situ measurements will seek to demonstrate whether that expectation is met.

This work is divided into three main parts. The primary research aim of the first two is to establish the accuracy of HF radar wave measurements. Evaluation of two different methods for wave inversion will help to determine the errors associated to the algorithm used, and differentiate them from those inherent to the radar technology itself. Additionally, the assessment of several months of measurements collected at three different locations within the radar coverage will provide information about their spatio-temporal reliability. On the third part of the thesis, the previously analysed wave data is used in combination with surface current measurements, also obtained with HF radar, to study the hydrodynamic conditions over the measurement area, and aims to shed light on the potential benefits of using these data to further the understanding of wave-current interactions.

The specific objectives of the study can be summarised as:

– Examine the accuracy of HF radar measurements using data collected at different ranges and azimuths over the radar's field of view.

– Determine errors associated with two existing wave inversion algorithms.

– Determine the utility of HF radar in studying wave-current interactions.

In order to meet the above objectives, the analyses conducted in this work will seek to answer the following research questions:

• Is the radar configuration adequate for wave measurement?

• Which are the errors associated to the inversion algorithm used, and which are independent to the method, but inherent to the HF radar technique itself?

• How do these errors affect the results? Can these be clearly identified?

• What is the temporal and spatial accuracy of the measurements?

• How can HF radar measurements contribute to the study of wave-current interactions?

1.3 Outline of the thesis

Chapter 2 first provides an introduction to the HF radar technique. The principles that underpin the measurement of sea state are summarised, and the specifics of the type of radar used in this study enumerated. This information is completed with a review of the main techniques used to invert the radar signal into meaningful wave information. A review of intercomparison techniques used to evaluate wave measurements acquired with different sensors is then provided, and followed by documented validations of HF radar wave measurements. An introduction to the

theory of wave-current interactions is then given, and some relevant published works summarised.

In Chapter 3, the various instruments used to collect the data used throughout are described, as are the procedures used to process these data. Various general methods used throughout the rest of the document are also summarised .

Chapter 4 aims to evaluate the in-house algorithm shipped with WERA radars. Due to its semi-empirical nature, this is first calibrated using data collected locally, and the results are then evaluated through comparison against in situ measurements. The accuracy of the one-dimensional spectra obtained, never reported in the literature before, is explored along with the bulk parameters derived from them. Inspection of the errors associated to the effects of the second harmonic peaks of the Doppler spectrum upon the results is also provided.

Chapter 5 focuses on the evaluation of the results obtained with a theoretical inversion algorithm. The literature covering the analysis of its performance is far more extensive than in the previous case, hence the main aim of this chapter is to evaluate whether the sampling scheme of the radars used in this study brings significant improvements to the results.

The aim of Chapter 6 is to compare the two approaches analysed in the previous two chapters using a unified framework, in which only records common to the two methods are evaluated.

Chapter 7 provides an overview of the surface current and wave fields measured by the radar. The two types of measurements are then analysed together with the aim of examining the refractive effects of the former onto the latter.

Chapter 8 provides a summary of the work presented throughout, and examines the main findings.

Chapter 2

Review

The first part of this review introduces the principle behind all oceanographic HF radar measurements, and summarizes some of the techniques that allow obtaining meaningful ocean wave information from radar backscatter. The validation of wave measurements is next discussed. The generalities of data inter-comparison, and the common approaches adopted within the wave science community are first summarised, and an outline of some studies regarding the validation of HF radar wave products is then given. Lastly, the state-of-the-art of wave-current interaction research, and a summary of related studies is provided.

2.1 HF Radar Remote Sensing and Wave Inversion

2.1.1 HF radar systems

High frequency (HF, 3 - 30 MHz) ground wave radars are shore based remote sensing systems that transmit vertically polarised electromagnetic waves, which due to the conductivity of the sea surface propagate long distances with very

little loss. As they travel, the electromagnetic waves interact with the rough sea surface, which acts as a diffraction grating, scattering them in all directions with some scattered back to the radar receivers (Kahma et al., 2005). Crombie (1955) was the first to notice the two dominant peaks in Figure 2.1 while studying a record of radio waves reflected from the sea surface at 13 MHz. He deduced that these were the result of the scattering of the electromagnetic waves off ocean waves with exactly half the radio wavelength, travelling towards and away from the radar. This scattering mechanism was therefore seen to be Bragg scatter, the same phenomenon responsible for the scatter of X-rays in crystals and light rays from diffraction gratings and holograms (Barrick, 1970). Another feature Crombie noticed was that the position of these peaks was symmetrical around the carrier frequency and varied as a function of the square root of the latter (Barrick, 1978). He correctly pointed to the celerity of the moving Bragg waves as the cause for the frequency shift relative to the transmitted frequency. However, the position of the two peaks is always shifted from the theoretical value calculated with the wave dispersion relation, which predicts them to be located at a Doppler frequency equal to,

$$\omega_D = \pm\sqrt{gk_B\tanh(k_Bh)} \tag{2.1}$$

where ω_D is the Doppler frequency of the Bragg peaks, k_B is the wave number of the Bragg waves and g is the acceleration due to gravitational forces.

The wave number of the scattering Bragg wave can be obtained from the Bragg condition, which states that the primary reflections come from waves with half the radio wavelength. Hence,

$$k_B = \frac{2\pi}{\lambda_B} = \frac{4\pi}{\lambda_0} = 2k_0 \tag{2.2}$$

where λ_0 is the transmitted radio wavelength and λ_B is the wavelength of the Bragg scattering waves. The difference between the measured and the theoretical
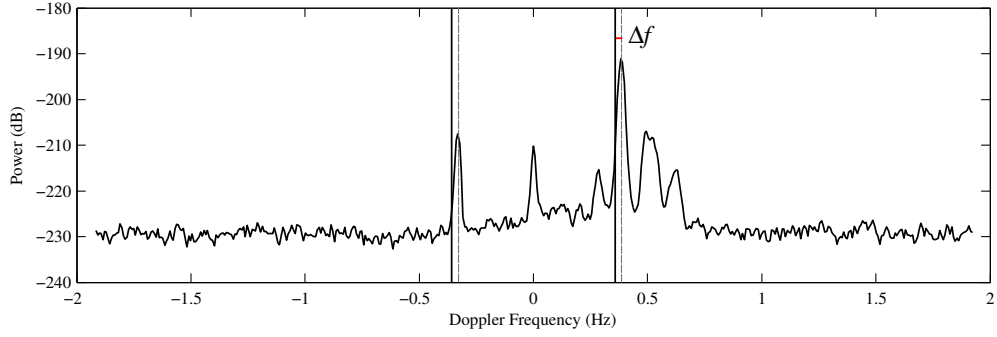
Figure 2.1: Doppler spectrum measured by a HF radar transmitting at 12 MHz. The vertical black lines are the theoretical positions of the receding (negative) and approaching (positive) Bragg waves obtained from Equation 2.1. Dashed lines indicate the measured frequency of Bragg waves, and Δf corresponds to the additional Doppler shift generated by the surface current.

phase velocity is attributed to the radial velocity of the surface current, hence the frequency of the Doppler-shifted signal is,

$$\omega_D = \pm\omega_B - 2k_0 u \tag{2.3}$$

where ω_B is the angular frequency of the Bragg scattering ocean wave, k_0 is the radio wave number and u is the radial component of the current. The sign in front of ω_B depends on the direction of the scattering wave, positive if travelling towards the radar and vice versa. Because u is the only unknown variable on Equation 2.3, this can be used to derive surface current information from HF radar. Information about wind direction is often inferred from the relative height of these two peaks (Heron and Rose, 1986). The rest of the spectrum, consisting of a continuum due to non-linear wave interactions and scattering processes along with a noise floor (Kahma et al., 2005) can be used to extract information about the directional ocean wave spectra and will be explained further in the next section.

About a decade after Crombie's discovery, theoretical studies began to appear and confirmed his empirical observations (i.e. Wait, 1966; Barrick, 1970). This aroused significant interest on using radars on the band of high frequency radio signals to study oceanographic processes and led to the development of the Coastal

Ocean Dynamic Applications Radar (CODAR) (Barrick et al., 1977; Evans and Georges, 1979). The system, developed at NOAA, became the first commercial high frequency radar capable of measuring oceanographic parameters. Since the first CODAR, much research and new developments have resulted in different radar designs with more or less success. The Ocean Surface Current Radar (Prandle, 1987) and PISCES (Shearman and Moorhead, 1988), both developed in the UK, were some of the earliest phased array systems to be commercialized. While the first one is no longer in use, a PISCES system manufactured by Neptune Radar Ltd. has been in operation on the south-west coast of the UK since 1986. In 1995, Klaus-Werner Gurgel developed the WEllen Radar (WERA) at the University of Hamburg (Gurgel et al., 1999a), a design produced to overcome CODARs limitations on wave measurement, which is now produced and commercialized by Helzel Messtechnick GmbH.

The main difference between phased-array systems and CODAR type radars relies on the technique they use to resolve the incident angle of a sea echo (Gurgel et al., 1999b). Using the so-called direction-finding technique, CODAR radars measure the amplitude and phase characteristics of a signal at three receive antennas. To identify the incidence angle of a signal, they use the so-called MUSIC algorithm. With this technique, strong first order Bragg lines from different directions are superimposed onto the weaker second order returns, hence making the extraction of wave information from the latter very difficult. In order to overcome this problem, phased array systems use beam-forming techniques, which permit the digital steering of the radar beam to all defined directions desired, in order to measure scattered returns from a specific patch of the ocean. The effective radar radiation pattern is steered to a particular direction by adding an appropriate phase shift to the signal received at each antenna. Adding up the signals received at all receiving antennas, a spectrum is generated for the desired direction, and the second order part of the Doppler spectrum can be accessed to extract wave information.

With more than 350 systems installed worldwide, CODARs SeaSonde is the leader
HF radar technology, followed by the 47 phased array WERA systems that had
been deployed to date. Nonetheless, as already mentioned, phased array systems
such as WERA are best suited for spatial wave measurement, as the compact
antenna systems of CODAR type require spatial homogeneity in the wave field
over a wide area (Kahma et al., 2005). The majority of the SeaSondes deployed
worldwide are therefore primarily used for current measurement.

2.1.1.1   Wellen Radar

As mentioned before, the HF radar operated by Plymouth University is a WEllen
RAdar (WERA). Drawing extensively on reference to Gurgel et al. (1999a), this
section intends to provide a summary of the characteristics and technical design
of this system that will help to understand how the results are obtained.

WERA was developed within the frame of the European project SCAWVEX (Sur-
face Current and Wave Variability Experiment). It can operate at any frequency
within the range 5-50 MHz, and both phased array beam-forming and direction
finding techniques are supported for azimuthal resolution, allowing for current
mapping and sea state resolving (Gurgel and Antonischki, 1997; Gurgel et al.,
1999a). WERA transmits frequency modulated continuous waves (FMCW) with
the following form,

$$s(t) = \sin \left[2\pi \left(v_0 + \frac{b}{2T}t \right) t \right]$$

(2.4)

where during the chirp period T, the frequency linearly increases from v_0 to $v_0 + b$,
where b is the bandwidth. The received signal is a superposition of HF waves,
which have been backscattered at different distances from the radar,

$$r(t) = \int \alpha(\tau) sin \left[2\pi \left(v_0 + \frac{b}{2T}(t - \tau) \right) (t - \tau) + \phi(\tau) \right] d\tau$$

(2.5)

where τ is the propagation time from the radar to the scattering area and back, and ϕ and α are the signal phase and amplitude, which are assumed to be constant over a chirp. After phase-coherent demodulation, signals are sorted by range, performing a Fourier transform of each chirp. Before this, a window filter is applied to prevent leakage.

The range resolution of these measurements depends on the allocated bandwidth by,

$$r = \frac{c}{2b} \tag{2.6}$$

where c is the speed of light. However, due to the windowing applied with the Fourier Transform the resolution is broadened (Harris, 1978). Therefore, using a Hanning window (which results in a broadening of factor 2) the range resolution would be,

$$r = \frac{c}{b} \tag{2.7}$$

After the above processing, it is possible to know where the received signals have been scattered from in range, but we still need to know their position in azimuth. In phased arrays, the latter is actually not inferred from the signal but rather performed by the radar using beamforming techniques, as discussed earlier. The azimuthal resolution of this beam depends on the aperture, i.e., the length the array by,

$$\frac{\lambda_0}{D} \tag{2.8}$$

where λ_0 is the transmit wavelength and D is the length of the array. Similarly to range resolution, the width of the beam will be broadened due to the use of a windowing function, applied in this case to reduce sidelobes in the antenna pattern (Gurgel et al., 1999b).

2.1.2   Scattering theory

Studies on the wave scattering from random rough surfaces date back to the end
of the 19th century when Rayleigh (1877) studied the scattering of sound waves
from sinusoidal surfaces. In doing so he used perturbation analyses, which allow
finding approximate solutions to complex physical applications by solving simpler
models with a known solution. Rice (1951) further extended this work applying
perturbation theory to solve the scattering of electromagnetic (EM) waves on two-
dimensional randomly rough surfaces. The Rice boundary perturbation approach,
which constitutes the basis for most of the subsequent mathematical formulations
of the HF radar backscatter, is based on an incident plane wave, a perfect conduct-
ing scattering surface and is restricted by the following conditions: 1) the height
of the surface must be small in terms of radio wavelength, 2) surface slopes must
be small, and 3) the impedance of the surface medium must be small in terms of
the free-space wave impedance. Following Rice's theory, Barrick (1972a) devel-
oped a first-order solution for a perturbation analysis of the interaction between
electromagnetic waves and the sea surface, which was represented as a section of
a moving and perfectly conducting surface. The inclusion of time in the descrip-
tion of the random sea surface is accomplished by a Fourier series expansion over
time as well as space. This way, Barrick was able to obtain an expression for the
normalised radar cross-section per unit area per frequency, that is described as a
function of the Doppler frequency as follows,

$$\sigma_1(\omega_D) = 2^6 \pi k_0^4 \sum_{m'=\pm 1} S(-2m'k_0)\delta(\omega - m'\omega_B) \tag{2.9}$$

where σ_1 is the scattering cross-section per unit area and per radian/s bandwidth,
ω_D is the Doppler frequency, m' denotes the sign of the Doppler shift, k_0 is the
incident radar wave number, δ is the impulse function that represents the discrete
Bragg peaks (first-order peaks) and S is the directional wave number spectrum.

According to Equation 2.9, the Doppler spectrum consists of two peaks centred at the transmitted frequency and shifted by an amount dependent on the motion of the ocean waves. However, and as shown in Figure 2.1, the Doppler power spectrum contains a continuum besides the first-order Bragg peaks described by Equation 2.9. It was Hasselmann (1971) who first suggested that this continuum ought to be proportional to the wave height non-directional temporal spectrum. Based on this idea, Barrick (1972b) extended the perturbation analysis to obtain second-order solutions that could explain the continuum surrounding the first-order peaks. He modelled the second-order cross-section as a combination of hydrodynamic nonlinear interactions (hydrodynamic effect) and double scattering (electromagnetic effect). The hydrodynamic second-order scatter results from a single scatter off a second-order ocean wave. This would be the result of the interaction of two fundamental ocean waves with wave vectors k and k', which after vector summation result in a wave whose wavelength is half the radio wavelength and travels along the radar beam. On the other hand, the electromagnetic second order scatter occurs when the incident radar wave is scattered by a first-order ocean wave whose wave vector is k, which is itself scattered again by another first-order ocean wave of wave vector k' (Zhang et al., 2012). Again, the constraint for the second-order scatter to occur is that the resulting vector has to obey the Bragg condition, hence the wavelength of the combined components should match one-half the radar wavelength after vector addition and the direction of the combination should be along the radar beam. But even though the first- and second-order waves have matching wavelengths (obeying the Bragg condition), the wave numbers of the first-order waves are related to their frequencies via the linear dispersion relationship, whereas the second-order waves are not (i.e., for the second order wave with wave vector K, $\omega + \omega' = \sqrt{gk} + \sqrt{gk'} \neq \sqrt{gK}$). According to this, waves of any wavelength may contribute to the electromagnetic and hydrodynamic terms, and consequently the second order continuum contains information about the entire wave directional spectrum.

The expression obtained in Barrick (1972b) for the second-order radar cross-section is,

$$\sigma_2(\omega_D) = 2^6 \pi k_0^4 \sum_{m,m'=\pm 1} \iint_{-\infty}^{\infty} |\Gamma|^2 S(mk)S(m'k')\delta(\omega_D - m\sqrt{gk} - m'\sqrt{gk'})dpdq$$

(2.10)

where m equals ± 1, p and q are the spatial wavenumbers, parallel and perpendicular to the radar beam, respectively, and Γ is a coupling coefficient that accounts for the electromagnetic and hydrodynamic components described above.

2.1.3   Wave inversion algorithms

The early theories summarized in the previous section set the ground for all the methods, both theoretical and empirical, that have been developed to extract ocean wave information from the Doppler power spectrum. Among the theoretical methods, the inversion of the perturbation solution developed by Barrick under different approaches is the most common procedure used to estimate the ocean wave spectrum. On the other hand, empirical algorithms explore relevant relationships between Doppler and ocean wave spectra, which can allow inverting the former into the latter.

2.1.3.1   Theoretical wave inversion

Based on his own theoretical derivations of the first- and second-order cross sections, Barrick (1977b) derived an inversion technique for obtaining the wave height non-directional spectrum. He employed the stronger second-order Doppler sideband divided by a parameterless, dimensionless weighting function. Dividing the product of the latter division by the adjacent first-order spectral energy to remove unknown factors, the non-directional wave height spectrum could be obtained. In

another work from the same year, Barrick (1977a) presents a computerized technique for extracting rms wave height and dominant wave period from HF radar Doppler spectra. He applied two approximations that removed the coupling coefficient and the delta Dirac function from the integral that defines the second order cross section. The result is an expression for the radar rms wave height in terms of the weighted second-order spectral area divided by the first-order area.

After Barrick, several other approaches to the inversion problem have been investigated and published elsewhere (Lipa, 1977; Wyatt, 1990; Howell and Walsh, 1993; Hisaki, 1996; Hashimoto and Tokuda, 1999; Hisaki, 2015). One of the main differences between them lies on whether Equation 2.10 is linearised or not before solving it. Additionally, some schemes use the action balance equation under the assumption of stationarity together with Equation 2.10 (de Valk et al., 1999; Hisaki, 2015), and allow estimation of the directional spectrum from one radar only. Of all methods, Wyatt's (1990), distributed as a software package by Seaview Sensing Ltd. is probably among those accumulating the largest number of publications, as well as the focus of part of this thesis. The algorithm, described in detail in Wyatt (1990) and Atanga and Wyatt (1997), is a linearising method based on an iterative scheme initialized with a Pierson-Moskovitz spectrum and a cardioid model for the directional distribution, both of which are defined using information directly extracted from the radar-measured Doppler spectrum (Wyatt et al., 1985). This initial guess of the ocean wave spectrum is then used to derive a Doppler spectrum by integration of the equation relating the two. The integrated result is then compared to that measured, and if the spectra differ from each other the initial estimate of the ocean wave spectrum is adjusted in the following iteration until a certain convergence criterion, based in the difference between the calculated and measured Doppler spectra, is met (Wyatt, 2000).

2.1.3.2   Empirical and semi-empirical algorithms

A different approach to the inversion consists of deriving empirical expressions
relating the backscatter spectrum to the equivalent ocean wave spectrum or some
of its summary parameters (i.e. Barrick, 1977a; Wyatt, 1988, 2002; Maresca et al.,
1980; Heron and Heron, 1998, Essen et al., 1999; Gurgel et al., 2006). Although
using such empirical relationships avoids the problem of inverting the ill-posed in-
tegral equation that defines the second-order part of the Doppler spectrum, they
do not allow for the estimation of the full directional spectrum. Nonetheless, some
of them have proven to be robust methods for the estimation of significant wave
height. Among them, the Maresca et al. (1980) and Heron and Heron (1998) ap-
proaches remove the weighting function from the equation developed by Barrick
(1977a) and described in the previous section, and include their own empirically fit-
ted parameters into the solution. Comparing the three aforementioned algorithms,
Heron and Heron (1998) found that the exclusion of the weighting function led to
significant errors in crosswind conditions. They concluded that a scaled version
of the original formulation developed by Barrick provides the best results. How-
ever, Ramos (2006) found that the latter produced adequate estimates for low
sea states but overestimated high wave heights, and states that this tendency is
related to the fact that first and second-order limits of the Doppler spectrum are
imposed a priori. To address this shortcoming, the same equation based on Bar-
rick's theory was used, but the first- and second- order limits were defined as the
minimum values within a range dependant on the Bragg frequency, rather than a
fixed value. Essen et al. (1999), applied empirical regression curves to determine
significant wave height and mean wave direction. They found a high correlation
between the standard deviation of the Bragg frequency and the significant wave
height weighted by an azimuthal function. This allowed them to assume a linear
relationship between the two quantities and find two regression coefficients that
are then used to retrieve significant wave height and mean wave direction from

Doppler standard deviations as measured by the radar. A similar approach is
used in the method presented in Gurgel et al. (2006), where it is assumed that
the measured radar spectrum depends on the wave height spectrum measured by
a wave buoy weighted by an angular spreading function. Using this relationship
the authors determine a set of frequency-dependent regression coefficients that
allow inferring the ocean wave spectra from second-order Doppler spectra. This
algorithm is shipped with all WERA radars, and will be evaluated later in this
document.

2.2   Data validation and related work

2.2.1   Intercomparison of wave data

The accuracy and reliability of modelled and remotely sensed wave data are rou-
tinely established through comparison against in situ measurements, generally
collected with wave buoys. Reflecting their relative long history of operation, the
processing and interpretation of wave buoy measurements are well known pro-
cesses, hence these data are normally considered sea-truth. On the other hand,
deriving ocean wave information from remotely sensed signals often involves so-
phisticated inversion techniques, and the theory that underpins the measurements
is sometimes not completely well understood, or somehow limited in its description
of the variable of interest. These factors typically mean that validation against
more established measurement techniques is a mandatory exercise prior to devel-
oping acceptance of these data.

Nonetheless, because it is common practise to integrate wave data sets obtained
with different sensors into common databases, the inter-comparison of wave mea-
surements is not exclusive to validation of remote sensing or modelled products,
but a common exercise in the field of wave science, hence the existing literature

focused on the comparison of different wave measuring platforms is extensive (Allender et al., 1989; Anctil et al., 1993; O'Reilly et al., 1996; Graber et al., 2000; Drennan et al., 2003; Pettersson et al., 2003; Wyatt et al., 2003; Collins et al., 2014). In general, comparison of the energy containing part of the spectrum results in good agreement between techniques, while discrepancies arise when the focus of the analysis lies outside this range. Directional properties, more problematic to measure and quantify (Kahma et al., 2005), have commonly been found to disagree more than the variance of the spectrum. Both instrumental limitations and inconsistent analysis techniques, have been pointed out as the main drivers for these differences (Pettersson et al., 2003).

Despite the number of studies covering the inter-comparison of wave measurements, there is not an established and standardised procedure to follow. Nevertheless, there have been some efforts to make recommendations on best practises. Krogstad et al. (1999), identified significant wave height, mean and peak period, mean wave direction, and the directional spreading of waves as the parameters required for the appropriate description of a sea state. In order to evaluate the agreement of the aforementioned parameters measured by two different devices, it is common to consider one of them as a reference, assuming it provides 'sea-truth' measurements. As such, any disparities between methods are attributed to the test system, and standard descriptive statistics (e.g. linear regression analysis, correlation coefficients, mean error, bias, scatter index) are used to quantify the magnitude of the deviations.

However, there is currently not a single measuring system able to produce unbiased, error free measurements, as these will be subjected to sampling variability at the very least. Therefore, a two-sided regression capable of accounting for errors in both measurements is generally regarded as a more suitable approach for comparison (Krogstad et al., 1999). This is particularly relevant to the comparison of remote sensing products against point measuring devices. The two techniques,

with their differing measuring principles and spatial resolution, can both be providing a perfect measurement and yet show differences when compared against each other (Mackay, 2009). Therefore, taking into account the errors in both data sets is the best way to make an accurate interpretation of the differences between methods. However, given the complicated techniques involved, calculating sampling variability for remotely sensed measurements is not an easy task. For example, determining the sampling variability of wave parameters derived from the mathematical inversion of HF radar backscatter, requires computer simulation (Sova, 1995; Krogstad et al., 1999). An alternative is to substitute the ordinary regression analysis with an orthogonal approach, assuming equal error variances in the two datasets. However, the latter assumption does not always hold. An alternative way of investigating the variance of the errors without the need for calculating sampling variability is through triple collocation methods (Janssen et al., 2007; McColl et al., 2014). These can be used whenever there are three independent collocated data sets available, and are usually applied to estimate the errors associated to remotely-sensed, in situ-measured, and modelled results.

Albeit the abundant information that can be extracted from the above analyses, not all the differences can be properly explained using integrated wave parameters only, and comparison of spectral properties is generally advised (Krogstad et al., 1999). Inspection of graphical representations of cases associated to a variety of meteorological conditions, comparison of average spectra, and calculation of spectral ratios, are among the most common approaches to comparison between spectra and frequency dependent parameters derived from different methods. Additionally, statistics can be obtained for discrete frequency bands (e.g. Rogers et al., 2005; Janssen, 2008). This approach is used in a comparison technique developed as part of the Coastal Data Information Program (CDIP), which is based on the study of the spectral distribution of the energy density and the first four Fourier coefficients of the directional energy distribution (O'Reilly et al., 1996).

The spectra of each of the data sets compared is discretized in frequency-energy bins, and calculations are performed on the data that falls in each of these bins. Another procedure for the comparison of frequency spectra has been recently proposed in Dabbi et al. (2015), and it is based on the parallel comparison of two parameters. According to the authors, such information can provide insight on the differences in magnitude or shape between two spectra. Differences in wave height are studied together with those in maximum spectral energy, and give an idea of the dissimilarities in spectral areas, while differences in peak frequency and maximum energy give an idea of any frequency offsets.

2.2.2 Validation of HF radar wave measurements

Most of the publications addressing the accuracy of HF radar wave estimations have been produced as part of big multidisciplinary projects. One of the first of such type was DUCK94 (Birkemeier et al., 1996), conducted at Duck, North Carolina (NC) and designed as a test of new instrumentation to support another project looking at improving fundamental knowledge of the natural processes that cause beaches to change. Also conducted at Duck, SHOWEX (Shoaling Waves Experiment) (Graber, 2005) looked at the variation of the wave field in the shoaling zone. Back in Europe, SCAWEX (Surface Current And Wave Variability Experiments; Gurgel et al. (1998)) consisted of three experiments conducted in England and The Netherlands, and was intended to provide datasets that measured the spatial and temporal variability of ocean surface waves and currents. Like SCAWEX, EuroROSE (Wyatt et al., 2003) was a European Union funded project aimed to combine fine resolution numerical models together with ground-based radar sensors, in order to provide the spatial and temporal resolutions needed at coastal seas. Finally, NURWEC2 (Netherlands-UK Radar Wavebuoy Experimental Comparison), the only project focused on just HF radar, was aimed to evaluate new

software for significant wave height and directional spectrum measurements using
a PISCES dual radar system (Wyatt, 1991).

Using a 7-day section of data recorded over 5 min sampling periods by a 25.4
MHz OSCR radar during the DUCK94 experiment, Heron and Heron (1998) com-
pared the results of three semi-empirical algorithms used to obtain the root-mean-
squared wave height. Using the method showing the best performance from the
three, they found a RMS difference of 7 cm between the radar and a directional
wave buoy in wave fields, which ranged from 0.1 to 0.7 m significant wave height.
Essen et al. (1999) tested an empirical algorithm that relates the total variance
of the first order Bragg peaks to the significant wave height weighted by an az-
imuthal function. The radar measurements were compared against thirty-four
days of directional Waverider buoy measurements collected during the SCAWEX
experiment, where the radars operated at 27.65 MHz and measured backscattered
signals from the ocean during 9 min. Throughout the thirty-four days, significant
wave height varied between values less than 0.5 m and higher than 4 m. Linear
correlations (R) between 0.8 and 0.9 were obtained at some regions of the spa-
tial field up to 30 km from the radar station, where the noise began to dominate
the measurements. Wyatt and Green (2002) gathered the results of all the main
radar experiments with which the University of Sheffield had been involved to the
time of writing. The mean correlation coefficient (R) between OSCR, PISCES and
WERA radars and buoy measurements was 0.94 for wave height and 0.79 for mean
wave direction. The largest differences were found for the OSCR dataset collected
during the SHOWEX experiment, and are attributed to antenna sidelobe contam-
ination (OSCR limitations are further discussed in Wyatt et al. (2005) and will be
summarised later in this section). In spite of some outliers associated with high
sea states, the PISCES radar, which transmitted the lowest frequency of all radars
tested, yielded the highest correlations when compared to in situ-measured wave
height and mean direction. Wyatt et al. (2003) collates the results acquired with

WERA radars at two different sites (Fedge - Norway and Gijon Spain). In both experiments, the radars operated at 27.65 MHz and recorded backscattered signals for 9 min, every 20 min. The analysis of the data collected at Fedge focused on a 7-day period, which included the highest storm event during which the significant wave height reached almost 12 m. An 8-day period was analysed from the data collected at Gijon, which included two swell events characterized by waves of 4 m significant wave height and a mean period of 13 s. The results show a very good correlation of wave height between buoy and radar, with a mean bias of 6%. Mean periods at both locations were much lower than those measured by the buoy, and this is related to an overestimation of high frequency amplitude during high wave height events, also reported in Wyatt et al. (1999). Mean direction differences between WERA and the X-Band radar, WaMos, are reported to be noisy at Gijon, while at Fedge the comparison against wave buoy data resulted in differences less than $2 \pm 28°$. The difference between the two comparisons is the location of the validation point, which at Gijon was located at the edge of the measurement region, where the influence of sidelobe contamination is higher. Using a couple of radars transmitting on the lower HF band (12 MHz), Wyatt et al. (2008) compare the results of two WERA radars deployed on the Brittany coast, against the outputs of a wave model. The study covered nine days and revealed wave spectra which were accurate in shape, but overestimated the amplitude during high sea states. This issue was linked to limitations imposed by the theory that underpins the inversion (Wyatt et al., 2011), while further inaccuracies were attributed to the short time averaging (9 min) used to derive directional spectra. The same problem was reported in Savidge et al. (2011) and Voulgaris et al. (2008), and it is extensively discussed in Wyatt et al. (2009), where it was concluded that an integration time of few minutes is not long enough to reduce sampling variability for wave measurement. In addition to Wyatt et al. (2008), results obtained at the lower HF band are presented in Wyatt et al. (2006). The latter work is based on measurements acquired with a PISCES radar, and is possibly the only using

a long averaging period of 19 minutes. The results show accurate wave heights, with correlation coefficients of 0.94 during the energetic months, which decreased to 0.86 under milder conditions. The best results for wave period were measured in the range 0.05 - 0.22 Hz, and as observed for the wave height, the statistics are better for energetic conditions. With a maximum correlation coefficient of 0.62, wave direction is the worst correlated parameter to the wave buoy, with the best results obtained for the energy containing part of the spectrum, from 0.1 to 0.2 Hz and wave heights higher than 2 m.

Rather than using a dataset collected during an experimental, short-term project, Savidge et al. (2011) summarised the results obtained with two operational 8.3 MHz WERA radars located on the South East of the United States. Radar-derived estimates and in situ measurements were examined for a variety of parameters, including significant wave height and directional wave spectra. The results showed that while significant wave height estimates obtained with the manufacturer-supplied software (Gurgel et al., 2006) were much noisier than the measurements from in situ sensors, they captured lower frequency variability fairly well. The authors also compared the directional spectra produced by the Seaview Sensing software to the results provided by a VADCP, and conclude that the correspondence between the two is not routinely good. The radars used in this study were located 90 km apart, and had receiving arrays formed by twelve antennas. None of the enumerated characteristics are recommended for wave processing, and as suggested by the authors, this compromised the wave comparison.

In addition to the above, a limited number of spatial validations that compare the radar results to more than one in situ instrument have also been produced. However, they have generally suffered from poor data quality and/or availability. Wyatt et al. (2005) tried to conduct one such study using OSCR radar, but the data availability at the location of the two wave buoys used in the analysis

was as low as twenty-six and forty-four measurements, respectively. As a consequence, data from one of the buoys, located at the edge of the radar coverage, were compared to non-collocated radar estimations obtained at the centre of the measurement region, where the data availability was higher. This resulted in a relative bias of 27% and a correlation coefficient of 0.85 for wave heights which ranged between 0.5 and 3 m approximately. In spite of the relatively good results, the authors point out that OSCR is not capable of operational wave measurement. Hardware, signal-to-noise ratios, and antenna sidelobes are identified as the main limitations. It is nonetheless emphasised that these are specific to the system used and should not be seen as a problem inherent to HF radar systems. Voulgaris et al. (2008) and Haus et al. (2010) both describe the same experiment, and as far as the author is aware, are the only studies which have compared radar estimations to as many as five different in situ instruments deployed within the radar domain. The study was conducted using a pair of WERA radars, operating at 16 MHz and with an integration time of 5 min. Validation of the radar data was conducted for a 45-day period characterised by persistent light winds and low wave heights, with the maximum hourly significant wave height being 1.35 m. Correlations between wave heights computed using an empirical approach developed by Ramos (2006) and those observed at all the in situ sensors were significantly lower than those obtained for the comparisons between in situ observations (Voulgaris et al., 2008). Additionally, directional spectra obtained using the Seaview Sensing inversion algorithm were compared to the spectral estimates from two Tri-Axys buoys over a 6-day period. Significant wave height showed good agreement between the WERA and the buoys over the first 22 % of the record, but there were large errors for the last half of the observation period. The authors conclude that these discrepancies might be caused by the limited length of data used for the calculation of HF radar spectra, compared to the 20 min datasets used for the in situ sensors. Rather than using in situ devices, Jaffres and Heron (2011) compared the significant wave height obtained with a HF radar system to that computed with the WaveWatch

III wave model. The radar wave heights were derived from an empirical algorithm, which was fed with data collected over 10 min sampling intervals by a 8.3 MHz WERA system. Although the differences between the model and the results of one of the stations reached 4 m in a localized area near the radar station, the authors report the significant wave height field to compare reasonably well with the model estimates, and noticed that the spatial maps of wave heights derived from the radar measurements showed higher variability than the model results. This is a common observation on the radar maps, and whether it is real or derived from radar errors is still not clear until additional statistically significant spatial validations are provided. Nonetheless, Jaffres and Heron (2011) stated that the differences could be in fact attributed to the absence of surface currents in the model forcing and the low resolution of the wind input, both of which lead to a spatially more homogeneous significant wave height map.

The works summarised above evidence the main drawbacks of the currently available validations of HF radar wave measurements. Data acquired over short experimental venues using radars not properly configured for the task of wave measurement, are common aspects of most of the published works. Furthermore, only few studies have tested any other parameters than significant wave height, and the spatial mapping capability of the technique is not supported by enough quantitative evaluations against either a group of in situ measurements, or wave models.

Despite the deficiencies identified, there is enough evidence suggesting that HF radar is capable of producing accurate estimates of at least significant wave height, and the validation of an installation designed for measuring waves is of fundamental importance for a conclusive evaluation of the wave measurement ability of this technology.

2.3 Wave-current interaction and related work

Ambient currents can change the amplitude, direction, and frequency of ocean surface waves (Holthuijsen, 2007). These modifications are usually divided into their effects on the wave kinematics and dynamics (Jonsson, 1990), and as such are briefly summarised below. The reader is referred to Peregrine (1976) or Jonsson (1990) for comprehensive reviews of the interaction processes and the mathematical derivations used to study them. In addition to the background theory, some relevant works are also summarised, laying particular interest on those which focused on the effects of tidal currents and were based, at least in part, on observational data.

2.3.1 Wave kinematics

Changes in wave kinematics are a result of current variations in space and time, which modify the wave number and frequency of waves. In the linear theory of gravity waves, these two parameters are related by the linear dispersion relationship as follows,

$$\sigma = \sqrt{gk \tanh kh} \qquad (2.11)$$

where σ is the relative wave frequency, g is the gravitational acceleration, k is the wave number, and h is the water depth.

2.3.1.1 Effects on wave frequency

In the presence of a current $\mathbf{U}$, the relative frequency defined by Equation 2.11 will be Doppler shifted, and the observed frequency (ω) in a stationary reference frame becomes,

$$\omega = \sigma + \boldsymbol{k} \cdot \boldsymbol{U} \qquad (2.12)$$

In the most realistic case, in which depth and current are allowed to vary in space and time, the rate of change of the absolute wave frequency is found by differentiating Equation 2.12 with respect to time and employing the conservation of wave crests principle (Haller and Özkan-Haller, 2007).

$$\frac{\partial \omega}{\partial t} = -\frac{\partial \omega}{\partial x} \tag{2.13}$$

This gives the equation governing the rate of change of wave kinematics for the inhomogeneous and unsteady case,

$$\frac{\partial \omega}{\partial t} + (U + c_{gr}) \frac{\partial \omega}{\partial x} = k \frac{\partial U}{\partial t} + q \frac{\partial \eta}{\partial t} - p \frac{\partial \eta}{\partial t} \tag{2.14}$$

where c_{gr} is the relative group velocity, defined as the speed of wave energy propagation in a frame moving with the local current velocity and η is the water level. The quantities c_{gr}, q and p are defined as,

$$c_{gr} = \frac{1}{2} \left(1 + \frac{2kh}{\sinh 2kh} \right) \frac{\omega - kU}{k} \tag{2.15}$$

$$q = \frac{\omega k}{\sinh 2kh} \tag{2.16}$$

$$p = \frac{k^2 U}{\sinh 2kh} \tag{2.17}$$

Equation 2.14 indicates that temporal variations in the wave frequency only occur when the currents and/or water depths vary in time and space. However, most of the literature on wave-current interaction is based on the quasi-stationary approach, which assumes that the current field and total water depth are stationary at the time scales relevant to the wave propagation (Haller and Özkan-Haller, 2007). This allows neglecting the local rate of change of the current field and water depth (Jones, 2000), which implies that the frequency is invariant. However, works such as that of Barber (1949) show a correlation between the absolute

frequency of waves and the semidiurnal tide. Despite the impeccable treatment of the wave-current interaction problem, the data available to the study was limited, and the results were obtained using graphical methods to differentiate Equation 2.14. Nonetheless, Barber was able to identify a modulation in wave frequency at a site off south-west Britain, which was attributed to temporal variations of the current, and to a significant lesser extent, to water level fluctuations. Basing his observations in modelled results, Tolman (1990, 1991) also showed correlations between absolute period and tidal current velocity, and Jones (2000) found that quasi-steady analytical models failed to reproduce observed variations at two sites off the coast of south-west Wales. Wolf and Prandle (1999) studied wave-current interaction based on measurements collected by a wave buoy and a current meter deployed in two near-shore locations of the North Sea. They found evident tidal modulation of the wave period and a variation of wave steepness due to the Doppler shift of the relative frequency. The modulation was correlated with the current with a phase lag of 3 h, a result that deviates from the expected behaviour based on the Doppler shift described by Equation 2.12 alone. These results indicate that neither the spatial gradients, nor the unsteadiness in water depths and currents are negligible in an area under tidal influence.

2.3.1.2   Effects on wave direction

Waves propagating over a varying current field will experience current-induced refraction. Differentiating 2.12, and using 2.13, the rate of change of wave direction can be determined as (Tolman, 1991),

$$\frac{d\theta}{dt} = -\frac{1}{k}\left[\frac{\partial\sigma}{\partial d}\frac{\partial d}{\partial m} - \boldsymbol{k}\cdot\frac{\partial\boldsymbol{U}}{\partial m}\right] \tag{2.18}$$

where m is a coordinate perpendicular to the direction θ, and the operator d/dt is defined as:

$$\frac{d}{dt} = \frac{\partial}{\partial t} + (C_g + U) \cdot \nabla \qquad (2.19)$$

Although current-induced refraction is mentioned quite regularly in studies regarding wave-current interaction, this mention is generally made to explain the focusing and defocusing of wave energy due to this process. However, changes in the direction of wave propagation itself are rarely reported in the literature. As mentioned in Hopkins et al. (2015) this is because most studies are conducted in estuarine and inlet areas, were waves barely change direction.

In a study based on modelled currents validated with HF radar, and wave fields obtained with the WW3 model and supported by wave buoy measurements, Ardhuin et al. (2012) provide evidence of the effect of current-induced refraction on both, the modulation of wave energy, and the direction of wave propagation. The latter was found to be affected by the tide, veering over 20° between high and low tide. As is common in studies based on modelled results, the conclusions are supported by the comparison between the results of a model run with variable currents and water levels, and one without them. Hopkins et al. (2015) report a strong tidal modulation ($\pm$35°) of the direction of 0.1 Hz measured waves propagating from 50 m to 7 m depth across tidally varying currents. Such modulation was attributed to current-induced refraction rather than bathymetric effects, and the theory is supported by the better agreement of the measurements with the model including tidal currents and variable water depths. Jones (2000) also reports variations of about 15° in wave directions calculated with a ray tracing model over a tidal cycle. However, observations to verify the results were not available.

2.3.2   Wave dynamics

Although this work will focus on changes on the phase parameters of waves, which are described by the expressions shown the previous section, the effect of a current field on the energy density (E) of the wave spectrum is included here for completion. This can be determined solving the spectral action balance equation in terms of the relative frequency (σ),

$$\frac{\partial N}{\partial t} + \nabla_x \cdot [(c_g + U)N] + \frac{\partial}{\partial \theta}[c_\theta N] + \frac{\partial}{\partial \omega}[c_\omega N] = \frac{S}{\sigma} \tag{2.20}$$

where $N = E/\sigma$ is the action density spectrum, and S represents the net effect of sources and sinks for wave variance. The left hand side of Equation 2.20 represents the local rate of change of the action density and effects of propagation. The first term represents the local rate of change of the action density in time. The second term accounts for the propagation of action density in geographic space, the third represents refraction and the fourth term defines the shift of the relative frequency due to variations in depth and currents. The right-hand side is the source/sink term of the equation and represents all physical processes that generate, dissipate or redistribute energy.

Chapter 3

Materials and Methods

This chapter provides an introduction to the study area, as well as of all devices used to collect the data used throughout this work. Details about the processing of such data are also given, and some general methods used throughout are summarised.

3.1 Study area

The measurements analysed in this work were collected at the Wave Hub; a grid connected wave energy site for testing offshore renewable energy technologies located in the North coast of Cornwall (UK). Wave Hub is an initiative set to provide the required infrastructure for testing offshore renewable energy technologies. It consists of an underwater electrical hub, located approximately 20 km offshore the town of Hayle, at an average depth of 50 m.

The hub has four electrical connections, each associated with an area of 2 km^2 of sea, and a total capacity of 30 MW. This will give wave energy device developers the opportunity to connect their devices to the National Grid for pre-commercial testing (SWRDA, 2006).

3.1.1   Wind and wave climate

The wave climate in the south-west of England is a combination of long-period swell that propagates across the North Atlantic and locally generated wind waves, which are both modified by a current field that is largely dominated by tidal streams reaching 1 ms^{-1} (SWRDA, 2006). The area is well exposed to waves arriving from the west and south-west, and to some extent shielded by Ireland from waves coming from the north-west (SWRDA, 2006). The prevailing wind directions are between south-south-west and north-west, with north-easterly winds increasing their frequency in late winter and spring. Winds of force 5 (8 ms^{-1}) or greater occur about half of the time in autumn and winter, and only 25% and 15% during spring and summer, respectively (OESEA3, 2016). The western winds are associated to the low pressure systems that track the North Atlantic, and consequently, the wave climate is not only a result of storminess, but also dependent on the latitudes along which storms propagate. This leads to high inter-annual and inter-decadal variabilities, which are believed to be associated with the North Atlantic Oscillation (NAO) (Saulter, 2011). Typical wave conditions are composed of waves with 1.6 m significant wave height and 6 s mean period, while the 1 in 1 year return periods can reach the 10 m significant wave height and 12 s period (SWRDA, 2006).

3.1.2   Tidal conditions

Tides typically account for 90% of the variability in the currents (Howarth and Proctor, 1992) measured over the European continental shelf. About 75% of the total kinetic energy is contained in the principal lunar semi-diurnal (M_2) tidal constituent. This is followed by the principal solar semi-diurnal (S_2), which has about 0.33 of the amplitude of the M_2. The interaction between these two constituents results in the fortnightly modulation of the tide responsible of the spring-neap

cycle. During spring tides both components are in phase, and result in tides with an amplitude 1.33 times the values of the M_2 component alone. The situation is reversed during neap tides, when the constituents are in quadrature, and the amplitude decreases to about 0.67 times the M_2 (Pingree, 1980). These components, and therefore the predominant currents, are oriented toward the west-southwest during ebb and veer east-northeast during flood. The maximum current magnitudes occur during spring tides, and reach values of about 1 ms^{-1}.

3.2 Data sources

3.2.1 HF radar

The radar dataset used throughout this study was obtained with two phased-array WEllen RAdars (WERA) (Gurgel et al., 1999a) deployed on the north coast of Cornwall to overview the area described above. The individual stations are located at Pendeen (master station) and Perranporth (slave station), approximately 40 km apart, and have been operational since the end of 2010 and beginning of 2011, respectively. Each site consists of a 16-element phased-array receiver and a rectangular 4-element transmitter located roughly parallel to the coast.

The master station is located in a limited stretch of a cliff, which lies within a cattle farm in the village of Pendeen, Cornwall. These two conditions make of this site a particular deployment, with a curved array and antennas stabilized by a concrete base to avoid the use of guiding ropes. The receiving array at Pendeen is orientated at 113° from true North (clockwise) hence its boresight (beam direction perpendicular to the receivers) is directed 23°, also from North. The predominant waves, coming from the west and southwest will therefore interact almost perpendicularly with the radar beam.

The slave station is situated at Perranporth's airfield, a flying club located in the village of Trevellas, Cornwall. This site is what can be considered a more traditional setting for a HF radar deployment, with a linear receiving array composed of antennas supported by the usual guiding ropes. The orientation of Perranporth's receiving array is 35° from North, and its boresight is directed to 305° also from North (measured clockwise). The angle between the predominant waves and the radar's main lobe is therefore smaller for this site. The signal recorded at this station is consequently expected to be generally stronger than at Pendeen, as the radar receives a stronger signal from waves propagating towards or away from the radar than from those propagating perpendicular to it (Wyatt, 2002).
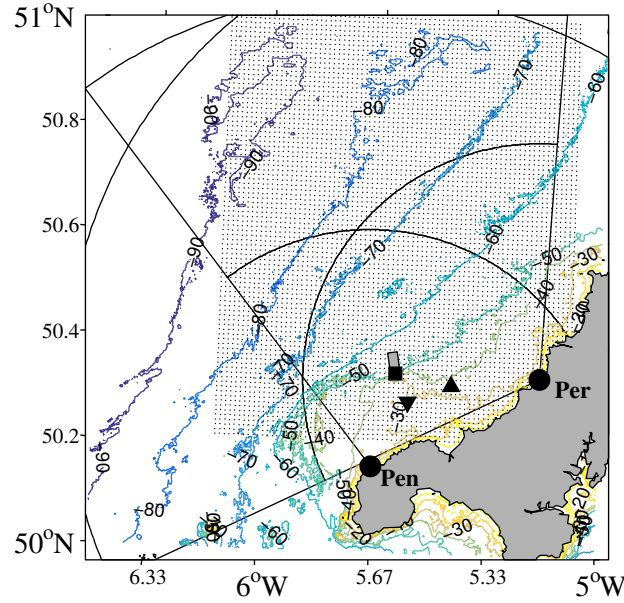
Figure 3.1: Radar stations (black circles), their coverage (120° fans) and measuring grid. Surface current measurements are possible within the full area delimited by the fans, while wave measurements are restricted to the area demarcated by the small arcs. Depth contours are also shown and expressed in meters. The positions of three in situ mooring devices deployed in the area are also displayed: wave buoy (star), ADCP-W (inverted triangle) and ADCP-E (triangle). The grey rectangle delimits the Wave Hub test site for marine renewable energy (MRE) devices.

Measurements are synchronously acquired at the two stations for 17 min 45 s, every hour, at approximately 1-km range resolution and 7° angular resolution. Both

radars operate in a listen before talk mode (Gurgel and Schlick, 2007), determining the cleanest operating frequency for transmission within a 250-kHz bandwidth, and around a centre frequency of 12 MHz. At this frequency, the transmitted waves are backscattered off ocean waves 12.5 m long, from distances up to 101 km. Only surface current measurements are, however, achievable over the full range, while wave products are limited to half this distance due to the lower signal-to-noise ratio (SNR) of the second-order returns compared to the first-order echo.

The measuring period of 1065 s sampled at 3.85 Hz results in time series with 4096 samples. In the first stage of the processing, these signals are range and azimuth sorted to grid points in a 75-by-90 rectangular grid at 1-km spacing (see Gurgel et al. (1999a)) and Chapter 4 for details). Doppler spectra are then calculated using 512 point Fast Fourier Transform (FFT) with 75 % overlap.

3.2.1.1 Current measurements

As it was introduced in Chapter 2, the measurement of surface current is based on the displacement of the Bragg peaks from their theoretical position, derived from Equation 2.3. This relation will give the radial component of the current along the look direction of each radar. Two independent radial estimates obtained from each radar are then combined to construct two dimensional current vectors (Figure 3.2). The east-west component of the surface current is obtained for each cell in the radar grid as,

$$u = \frac{r_1 \cdot \cos \theta_2 - r_2 \cdot \cos \theta_1}{\sin (\theta_2 - \theta_1)} \qquad (3.1)$$

and the north-south component is,

$$v = \frac{r_2 \cdot \sin \theta_1 - r_1 \cdot \sin \theta_2}{\sin (\theta_2 - \theta_1)} \qquad (3.2)$$

where $r_{1,2}$, and $\theta_{1,2}$ represent radial velocities and angles relative to the boresight from each radar station, respectively.
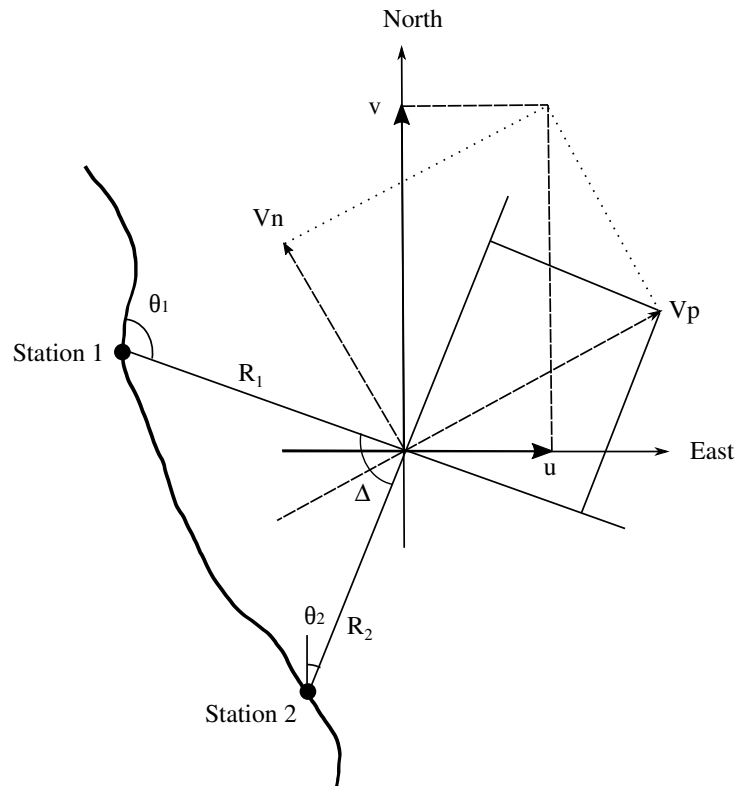
Figure 3.2: Schematic representation of the components used for combining the radial velocity components measured at two stations to produce a vector current. Adapted from Graber et al. (1997).

The current velocity components obtained with Equations 3.1 and 3.2 were then quality controlled using a de-spiking technique based on the concept of a 3D Poincare map. This is based on a graphical representation of the variable and its first and second derivatives. The points located outside of the ellipsoid in the Poincare map are excluded and the method iterates until the number of detected spikes becomes zero (Mori et al., 2007).

3.2.1.2   Wave measurements

The Doppler spectra obtained after the processing synthesised on the previous section are subsequently inverted into ocean wave spectra using two algorithms. One of them is the Wyatt method (Wyatt, 1990; Seaview hereafter) that was briefly described in the previous chapter. Processing by this method results on a wave directional spectrum for each grid point where dual information is available, provided the signal-to-noise ratio (SNR) is higher than 15 dB and the amplitude of the local minima around the strongest Bragg peak is less than 3 dB. When only one of the stations yields usable data only wave parameters are calculated using the empirical expressions presented in Wyatt (2002) . A second algorithm (Gurgel et al., 2006), available from the radar manufacturer, produces estimations of frequency spectra and mean wave direction. The former can be calculated from the results of just one station, while the mean wave direction is only provided at those grid points with overlapping information from the two radars. In this case, the SNR of the second order sideband must be above 10 dB for the wave calculations to be performed. Details regarding each of these methods will be discussed further in Chapters 5 and 6, where their results are evaluated.

3.2.2   Wave buoy

From 13 March until 20 December 2012, a Seawatch Mini II directional wave buoy was deployed at 53 m depth, 20 km offshore from Pendeen and 30 km from Perranporth (see Figure 3.1). The Seawatch Mini II is a displacement buoy, which therefore follows the motion of the water surface particle when wave forces are exerted upon it in a defined range of frequencies. The device is equipped with the Wavesense III wave sensor which comprises accelerometers, rate gyros and magnetometers mounted orthogonally to provide basic data, which are processed to provide heave, roll, pitch, surge, sway and compass time series.

The buoy was set to record its position in the vertical, east and north directions for 17 min 4 s, every 30 min at 2 Hz. These data, which are stored in the internal hard drive of the Seawatch Mini II, were posteriorly downloaded and processed using WAFO (Wave Analysis for Fatigue and Oceanography), a toolbox of Matlab routines for statistical analysis and simulation of random waves and loads (Brodtkorb et al., 2000).

Calculation of the directional spectrum requires the computation of the cross-spectra of the three components of motion measured by the buoy. Assuming linear theory, the relationship between the cross-power spectrum for a pair of wave properties and the wave directional spectrum is,

$$
\Phi_{mn}(f) = \int\limits_{0}^{2\pi} H_m(f,\theta)H_n^*(f,\theta)[\cos\left(k\left(x_{mn}\cos\theta + y_{mn}\sin\theta\right)\right) -
$$
$$
\sin\left(k\left(x_{mn}\cos\theta + y_{mn}\sin\theta\right)\right)]E(f,\theta)d\theta
$$

$$(3.3)$$

where $\Phi_{mn}(f)$ is the cross-power spectrum between the m-th and n-th wave properties, $H_m(f,\theta)$ is the transfer function from the water surface elevation to the m-th wave property, x_m the location vector of the wave probe for the m-th wave property, $E(f,\theta)$ is the directional spectrum , and " * " denotes the conjugate complex.

The directional spectrum is usually expressed as a product of the frequency spectrum $S(f)$ and a directional spreading function $G(\theta|f)$ as,

$$
E(f,\theta) = S(f)G(\theta|f) \tag{3.4}
$$

where $E(f,\theta)$ is the directional spectrum, $S(f)$ is the frequency spectrum and $\int\limits_{0}^{2\pi} G(\theta|f)d\theta$ is equal to 1.

If an infinite number of wave properties were measured, the directional spectrum could be uniquely determined using classical cross-spectral analysis and the co- and

quad-spectra of the measured properties and using Equation 3.3. However, the three motion signals recorded by wave buoys do not contain enough information to obtain accurate estimates, and statistical techniques have to be applied to approximate the spreading distribution and resolve the directional spectrum. Here, we used the Extended Maximum Entropy Method (EMEM; Hashimoto, 1997).

The method was applied as implemented in the WAFO function *dat2dspec*, which estimates the directional wave spectrum from recorded heave, north and east positions. A 256-point cross-spectral analysis with 50% overlap and a Hanning window, along with the EMEM estimates of the directional distribution, resulted in directional spectra at 0.0078 Hz frequency resolution and 4° directional resolution. In order to match the lowest resolution spectra used in this work, which are provided by the radar manufacturer's algorithm, wave spectra were posteriorly re-sampled to 0.01 Hz, and wave parameters were calculated by integrating them over the range 0.05 - 0.25 Hz, also used in the radar outputs.

Prior to calculating directional spectra, the raw data were subjected to some basic tests included in common quality control procedures for wave buoy measurements (i.e. IOOS, 2015; Ingram et al., 2011). The tests performed were,

- Out of range. This test checks that the values of the time series fall within limits defined by the operator, $\pm 20m$ for SeaWatch Mini.

- Check for values that exceed 5 times the standard deviation from the mean of the time series.

- Test to detect if the acceleration of the ocean surface measured exceeds $g/3$, with g being the acceleration due to gravity (9.81 ms $^{-1}$).

- Repetition. Tests for 7 consecutive repeated values in the series.

Wave spectra calculated with the quality-controlled time series were posteriorly analysed for spurious energy at low frequencies following a procedure developed by

Ashton (2011) for data collected at a nearby location using the same type of wave buoy. He found erroneous energy affecting spectra at frequencies below 0.06 Hz and designed a variable low frequency filter to examine the peaks of the spectra. The filter, as described in Ashton (2011), works as follows: whenever the maximum of a system occurs below 0.05 Hz, the entire spectrum is discarded as erroneous. If no maximum occurs below 0.05 Hz, f_1 is set at 0.043 Hz and the energy below that frequency is set to zero. When the energy at f_1 is not close to zero, the shape of the spectrum after filtering might not be representative of naturally occurring conditions. In that case, the algorithm identifies the two minima surrounding the low energy peak and f_1 is set as the frequency associated to the second minimum. Then, the Pierson-Moskowitz spectral shape for a fully developed sea is used to estimate the spectral density at frequencies below f_1.

Finally, wave parameters were tested for defective values, which were subsequently discarded whenever found. An outlier was defined as a value that exceeded three standard deviations from the mean calculated using its four neighbours (two behind and two ahead) in time. Finally, small gaps up to two hours that were either already present in the data set, or generated by the quality control, were linearly interpolated.

3.2.3   ADCP

Two upward looking 600-kHz Teledyne RDI WorkHorse Broadband with a Janus configuration consisting of 4 beams with an inclination of 20° from the vertical, were also present in the area to serve as validation data for the radar's measurements. Both were deployed on the 13 March 2012 and recovered on 16 May 2012. A second deployment, during which devices were located at about the same locations, started on 18 May 2012. Finally, after a second recovery on 11 August 2012, the last deployment began three days later, on 14 August 2012. The eastern-most

ADCP, referred to as ADCP-E here, was located at 24 km from Pendeen and 19 km from Perranporth at an average depth of 33 m, while the other (ADCP-W) was moored at 16 km from Pendeen and 29 km from Perranporth, at an average depth of 35 m over the three deployments (see Figure 3.1).

The raw data collected and stored in the memory card of the instruments were posteriorly processed with the manufacturer's software in order to obtain wave and current information. The next two subsections provide an overview the main aspects of such processing.

3.2.3.1 Current measurements

Current data were obtained every 10 minutes, with a vertical resolution of 0.75 m. Raw measurements were processed using RDI's software in order to obtain current velocities over the water column. Because the data are intended for comparison against the radar's measurement of the surface current, only the uppermost bin was kept for further analysis. Bins located close to the surface are, however, affected by sidelobe reflection, so the first 10% of the water column was discarded, and data from the bin directly underneath were used for subsequent analysis.

Data were then quality controlled using the same de-spiking technique based on the 3D Poincare map (Mori et al., 2007) used for the radar results. Hourly current values were finally computed from the quality-controlled data by averaging six sequential 10 minute observations in order to match the radar measuring scheme.

3.2.3.2 Wave measurements

Data for wave processing were acquired over 20 min measuring periods, every 2 h, at 2 Hz. Five bins automatically selected by the processing software were then used to calculate directional spectra. The along-beam orbital velocities, corrected

for the effect of the current, are used to perform the calculations. In order to resolve the spreading distribution, RDI's software uses the Iterative Maximum Likelihood Method (IMLM; Krogstad, 1988).

The spectral analysis was carried out on a 2048-sample FFT, and resulted in spectra with a frequency resolution of 0.0078 Hz and 4° directional resolution. Similarly to the buoy data, the frequency spectra were posteriorly re-sampled to 0.01 Hz in order to match the other data sets.

RDI's software has some quality control implemented in their processing; hence additional tests were only performed upon the wave parameters posteriorly calculated from the spectra. These were checked for outliers following the same procedure than that used for the buoy data, hence values that exceeded three standard deviations from the mean calculated using its four neighbours were rejected. Finally, small gaps up to two hours that were either already present in the data set, or generated by the quality control, were linearly interpolated.

3.2.4   Wave model

ADCP and buoy measurements are restricted to a single location. Consequently, when assessing the radar's spatial measurements it is necessary to resort to a wave model, which provides estimations of directional wave spectra over the whole HF radar grid. The HOMERE model (Boudiere et al., 2013), run by Ifremer as a support to research activities related to the development of marine renewable energies, was selected as the source for spatial information. The database is a 19-year hindcast covering the period 1994 - 2012, that was obtained with the WAVEWATCHIII (WW3) wave model on a refined unstructured grid, with a resolution that ranges from 200 m to 10 km. WW3 is a phase-averaged wave model resolving the random phase spectral action density balance equation for wave number-direction spectra. The model is forced by 31 years of reanalysis

winds, updated every 6 hours, and with spatial resolution ranging from 0.25° at
the equator to 0.5° at higher latitudes (Saha et al., 2010). Both currents and water
levels are included in the model, and updated every 30 min. These are provided
as harmonic components derived from the outputs of the MARS2 hydrodynamic
model (Lazure and Dumas, 2008), which at the area covering our study site was run
with temporal and spatial resolutions of 1 h and 700 m, respectively. The forcing
is obtained from the results of a coarser model, which is itself forced by the sea
surface height from the FES (2004) global tidal model with 14 tidal components.
The meteorological forcing is provided by the ARPEGE model, run with 0.5°
spatial resolution and a 6 h time step.

The database contains directional spectra at over 4000 locations over an area cov-
ering the English Channel, Bay of Biscay and part of the Celtic Sea. Gridded
outputs such as significant wave height, peak period and wave directions are also
provided, and are available at more than 110000 locations, together with some ad-
ditional parameters that are of particular interest to marine renewable application
such as the wave energy flux or the energy period (Boudiere et al., 2013). Only
model outputs obtained at distances of less than 500 m from a radar grid point
were used for comparison against the latter.

3.3   General Methods

3.3.1   Integrated wave parameters

The previous section provided an overview of how wave spectra were derived from
the measurements of each of the devices that collected the data used throughout
this work. Each of them uses a slightly different approach; hence the methods
were reviewed separately. However, once the wave spectra were obtained, the

calculation of the bulk parameters derived from them was performed using common expressions for all the techniques, and these are enumerated here.

Significant wave height and the energy period were calculated from the frequency spectrum as,

$$H_s = 4\sqrt{\int_{f_1}^{f_2} S(f)\,df} \tag{3.5}$$

$$T_e = \frac{\int_{f_1}^{f_2} f^{-1}S(f)\,df}{\int_{f_1}^{f_2} S(f)\,df} \tag{3.6}$$

and the mean direction and directional spreading were computed as,

$$\theta_m = arg\left[\int_{f_1}^{f_2} S(f)e^{i\theta(f)}\,df\right] \tag{3.7}$$

$$\sigma_m = arg\left[\int_{f_1}^{f_2} S(f)e^{i\sigma(f)}\,df\right] \tag{3.8}$$

where f_1 and f_2 are the lower and upper frequency limits used to calculate the above parameters. These were respectively, 0.05 and 0.25 Hz when all the common frequencies available in all datasets were used. In certain occasions, different ranges were used, but this will be specified in the document. $\theta(f)$ and $\sigma(f)$, appearing in Equations 3.7 and 3.8 were calculated from the first two Fourier coefficients of the directional distribution. When using a wave measuring technique that provides different measures of the wave field, such as the buoy's heave, east and north displacements, these coefficients can be directly retrieved applying standard cross-spectral analysis to the measured signals (Kuik et al., 1988). When this is not possible, or the raw signal is not available, the coefficients can be recovered from the directional spectrum, and this was the approach used here. Once the directional Fourier coefficients were obtained, the spectral mean direction and directional spreading were calculated as (Kuik et al., 1988),

$$\theta(f) = \tan^{-1}(b_1(f), a_1(f)) \tag{3.9}$$

$$\sigma(f) = \sqrt{((2\,(1 - \sqrt{a_1(f)^2 + b_1(f)^2}))} \tag{3.10}$$

3.3.2   Statistical approaches

A range of statistical techniques were used in the following two chapters to establish the accuracy of the radar measurements. Ordinary least squares regressions were performed, and standard descriptive statistics were calculated to provide a quantitative measure of the dissimilarities between the datasets compared. Biases, root-mean-squared errors, the scatter index of the data, and the linear correlation between two datasets were calculated as,

$$\text{Bias} = \frac{1}{n}\sum_{i=1}^{n}(y_i - x_i) \tag{3.11}$$

$$\text{RMSE} = \sqrt{\frac{1}{n}\sum_{i=1}^{n}(y_i - x_i)^2} \tag{3.12}$$

$$\text{SI} = \frac{RMSE}{\bar{x}} \tag{3.13}$$

$$\text{R} = \frac{\sum_{i=1}^{n}(y_i - \bar{y})(x_i - \bar{x})}{\sqrt{\sum_{i=1}^{n}(y_i - \bar{y})^2 \sum_{i=1}^{n}(x_i - \bar{x})^2}} \tag{3.14}$$

In all the equations, x corresponds to the reference value and y is the radar measurement. The variables with an over-bar indicate mean values.

Whenever possible, directional variables were compared using expressions from circular statistics. Mean values of the angular data were calculated by vector addition as described in Bowers et al. (2000),

$$\hat{x} = \pm\tan^{-1}\left(\frac{S}{C}\right) \tag{3.15}$$

where S and C are given by,

$$S = \sum_{i=1}^{n} \sin(x_i) \tag{3.16}$$

$$C = \sum_{i=1}^{n} \cos(x_i) \tag{3.17}$$

The circular standard deviation can then be calculated as,

$$\sigma = \sqrt{2(1 - R)} \tag{3.18}$$

where $R = \sqrt{C^2 + S^2}/n$, with n the number of records.

The values calculated with the above expressions were then used in Equations 3.11 to 3.13, while the linear correlation coefficient (Equation 3.14) was replaced by its circular counterpart (Bowers et al., 2000),

$$R = \frac{\sum\limits_{1 \leq i \leq j \leq n} \sin(x_i - x_j)\ \sin(y_i - y_j)}{\sqrt{\sum\limits_{1 \leq i \leq j \leq n} \sin^2(x_i - x_j) \sum\limits_{1 \leq i \leq j \leq n} \sin^2(y_i - y_j)}} \tag{3.19}$$

In calculating the above statistical descriptors, the radar was considered the test value. As such, all the error is attributed to its measurements. However, as mentioned in Chapter 2, in situ measurements are also imperfect, and establishing the errors associated to each data set being compared is the best way to make a good interpretation of the dissimilarities between them. Such analysis was performed here using the extended triple collocation method (ETC; McColl et al., 2014) with the in situ, radar and model data sets. In triple collocation (TC) techniques, the standard error model that relates a measurement to a 'true' geophysical variable is usually expressed as,

$$X_i = \alpha_i + \beta_i t + \epsilon_i \tag{3.20}$$

where the $X_i (i \in 1, 2, 3)$ are collocated measurements linearly related to the true underlying value t. X_i is assumed to be a combination of the underlying truth

plus a random error ϵ_i. α_i and β_i are the ordinary least squares intercepts and slopes, respectively. X_i, X', t, and ϵ_i are all random variables,

Under the assumption that X_i and t are anomalies from a climatological mean, the offset α_i can be dropped from Equation 3.20. The covariances between the different measurement systems are then calculated as,

$$\begin{aligned} \text{Cov}(X_i, X_j) = E(X_i Y_j) - E(X_i)E(X_j) = \\ \beta_i \beta_j \sigma_t^2 + \beta_i \text{Cov}(t, \epsilon_j) + \beta_j \text{Cov}(t, \epsilon_i) + \text{Cov}(\epsilon_i, \epsilon_j) \end{aligned} \tag{3.21}$$

where $\sigma_t^2 = \text{Var}(t)$. Assuming that the errors from the independent sources have zero mean $(E(\epsilon_i) = 0)$ and are uncorrelated with each other and with the true value, t, the two middle terms of the right-hand side of Equation 3.21, and the last term (whenever $i \neq j$), are zero. With these assumptions, and defining a new variable $\theta_i = \beta_i \sigma_t$, Equation 3.21 becomes,

$$Q_{ij} = \text{Cov}(X_i, X_j) = \begin{cases} \theta_i \theta_j, & \text{for } i \neq j \\ \theta_i^2 + \sigma_{\epsilon_i}^2, & \text{for } i = j \end{cases} \tag{3.22}$$

where $\sigma_{\epsilon_i}^2 = \text{Var}(\epsilon_i)$. Using the three collocated measurements, the above results in a system with six equations and six unknowns that can be solved to obtain the TC estimation of the error variances,

$$\sigma_\epsilon = \begin{cases} Q_{11} - \frac{Q_{12}Q_{13}}{Q_{23}} \\ Q_{22} - \frac{Q_{12}Q_{23}}{Q_{13}} \\ Q_{33} - \frac{Q_{13}Q_{23}}{Q_{12}} \end{cases} \tag{3.23}$$

In addition to the error variances commonly calculated in TC techniques, McColl et al. (2014) derived an expression to calculate the correlation coefficient between the measured variable and the unknown truth. Using Equation 3.20, and standard

definitions of correlation and covariance, they obtained,

$$\theta_i = \rho_{t,X_i}\sqrt{Q_{ij}} \tag{3.24}$$

where ρ_{t,X_i} is the correlation coefficient between the measured variable and the unknown truth. Estimating $\sqrt{Q_{ij}}$ from the data, and using Equation 3.22 to solve for θ_i, the expression for the correlation coefficient can be obtained as,

$$\rho_{t,X} = \pm \begin{bmatrix} \sqrt{\frac{Q_{11}Q_{13}}{Q_{11}Q_{23}}} \\ \operatorname{sign}(Q_{13}Q_{23})\sqrt{\frac{Q_{12}Q_{23}}{Q_{22}Q_{13}}} \\ \operatorname{sign}(Q_{12}Q_{23})\sqrt{\frac{Q_{13}Q_{23}}{Q_{33}Q_{12}}} \end{bmatrix} \tag{3.25}$$

The correlation coefficient calculated with Equation 3.25 provides an unbiased signal-to-noise ratio, scaled between 0 and 1, and combines information about the sensitivity of the measurement system to the variable of interest, and the variabilities of the signal and measurement error.

The above methodology will be used in the following three chapters to examine the error variances of the in situ and radar measurements, and the outputs of the model previously described in this chapter. In doing so we use 1000 bootstrap simulations to calculate the covariance matrices used in Equation 3.23 . The error variance is then obtained averaging the results of all the simulations.

Chapter 4

Semi-Empirical Estimates of One-Dimensional Wave Spectra

This chapter is focused on the evaluation of the accuracy of the inversion algorithm included in the in-house software provided with WERA radars. Due to its empirical nature, it has been possible to re-calibrate the algorithm with data collected at the Wave Hub, and the results of such calibration are also summarised here.

4.1 Introduction

The semi-empirical method (Gurgel et al., 2006; WERA algorithm) is based on a simple linear relation between the ratio of second- to first-order Doppler energy and the ocean wave spectrum weighted by an angular spreading function. The method, in spite of being provided with all WERA radars, has barely received any attention in the literature; hence, very little is known about its performance. Furthermore, although it provides an estimation of the wave frequency spectrum, only validations of the wave height results have been reported in the literature (Gurgel et al., 2006; Savidge et al., 2011; Toro et al., 2014). Savidge et al. (2011)

provide a comparison of radar-derived wave heights and in situ measurements in the form of scatter plots, but no quantitative measures for the goodness of fit are reported. Nevertheless, the figures included in the publication indicate high scatter and positive bias on the radar estimates, somewhat poor results that were nonetheless attributed to a suboptimal configuration of the radar. Toro et al. (2014) report on the results of their own adaptation to the original WERA algorithm. Their modifications comprise the inclusion of a weighting function derived by Barrick (1977b), a wind speed-dependent relation between Doppler and ocean wave frequencies, and four different parameterizations -also wind speed dependent- to scale the Doppler spectra. A linear correlation (R) of 0.73 and 0.39 m RMSE are reported for a 16-day comparison of buoy- and radar-derived wave heights, limited to cases when the wind was blowing toward the radar with a speed (U_{10}) higher than 8 ms^{-1}. Toro et al. (2014) also provide what is the only quantitative information related to the shape of the frequency spectrum retrieved by the WERA algorithm. This is represented by an estimation of the wind-sea spectral peak -a parameter that was found to agree very well with in situ measurements, showing a linear correlation (R) of 0.9 for a limited dataset corresponding to the same wind conditions referred to above.

Here, we intend to complement these rather scarce validations by providing a thorough evaluation of the results produced by the WERA software, using both the original calibration found in Gurgel et al. (2006) and a local calibration performed as part of this work. Using a longer dataset than most published validations of empirical inversion algorithms (e.g., Maresca et al., 1980; Wyatt, 1988; Heron and Heron, 1998; Essen et al., 1999; Ramos et al., 2009; Toro et al., 2014), and adding surface gravity wave spectra and energy period (T_e) to the more typical significant wave height (H_s) validations, we hope to enhance the understanding of the algorithms accuracy, strengths, and limitations. Assessing outputs extracted from three different locations within the radars coverage is expected to help determine

the spatial reliability of these measurements and contribute to the evaluation of the adequacy of HF radar for wave monitoring at wave farm installations.

4.2 Materials and methods

4.2.1 Data

The complete data set used in this chapter was collected over nine months, from March to November 2012. During this period the two radars were simultaneously operational 98% of the time. Over the operational hours, the maximum directional wave data retrieved by the inversion algorithm at any one cell within the radar coverage was 74% (Figure 4.1b). Accounting for non-directional results derived from one radar only, as well as dual information, the maximum percentage of data retrieval increases to 91% (Figure 4.1a). Over this period, the in situ devices provided data almost uninterruptedly.
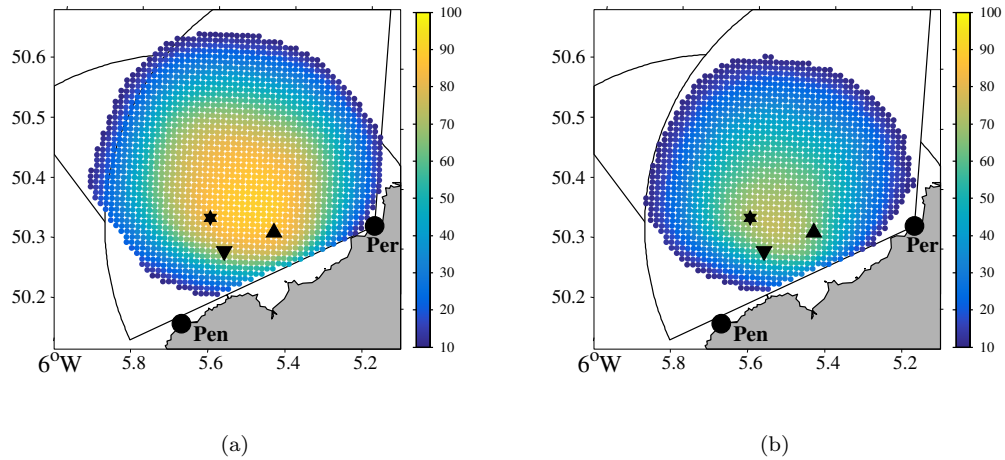
Figure 4.1: Temporal data coverage shown as a percentage of the time each cell had inverted data over a 9-month period. a) Total percentage of data return. Both directional information derived from the two radars and non-directional results obtained with only one station were accounted for. b) Percentage of directional results, obtained when both stations acquired good quality data simultaneously. Radar stations (black circles), their wave coverage (fans) and in situ mooring devices are also depicted: wave buoy (star), ADCP-W (inverted triangle) and ADCP-E (triangle).

All data sets were posteriorly divided into two sub sets, which were used to calibrate and later validate the algorithm. The training data set was collected during March, August, and September 2012. A varied group of sea states, characterized by wave heights ranging from less than 0.5 m to more than 5 m, peak periods between 4 and 20 s, and wind speeds up to 18 ms^{-1} blowing from various directions (Figure 4.2), suggests that the chosen period can provide a representative dataset for developing a relevant set of correction coefficients that can then be used to calculate the one-dimensional ocean spectrum from the radar signal. The remaining data were used to validate the results.
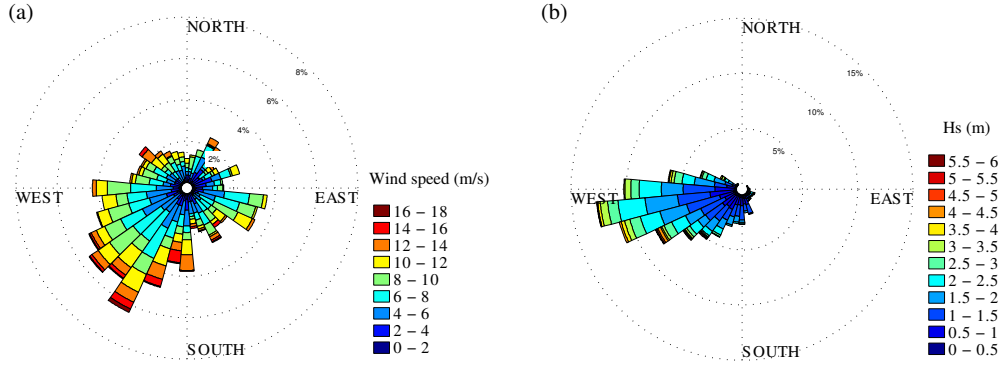
Figure 4.2: Wind and wave roses obtained with the calibration dataset, which includes three months: March, August and October. (a) Wind rose. The direction is degrees from north and follows the meteorological convention (wind blowing from). (b) Wave rose. The wave direction is also expressed as the direction the waves are coming from. The colour scale in the plots represents: (a) wind speed (ms^{-1}) and (b) wave height (m

4.2.2 Calibration of the algorithm

Following Hasselmann (1971), the algorithm presented in Gurgel et al. (2006) is based on the assumption that the continuous second-order sidebands surrounding the first-order peaks of the Doppler spectrum are proportional to the frequency

ocean wave spectrum. This simple relationship, however, was modified by introducing an angular spreading function as follows:

$$\alpha_k S_{mk} = S_k \, F(\varphi_k - \varphi_r)$$

$$\alpha_k S_{pk} = S_k \, F(\varphi_k - \varphi_r + \pi)$$

$$(4.1)$$

where α_k are the coefficients resulting from regressing radar sidebands against buoy spectra, with k representing the index of the spectral frequencies (0.05 - 0.25 Hz). Variables S_m and S_p refer to negative (m of minus) and positive Doppler shift relative to the first-order Bragg peak, respectively. The ocean wave spectrum S_k is measured in situ; F is an angular spreading function; φ_r is the radar look direction, which is defined as the angle between the radar boresight and a particular location within the radar coverage (the wave buoy in this case); and φ_k is the in situ-measured mean wave direction, both measured clockwise from north.

Gurgel et al. (2006) analyzed Equation 4.1 using different angular spreading functions, including a $\cos^2$ and a sech^2. The latter is reported to produce correlations of 0.75 - 0.9 for the positive sideband and of about 0.3 0.4 for the negative side when compared to buoy spectra. No correlation results are given for the $\cos^2$ function, but the authors state that both resulted in a similar set of regression coefficients. The correlation of the unweighted sidebands and buoy spectra was also examined and was found to result in a 10% reduction with respect to the sech^2 correlations. The regression coefficients were obtained by applying a $\cos^2$ function to approximate the angular distribution of the short scattering ocean waves. The solution of Equation 4.1 for the $\cos^2(0.5\varphi)$ is

$$S_k = \alpha_k(S_{mk} + S_{pk}) \qquad (4.2)$$

In the WERA software, the correction coefficients found by Gurgel et al. (2006) are applied to Equation 4.2 in order to calculate the ocean wave spectrum.

In their paper, Gurgel et al. (2006) state that the algorithm and correction coefficients derived using radars operating at 27.65 MHz can be used for other radar frequencies if multiplied by the squared ratio of the latter frequency and the new radar operating frequency. This correction yields a new set of coefficients that provides reasonable results for the 12 MHz Plymouth University radar, mainly in terms of significant wave height. However, rather less satisfactory estimates of wave period motivated a recalibration using data collected locally, in an attempt to further improve the results.

The radar second-order sidebands appearing in Equation 4.2, and necessary to calibrate the algorithm, were obtained using the WERA software. In the first stage of the processing performed by the WERA software, the received returns are range and azimuth sorted to grid points across the radar coverage area (see Gurgel et al. (1999a) for details), and a Doppler spectrum is generated via FFT at each grid point. In the next stage, the first-order peaks are identified for each spectrum, and the first- and second-order regions, used to estimate current and wave information, delineated. The stronger of the two Bragg peaks identified is then used to normalize the second-order sidebands surrounding it. Thereafter, Doppler frequencies of the normalized second-order sidebands are linearly transformed into ocean frequencies by subtracting the Bragg frequency, and the associated spectral amplitudes are interpolated onto a vector ranging from 0.05 to 0.25 Hz, at a resolution of 0.01 Hz. These results are stored and provided as outputs.

Using these variables as a starting point, a quality control procedure equivalent to that implemented in the WERA software was performed. As part of the process, data points with a signal-to-noise ratio lower than 25 dB in the first-order region, and lower than 10 dB in the second-order sidebands, were flagged as erroneous (see Figure 4.3a). Furthermore, spectra with an abnormally high signal in the second-order bands were also flagged, as it is likely to find interference with the first-order region in this situation. Flags for these tests were raised for 21% and

11% of the training datasets recorded at Perranporth and Pendeen, respectively. Once all the spectra on the measuring grid had been assigned a quality flag, the result at each node was calculated as a nine-point spatial average, provided all neighbours satisfy the criteria referred to above. The end products were the S_m and S_p sidebands appearing in Equation 4.2, which are averaged in space (over 9 km^2 approximately) and have a quality flag assigned to them.
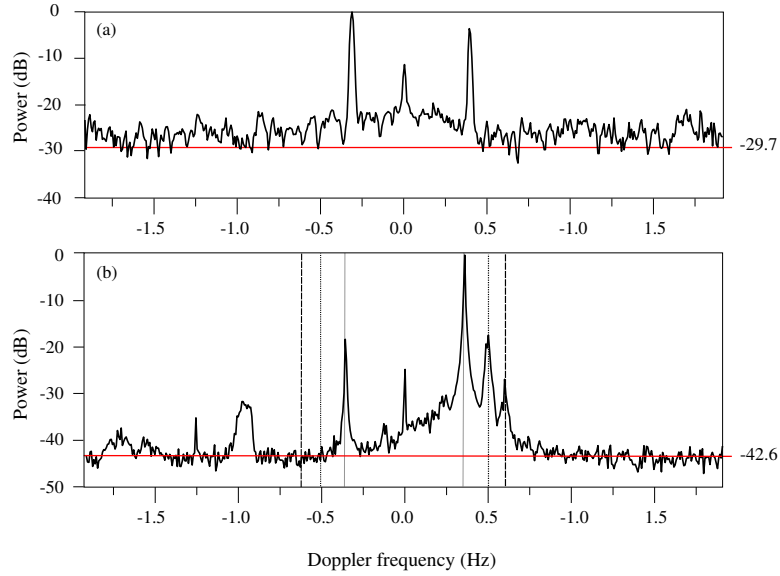
Figure 4.3: Doppler spectra computed at Pendeen. (a) Spectrum flagged as invalid due to the low signal-to-noise of the 2nd order part of the spectrum, which falls below the 10 dB limit imposed by the quality control. The horizontal line shows the noise level. (b) An example of good quality spectrum. The two solid vertical lines are the theoretical position of the first order Bragg lines. Dotted lines indicate the position of the second harmonic of the Bragg wave ($\pm 2^{1/2} f_B$), and dashed lines indicate the corner reflector peak ($\pm 2^{3/4} f_B$).

As mentioned in the previous section, Gurgel et al. (2006) found a better correlation between Doppler sidebands and in situ-measured spectra when the latter were weighted by an angular spreading function, and therefore applied a cos^2 function prior to finding the empirical parameters that allowed estimation of the ocean wave spectra from the Doppler sidebands. Here, we carried out a similar analysis, and studied the correlation between the Doppler sidebands and the buoy-measured spectra with and without the angular distribution weighting. As opposed to Gurgel et al. (2006), our results did not show a significant improvement

in terms of correlation after applying an angular spreading function; hence, the unweighted spectra were used to obtain the correction coefficients. Linear correlations (R) above 0.7 were found between radar returns and ocean wave spectra at frequencies between 0.06 and 0.1 Hz. These numbers decreased toward the high frequencies to reach values around 0.4.

The statistically significant correlations suggest that there is indeed proportionality between the energy on the radar sidebands and that on the measured wave spectra, mainly at the low frequencies. Therefore, applying a correction such as that suggested by Gurgel et al. (2006) could be a good approach for obtaining the ocean wave spectrum from HF radar measurements, especially if a persistent swell propagates over the measurement area.

The fitting procedure was formulated as a least squares minimization problem between wave spectra measured in situ and the sum of the energy in the sidebands surrounding the most energetic side of the Doppler spectra. The a_k coefficients of Equation 4.2 were found by minimizing the sum of the square of the errors between radar and in situ spectra.

4.3   Results

4.3.1   Result of the calibration

Two independent regression analyses were performed, using data collected by each of the two radar stations comprising the system. In addition, for each radar the analysis was conducted using data collected at three different points within the radar's field of view, where in situ measurements were available. The results, depicted in Figure 4.4, show that similar correction factors need to be applied at different ranges and azimuthal directions within the radar's coverage, suggesting

that the Doppler spectra do not differ significantly from each other at those loca-
tions. At the low frequencies, the main difference among the three curves derived
for Perranporth lies in the higher values obtained at the buoy node. This might
be the result of the attenuation of the radar signal with distance, as this location
is the furthest from the radar station. At Pendeen, the curves obtained for the
ADCP-W and wave buoy are similar in shape, but the former shows lower val-
ues. The mooring is the closest to the radar station, and the angle between the
prevailing swell and the radar beam is lower than at the buoy's position. The
combination of these two factors results in a higher signal backscattered from this
location, hence the lower correction coefficients.
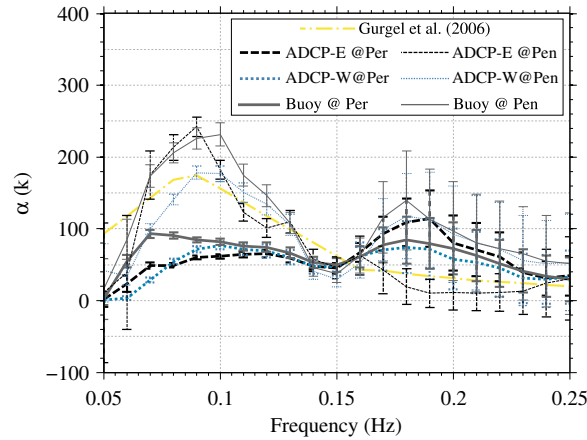
Figure 4.4: Coefficients obtained regressing radar Doppler spectra to in situ-measured
spectra recorded at Pendeen (thin lines), and Perranporth (thick lines). Three curves,
corresponding to the mooring devices deployed in the area, are shown for each station:
ADCP-E (dashed black line), ADCP-W (blue dotted line) and wave buoy (grey solid
line). The coefficients found in Gurgel et al. (2006), used in the WERA software, are
also shown (yellow dash-dotted line). The error bars are the 95% confidence intervals
of the coefficient estimation.

Around the frequencies 0.14 - 0.15 Hz, a minimum appears as a common feature
to all curves. Assuming a linear relation, such frequencies equate to a Doppler
frequency of $\pm 2^{1/2} f_B$ (the frequency fluctuation would be due to the variation in
transmitting frequency mentioned in Chapter 3), where the second harmonic peaks

(SHP) appear in the Doppler spectrum (Ivonin et al., 2006). Resulting from the resonant scatter produced by the second harmonic of the Bragg waves, these peaks do not represent the actual shape of the ocean wave spectrum which generated the scatter (Barrick, 1977b), and the minima seem to appear to compensate for this singularity. Finally, the higher variability of wind seas, as well as the noisiness of the radar data at high frequencies, both represented by the broad confidence intervals shown in Figure 4.4, are likely to be responsible for any differences between the correction coefficients above 0.17 Hz. Overall, the most noticeable discrepancy can be seen in the coefficients of the two radar stations, especially over the lower frequencies, where the values obtained using data collected by the Pendeen radar are approximately 60% higher. The prevailing westerly swell propagating across the area intersects Pendeen's beam almost perpendicularly at most azimuthal directions; a situation known to result in a lower signal as compared to that emerging from waves propagating towards or away from the radar (Wyatt, 2002), the latter being the common situation at Perranporth.

Despite the differences found, which are primarily due to the known dependency of the radar spectral signature on the angle between wave direction and radio beam direction (Lipa and Barrick, 1986), the similarity between the three sets of coefficients obtained for each station suggests that a constant curve can be a valid approximation to inverting the radar backscattered power over the measurement grid. The coefficients obtained using data acquired with the wave buoy were therefore chosen as the reference set to use for future calculations. This decision was made based on data quality, as the wave buoy was located at low angles from the boresight line of both radars, where the digital beamforming performs best.

4.3.2   Validation of results

The coefficients resulting from the above-described regressions were used to calculate the one-dimensional ocean spectrum. The calculations were performed using the average of the normalised second-order power of the two stations and their respective mean coefficients when possible, while the station-specific coefficients were applied when dual data were not available. Wave parameters were calculated by integrating the latter spectra over the full range of available frequencies (0.05 - 0.25 Hz). Significant wave height (H_s) and the energy period (T_e), were obtained using Equations 3.5 and 3.6, respectively. The results retrieved by the calibrated algorithm were then compared to in situ measurements in order to assess their accuracy. The agreement between methods is quantified in terms of the linear correlation coefficient (R), bias of the estimations, root-mean-squared error (RMSE), and scatter index (SI), all calculated using the expressions introduced in Chapter 3. In addition, we calculated the mean percentage error (MPE) as the percentage difference between the radar and in situ values divided by the magnitude of the latter, and normalised by the number of records. The MPE was computed for different wave height and period classes, in order to verify the performance of the calibration under different sea states.

4.3.2.1   Integrated parameters

Comparisons of the radar estimates against data collected by the three point measuring devices located within its footprint are presented in Figure 4.5, and summarised in Tables 4.1 and 4.2, where the results obtained with the original coefficients found in Gurgel et al. (2006) are also included. The calibrated algorithm retrieved estimations of H_s with nearly zero bias, linear correlations higher than 0.9, an average scatter index of 0.2 and RMS errors that range from 29 cm at the wave buoy coordinates to 44 cm at the ADCP-W. The higher errors found for

the ADCP-W, which was deployed at a high angle from Perranporth's boresight (45°), are probably associated with antenna sidelobes and current variability. The error is some 14% higher in the results retrieved by the original WERA algorithm, which nonetheless performed similarly to the calibrated scheme for this parameter.

Table 4.1: Summary statistics of the radar and in situ H_s comparisons. All the metrics have been calculated using the entire validation dataset (All) and only dual-radar estimations (Dual). The results obtained with the original WERA algorithm and the calibrated version (Calibr; bold numbers) are shown.

Site	Method	Bias		RMSE		SI		R		N	
		All	Dual	All	Dual	All	Dual	All	Dual	All	Dual
Buoy	Calibr	**-0.04**	**-0.03**	**0.29**	**0.26**	**0.17**	**0.14**	**0.95**	**0.96**	3192	2449
	WERA	-0.01	0.02	0.33	0.28	0.19	0.15	0.94	0.96		
ADCP-W	Calibr	**-0.04**	**0.03**	**0.39**	**0.36**	**0.23**	**0.19**	**0.91**	**0.91**	3360	2335
	WERA	0.11	0.22	0.52	0.46	0.28	0.23	0.88	0.89		
ADCP-E	Calibr	**0.09**	**0.10**	**0.33**	**0.36**	**0.21**	**0.20**	**0.93**	**0.92**	3242	2223
	WERA	0.18	0.18	0.39	0.42	0.25	0.24	0.91	0.91		

Table 4.2: Same as the previous table but for T_e estimates.

Site	Method	Bias		RMSE		SI		R		N	
		All	Dual	All	Dual	All	Dual	All	Dual	All	Dual
Buoy	Calibr	**1.00**	**1.00**	**0.68**	**0.57**	**0.09**	**0.08**	**0.82**	**0.87**	3192	2449
	WERA	1.11	1.13	0.96	0.84	0.11	0.10	0.68	0.74		
ADCP-W	Calibr	**0.70**	**0.80**	**0.87**	**0.82**	**0.11**	**0.10**	**0.71**	**0.72**	3360	2335
	WERA	1.48	1.69	1.58	1.53	0.18	0.17	0.52	0.51		
ADCP-E	Calibr	**1.00**	**1.00**	**0.78**	**0.67**	**0.10**	**0.08**	**0.78**	**0.84**	3242	2223
	WERA	1.43	1.26	0.99	0.71	0.12	0.09	0.68	0.82		

The improvement of the calibration relative to the unmodified algorithm is most noticeable in the T_e estimations, which revealed up to 30% RMS error reduction. Overestimations of this parameter seem to be linked to high speed currents (Figure 4.5b,e,h). At the ADCP-E, measurements acquired under high current speed conditions are seen to affect Perranporth's single-site estimates especially. The last column of Figure 4.5 shows the estimates of mean direction. These are independent of the regression coefficients, hence the results shown are as outputted from the WERA software. The radar wave direction is seen to have higher variability

than the in situ measurements, and the results seem to degrade with increased current speed.
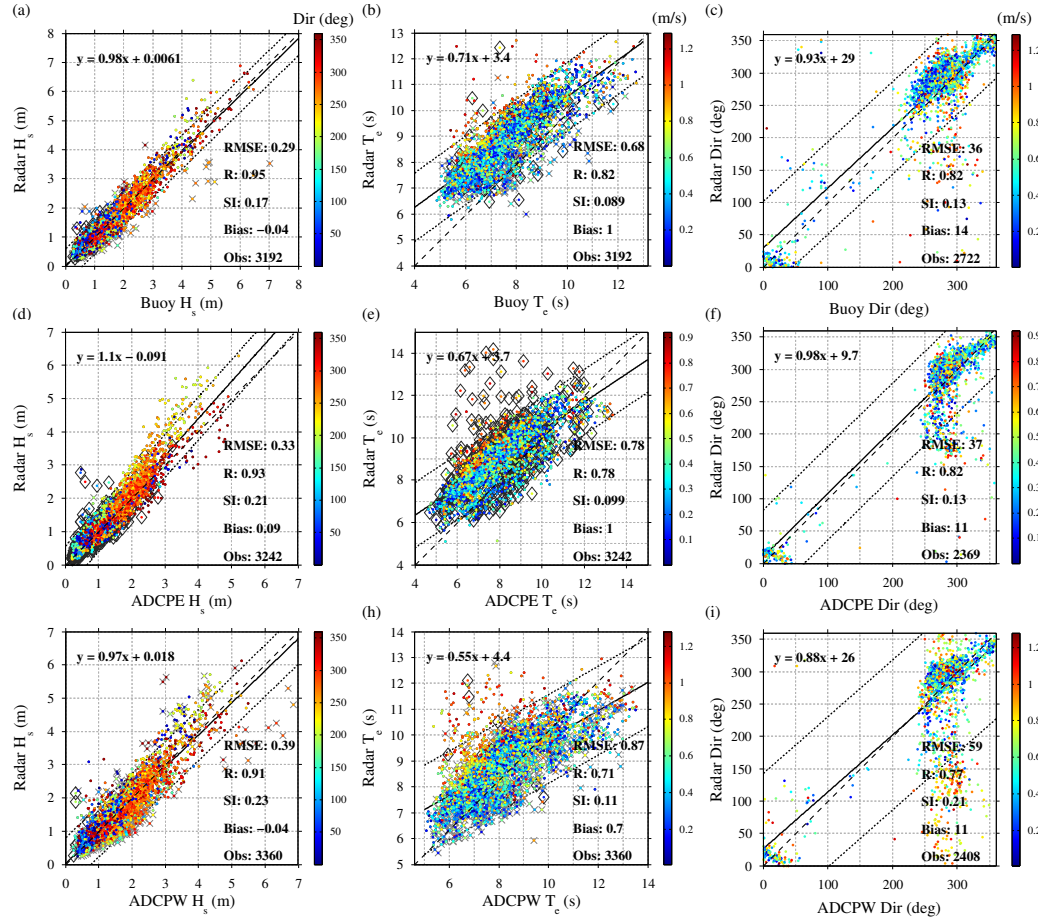
Figure 4.5: Comparison of significant wave height (left), energy period (middle) and mean direction (right) radar estimates vs. in situ measured data. The dashed line corresponds to the (1:1) line of perfect correlation. The solid line represents the least-squares regression from which the equations displayed on the figures were derived, and the dotted lines are the 95% confidence intervals about the regression line. The colour scale on the left column represents the direction towards which the wind was blowing. The T_e results (middle) and the mean direction (right) are coloured according to the velocity of the current. Dots surrounded by a black diamond correspond to single-site estimations from Perranporth, while those combined with a grey cross are results derived from Pendeen's measurements. Coloured dots without any other marker are dual-radar estimates. Results are shown for comparisons against the buoy (a-c), ADCP-E (d-f) and ADCP-W (g-i)

Figure 4.6a shows the mean percentage errors for wave height bins of 0.4 m. It can be seen that while the error on the radar's significant wave height estimations is within 10% for most wave amplitudes, deviations occur in the range 2.8-4 m

waves for comparisons against the ADCP-E measurements, which present errors closer to 20% with respect to the in situ measurements.
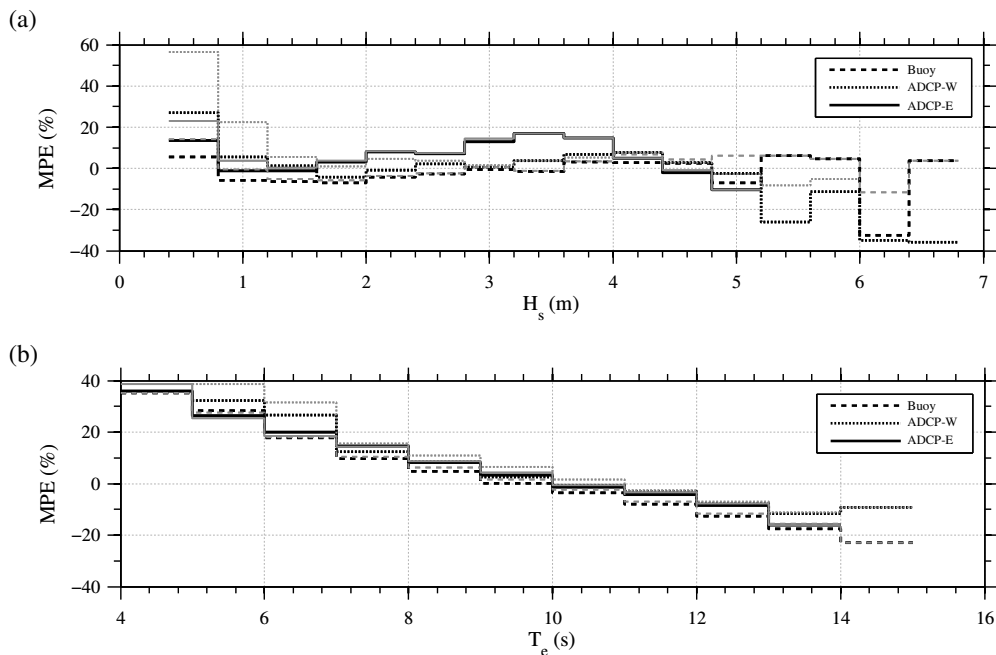
Figure 4.6: Mean percentage error (MPE) of H_s and T_e estimates. (a) MPE of 0.4 m intervals of wave height. (b) MPE of 2 s intervals of wave energy period. On both plots: Solid line, ADCP-E; dash-dotted line, buoy; dashed line, ADCP-W. Each plot contains two lines for each of the aforementioned in situ devices, grey for calculations made using only dual data, and black for calculations using all data available.

The overestimations in this range are associated with low frequency waves ($T_e >$ 9 s) and wind speeds higher than 10 ms^{-1}, blowing from the west (Figure 4.5c). The Doppler spectra recorded at both stations under these conditions (not shown) have their energy well distributed over the frequencies. However, they are peaked at the maximum of the correction coefficients and show some extra energy around 0.14 Hz. The combination of these two factors seems therefore to be responsible for the overestimations. On the other hand, the underestimation of wave heights higher than 4 m shown in Figure 4.6a is also associated with high wind speeds ($>$ 14 ms^{-1}) (not shown), but in this case, the energy containing waves are travelling from the north-northwest, aligned with the wind (see Figure 4.5c). Under these conditions, the Doppler spectra recorded at Pendeen (not shown) are dominated

by the SHP, and do not represent the ocean gravity spectra which produced the scatter. At Perranporth, the radar-to-wind angle reaches the values for which the hydrodynamic coupling coefficient is low (Lipa and Barrick, 1980). This results in a relatively weak backscatter, and as a consequence H_s is underestimated. An increase in the error can also be observed in Figure 4.6 below 1 m and until the 0.4 m minimum wave height detectable at the radar's transmitted frequency of 12 MHz. The figure also reveals the benefit of using only dual data to calculate wave height; a situation resulting in a 20% error reduction in the radar's estimations with respect to the buoy's measurements at the upper tail of the wave height distribution (6 - 6.4 m). An exception to the latter can be observed on the low wave heights obtained at the ADCP-W, where single site estimations show 30% less error than dual estimations. The reason is that, as it can be seen on Figure 4.5e, such single-site estimations are usually derived from Pendeen's measurements which, as opposed to Perranporth's, are unaffected by antenna sidelobes at this location.

The same analysis was conducted for the T_e results, which were discretised into 1 s bins. The results show accurate estimations of wave periods between 8 and 12 s, while both under- and overestimations can be observed above and below that range, respectively (Figure 4.6b). In addition, and as opposed to wave height estimations, this parameter does not show any significant improvement by using only dual-radar estimations.

Compared to the original WERA algorithm, the highest impact of the calibration was in the results calculated using data collected exclusively at Perranporth, which represent 28% and 6% of the ADCP-E and buoy validation datasets, respectively. For those cases, the results derived from the calibrated algorithm show a 26% and 31% average RMS error reduction in H_s and T_e, respectively. When using dual data, the estimations obtained with the new coefficients show a 15% average reduction in H_s RMSE and a 30% in T_e. On the other hand, the results obtained

from the signal received at Pendeen only did not show a significant improvement
with the new calibration.
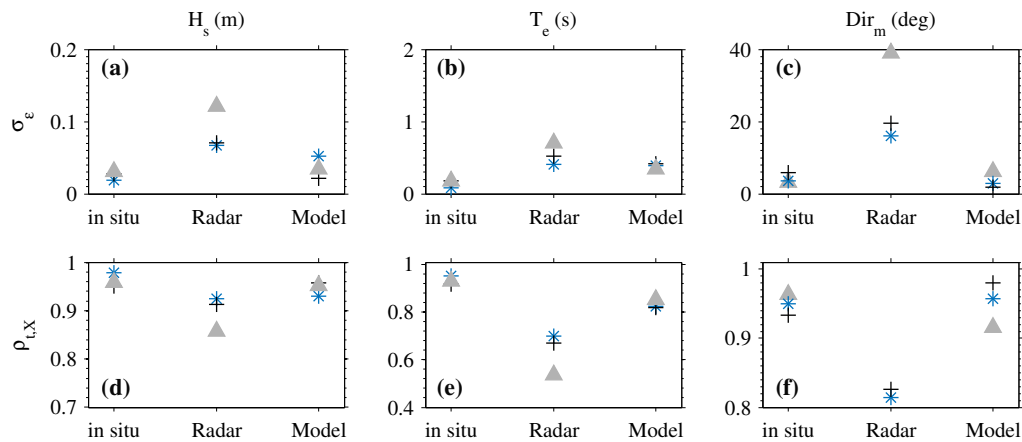
Figure 4.7: (First row): Triple collocation estimates of the error variances of the (a)
H_s, (b) T_e and (c) Dir_m estimates for the radar, the in situ measurements, and the
model products, calculated at the locations of the in situ devices: buoy (blue asterisk),
ADCP-E (black cross) and ADCP-W (grey triangle). (Second row): Extended triple
collocation estimates of the correlation coefficient between the unknown truth and the
radar, in situ, and model products of (d) H_s, (e) T_e and (f) Dir_m.

As mentioned in Chapter 2, one-sided least-squares regressions such as those pre-
sented in Figure 4.5 assume all the disparities between the two data sets analysed
are due to errors in the test variable; the radar in this case. However, the in situ
measurements are also subjected to random errors; hence the slope of the regres-
sion can be sometimes biased. An examination of the error of each of the data sets
used was therefore performed with the extended triple collocation (ETC) method
described in Chapter 3, and using the radar and in situ measurements, together
with the model products. The results, shown in Figure 4.7 indicate a higher error
variance in the radar estimates, as compared to the modelled results and in situ
measurements. As expected, the noise introduced by the effect of sidelobes and
current variability is translated into the highest variance at the ADCP-W location.
At the other two sites, the radar's random error is much closer to the other two
datasets, and correlations are high. Nevertheless, the very low errors and high
correlation to the unknown truth shown by the in situ devices, suggest that the

results of the one-sided regression discussed above are probably accurate enough in describing the radar errors, since it seems that the noise in its estimates dominates over that of the in situ measurements. In fact, the numbers obtained taking the square root of the variances presented in Figure 4.7 are in very close agreement with the RMSE that resulted from comparing radar and in situ measurements (Table 4.3).

Table 4.3: RMSE of the radar estimates of H_s, T_e and Dir_m obtained with triple collocation ($RMSE_{TC}$), and the common expression of RMSE (Equation 3.12).

	Radar@Buoy		Radar@ADCP-E		Radar@ADCP-W	
	$RMSE_{TC}$	RMSE	$RMSE_{TC}$	RMSE	$RMSE_{TC}$	RMSE
H_s (m)	0.26	0.29	0.26	0.33	0.34	0.39
T_e (s)	0.64	0.68	0.72	0.78	0.85	0.87
Dir_m (°)	36	36	40	37	61	59

4.3.2.2 Spatial comparisons

Radar wave height maps normally show a high spatial variability over the instrument measurement region. Whether this is real or a product of radar artefacts is a question that remains partially unanswered, and although the results presented in the previous section have shown that noisy results near the edge of the radars field of view may be in fact a consequence of antenna sidelobes, a complete spatial assessment of the results is essential. For that, in situ measurements acquired at two distant locations were compared to determine the variability captured by such devices. The same exercise was then conducted with radar estimates at equivalent positions, to allow for comparison against the in situ measurements. Unfortunately, whenever the ADCP-W is involved in the comparison, the results cannot be considered trustworthy due to the noise introduced by the antenna sidelobe issue mentioned earlier, so here the discussion focuses on the buoy-ADCP-E pair, deployed 12 km apart.

Table 4.4: Statistical indicators resulting from the comparison of radar-to-radar and in situ-to-in situ H$_s$ estimates. The results of the radar buoy - ADCP-E pair, referred to in the text, are shown in bold.

		Bias		**RMSE**		**SI**		**R**	
Pair	N	In situ	Radar	In situ	Radar	In situ	Radar	In situ	Radar
Buoy-ADCP-W	1863	-0.03	-0.05	0.23	0.33	0.12	0.19	0.97	0.94
Buoy-ADCP-E	**2921**	**-0.20**	**-0.08**	**0.21**	**0.34**	**0.12**	**0.18**	**0.96**	**0.93**
ADCP-E-ADCP-W	1844	0.19	0.20	0.24	0.4	0.15	0.21	0.96	0.91

Table 4.5: Statistical indicators resulting from the comparison of radar-to-radar and in situ-to-in situ T$_e$ estimates. The results of the radar buoy - ADCP-E pair, referred to in the text, are shown in bold.

		Bias		**RMSE**		**SI**		**R**	
Pair	N	In situ	Radar	In situ	Radar	In situ	Radar	In situ	Radar
Buoy-ADCP-W	1863	0.09	-0.06	0.65	0.66	0.07	0.77	0.93	0.86
Buoy-ADCP-E	**2921**	**-0.20**	**0.10**	**0.56**	**0.61**	**0.07**	**0.07**	**0.94**	**0.88**
ADCP-E-ADCP-W	1844	0.35	0.5	0.62	0.89	0.07	0.10	0.94	0.80

The in situ devices exhibited highly correlated measurements, which show almost no bias between the wave buoy and ADCP-W in either H$_s$ (Table 4.4) or T$_e$ (Table 4.5). Although still highly correlated, the measured conditions at the ADCP-E are smaller, both in terms of H$_s$ and T$_e$. Such modification of the wave field is due to its interaction with the varying seabed and possibly the tidal flow, and might be in fact responsible for some of the error on the radar estimates at the ADCP-E location. The highest waves (> 3 m) measured by the buoy, were seen to suffer an amplitude reduction when measured by the ADCP-E, which is represented by a 0.2 m bias (Table 4.4). Although this is also the case on the radar-to-radar comparison, the difference is smaller (0.08 m bias). In general, the radar-to-radar comparisons of the buoy - ADCP-E pair revealed 30% more scatter (SI), and 60% less bias on the H$_s$ results than the in situ comparisons (Table 4.4). The T$_e$ estimations derived from the radar are 7% less correlated between the two locations (Table 4.5) than the in situ pair, and unlike the latter do not show smaller T$_e$ measured at the ADCP-E.

In order to provide further insight on the spatial accuracy of the radar parameters,

these were compared against the outputs of the model described in Chapter 3. The correlation between data sets was obtained using Equation 3.14, and 3.19 for the mean wave direction. The results (Figure 4.8) show highly correlated estimates of all three parameters, particularly in an area covering approximately a 30° lobe around Perranporth's boresight. Wave period shows the lowest correlation to the modelled results, especially south of the ADCP-E and wave buoy, where the line demarcating the decline in correlation seems to actually follow the bathymetric contours. Measurements in most of this area would be affected by the same issues seen when comparing the radar outputs to the ADCP-W measurements. The relatively high angles from Perranporth's boresight, together with strong currents, which affected by the bathymetric contours travel in slightly different directions than the current at the same range but further north (see Chapter 7 for further details on the current field), are all factors affecting the measurements in this area. Additionally, the somehow limited representation of the surface current in the model probably results in less accurate outputs around this area. However, as shown in Figure 4.7, the modelled products resulted in lower errors than the radar when examined at the ADCP-W location, pointing to the radar measurements as the most affected by noise in this area. The same result is seen on the mean direction comparison, which while better correlated to the model, also shows a decline in the agreement in the southern-most part of the measurement area.

(a) (b) (c)
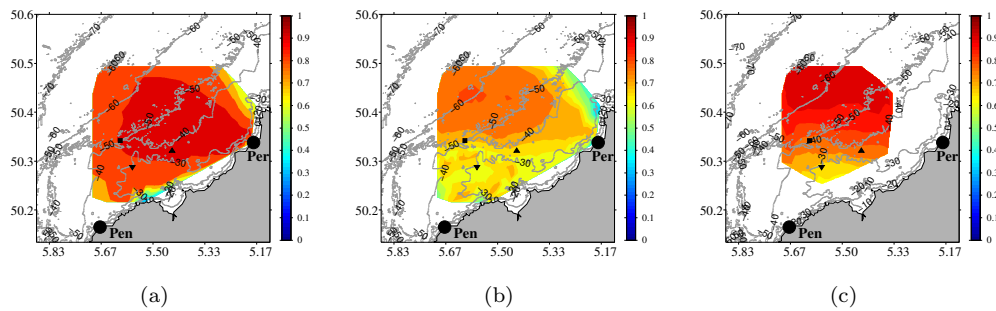
Figure 4.8: Linear correlation coefficient between radar and model estimates of a) Significant wave height, b) Energy period and c) Mean wave direction. Model and radar grid points closer than 500 m were used for the computations. The positions of three in situ mooring devices deployed in the area are also displayed: wave buoy (star), ADCP-W (inverted triangle) and ADCP-E (triangle)

4.3.2.3   Frequency dependent parameters

This section addresses the accuracy of the spectral estimations obtained with the radar. Average radar and in situ spectra were computed for the entire validation period, and for two subsets corresponding to low and high frequency systems. In order to obtain the latter, the spectra were crudely divided into two frequency bands, corresponding to swell and wind seas, establishing the frequency separation at 0.12 Hz. The results, depicted in Figure 4.9, show that the calibrated algorithm results in an accurate estimation of the average spectral shape and amplitude of the entire validation dataset (Figure 4.9a), as well as the swell cases (Figure 4.9b), only with a slight overestimation of 0.6 m^2 Hz^{-1} at the peak of both spectra. A different picture is observed for the frequency band higher than 0.12 Hz (Figure 4.9c), where the peak frequency is underestimated by 0.02 Hz, explaining the overestimation of the lowest periods seen in the previous section. The accuracy of the radar spectral estimations is further examined in the second row of the same figure, which depicts individual realisations of three different sea states. Figure 4.9d is an example of a single-site estimate derived from Perranporth's signal, and shows the improvement achieved using station-specific coefficients for the inversion in that situation (yellow spectrum in Figure 4.9d). As in the average results, the low frequency system (Figure 4.9d) is well represented by the radar, which reproduces both the shape and amplitude of the spectrum quite accurately. This translates in a H_s estimate with only 10 cm error, and an agreement on the T_e obtained with both techniques (11 s). Wind information obtained from a wave model (Boudiere et al., 2013) indicates that a 8.2 $m\,s^{-1}$ wind was blowing from the north-east direction, and the peak wave direction measured by the wave buoy was west-northwest. As already seen in the average spectrum, the wind sea example (Figure 4.9e) reveals a spectrum with its peak shifted to a lower frequency with respect to the buoy. However, the energy contained in both spectra is the same, and the significant wave height is accurately estimated by the radar.
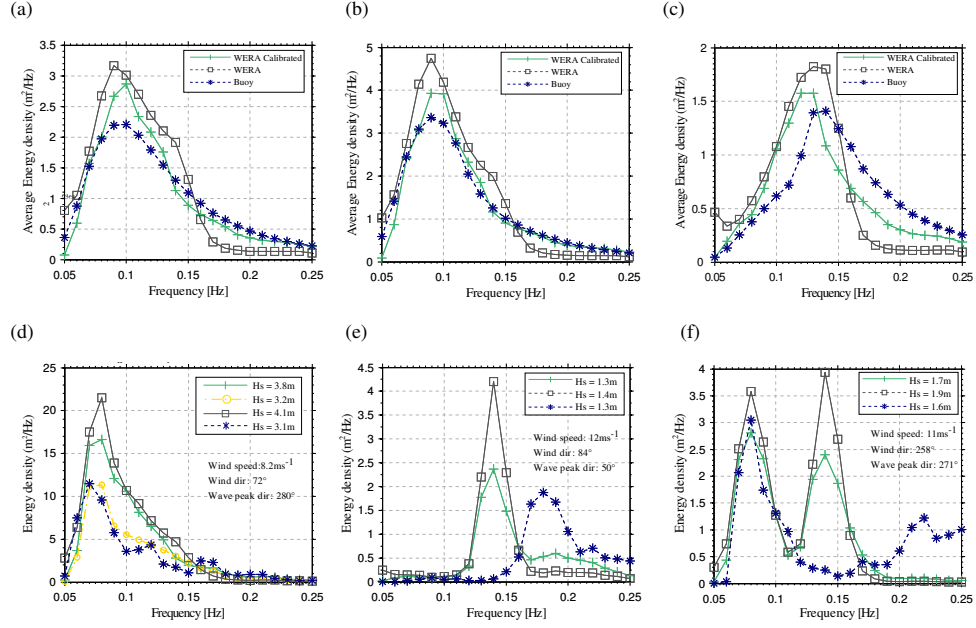
Figure 4.9: In situ-observed and radar-retrieved energy density spectra. Blue line (*) denotes the in situ measurement, green line (+) the spectrum obtained with the calibrated algorithm, grey line (□) is the spectrum retrieved by the WERA software, and the yellow line (o) in plot d) is the spectrum obtained with Perranporth's station-specific coefficients. (a) Time averaged spectrum calculated with all the validation data set. (b) Time averaged spectrum of swell cases (f_p <0.12 Hz). (c) Time averaged spectrum of wind seas (f_p >0.12 Hz). The bottom panel shows single examples of (d) a low frequency system arriving from the west recorded at the buoy location at 2305 UTC 26 May 2012. The radar estimate was calculated from the signal recorded at Perranporth only, (e) a wind sea recorded at the buoy location at 1005 UTC 23 Sep 2012 and (f) a mixed sea recorded at the ADCP-E location at 0005 UTC 03 June 2012.

Finally, Figure 4.9f shows a mixed sea represented by a double peaked spectrum. Both wind and peak waves are from the west, with the former blowing with a speed of 11 ms^{-1}. The spectrum can be seen as a combination of the two previous cases, with the low frequency system accurately represented both in frequency and amplitude, and the high frequency peak shifted to a lower frequency, which coincides with the SHP.

4.4   Discussion

The results presented in the previous sections revealed deviations in the radar estimates, which were mainly related to single site estimations, sidelobe contamination, or the occurrence of wind seas. In this section, these and other factors potentially affecting the performance of the algorithm are discussed.

First of all, and bearing in mind that the Doppler signature depends on factors such as the radar-to-wind direction (Lipa and Barrick, 1986), the distance from the radar station (Ramos et al., 2009), or the bathymetry (Lipa et al., 2008), all of which vary across the radar footprint, a potential source of error arises from calibrating the algorithm exclusively using measurements collected at its centre. In order to determine whether this introduces a significant error to the results, these were re-calculated using the regression coefficients derived from the ADCP-E measurements. The results obtained were then compared against the validation dataset measured by that same device (ADCP-E), and revealed a 3% reduction in the H_s error and 1% in T_e, with respect to the estimates obtained with the correction coefficients derived from the buoy measurements. This suggests that in spite of the differences in azimuth (30° variation in Pendeen's look direction), range (10 km difference from Perranporth's station) and depth ($\approx$ 20 m) between these two locations, using a constant set of regression coefficients does not significantly increase the error in the estimates.

Another factor found to affect the quality of the results was the use of a single radar to perform the calculations. Among the single-site estimations, those derived from the radar located at Perranporth are often closer to the in situ measurements. Furthermore, the results of this station show differing quality depending on the direction of both wind and waves. When the two are aligned, travelling towards the radar, and roughly parallel to its beam, the results provide a better fit to the in situ measurements, and the single-site estimations of T_e are strongly correlated

to the ADCP-E and buoy measurements (R = 0.9). In addition to the stronger signal recorded at the radar when the waves travel parallel to its main beam (Wyatt, 2002), Violante-Carvalho et al. (2004) found a stronger non-linear interaction between short scattering waves and swell when the latter is aligned with the wind. Such non-linear interactions have been found to be of importance in defining the swell peaks in the Doppler spectrum (Shen et al., 2013), thus conditions enhancing their occurrence are likely to increase the quality of the results, as observed.

The less satisfactory results obtained at Pendeen are related to the perpendicularity between this station's beam and the prevalent westerly swell waves throughout most of the radar coverage. As opposed to what was described in the previous paragraph, when the angle between the waves and radar beam approaches 90°, the non-linear interactions between short scattering waves and swell are weak (Lipa and Barrick, 1980). As a consequence, the energy of the low frequency part of the spectrum is underestimated. An attempt to improve the results was made by finding different scaling curves (alpha coefficients in Equation 4.2) depending on wind direction, a relevant factor in defining the Doppler spectrum, already reported to have an important influence on the results (Haus et al., 2010). Using a specific coefficient set for cases when the wind was blowing from the western sector (225-315° N), which are prone to produce the highest underestimations, reduced the RMS error of the radar energy period estimates with respect to the wave buoy by 60%, while wave height was 10% closer to the in situ measurements. However, the shape of the spectra obtained after applying the new coefficients closely matches that of the new scaling curve, which is imposing a certain shape on the low frequency part of the spectrum, where there was barely any energy. The effect of this correction therefore warrants further research and discussion, both of which are beyond the scope of this thesis.

In addition to the above, there are spatial variations on the quality of the results,

which was seen to degrade from the buoy to the ADCP-W, both in the original estimations retrieved by the WERA algorithm and the hereby proposed calibration. Because the ADCP-W was deployed at a high angle from Perranporth's boresight, the radar signal backscattered from that point is likely to be affected by antenna sidelobe contamination. Haus et al. (2010) have addressed similar geometries, and found that at angles higher than 45° sidelobe returns may be interpreted as the second order peaks, and produce spurious wave estimates. Restricting the outputs to grid nodes located at angles lower than 45° from the boresight of both stations, seems therefore essential to avoid noisy estimates. Further investigation of the spatial accuracy of the radar results was provided as a correlation analysis against the products of a wave model. The results indicate a better agreement of wave period and significant wave height around a 30° arc centred at Perranporth's boresight. Correlation of the two parameters was seen to decrease at the southern part of the domain, where the effect of the current field and antenna sidelobes affect Perranporth's measurements. It was also hypothesised that the model is less accurate on that area, owing to the complex bathymetry and the stronger surface current resent on that area. However, the ETC results confirmed that the error variances of the radar's estimates were higher than those of the modelled products, which were also better correlated to the unknown truth. It can be therefore concluded that the lower correlations can be attributed to noise in the radar estimates.

It has been shown that the WERA algorithm has a limit on the accuracy of period estimations at both ends of the frequency spectrum, either with its original settings and after calibration. The underestimation of the longest swells seems to be in part related to the use of a prescribed set of coefficients to scale the second-order frequency bands. This may impose a certain shape on the spectra, which are preferentially peaked at the maximum of the correction factors, around 0.09-0.1 Hz. Additionally, the peaks generated by these very long waves tend to merge with the first-order region of the spectrum, ultimately causing the underestimation.

On the other hand, the overestimation of the lowest periods seems to be related to a general inefficacy of the WERA algorithm in describing wind seas. The algorithm assumes a linear dependency between Doppler and ocean wave frequencies, a simple relation that, even though does not agree with theory (Forget et al., 1981), can be a good approximation for long ocean waves. Characterised by small wave numbers, the relation describing their interaction with a higher frequency component to give a Bragg scatterer with wave vector $-2k_0$ can be approximated as (Shen et al., 2013),

$$|\mathbf{K_w}| = |\mathbf{K_B} - \mathbf{K_S}| \approx |\mathbf{K_B}| \qquad (4.3)$$

where K_s and K_w are the wave vectors of the two interacting waves (swell and wind, respectively), and K_B is the Bragg wave vector. The swell frequency can therefore be approximated as,

$$\omega_d \approx m_1\sqrt{g\mathbf{K_s}} + m_2\sqrt{g\mathbf{K_B}} = m_1\omega_s + m_2\omega_B \qquad (4.4)$$

where ω_d is the Doppler frequency, and m_1 and m_2 represent the sign of the interaction. The above approximation is not valid at higher frequencies, thus the Doppler and ocean wave frequencies will not be equivalent. This may therefore be partially responsible for the inaccuracies found in the high frequency band of the spectra calculated assuming a linear relation between Doppler and ocean frequencies.

When wind seas occur, there seems to be a tendency of producing spectra peaked at 0.14 - 0.15 Hz (i.e. Figure 4.9e). As explained in section 4.3.1, these peaks are related to the resonant scatter produced by the second harmonic of the 12.5 m Bragg ocean waves travelling towards and away the radar station. This is illustrated in Figure 4.10, where it can be seen that winds blowing from sectors centred at the north and south generate a peak at 0.14 Hz on the positive and negative

Doppler sidebands measured at Pendeen. This situation is replicated at Perranporth, but for winds blowing from the west and the east. The occurrence of these peaks is well described in the HF radar theory (Barrick, 1977b), and their effect is usually corrected for by a weighting function also developed as part of Barrick's (1977) work. In the approach used here, the SHP are partially compensated for by a minimum value in the correction coefficients (Figure 4.3). However, these do not retain the Doppler frequency dependence, while the weighting function does. Additionally, multiplication of the Doppler spectra by the correction coefficients is performed after the second-order energy has been interpolated onto the vector of ocean frequencies obtained by subtracting the Bragg frequency, and that might be spreading the SHP energy onto adjacent frequencies. Toro et al. (2014) combined the inversion approach of Gurgel et al. (2006) with Barrick's weighting function. This modification, along with a wind speed dependant transformation between Doppler and ocean frequencies, might in part have been responsible for the better representation of the high frequency part of the spectrum obtained by Toro et al. (2014), which is exemplified by a correlation of 0.9 between the radar and in situ wind-sea spectral peak. Nevertheless, due to the limited range of wind conditions addressed by Toro et al. (2014), further research is needed to determine the suitability of their modifications for a broader spectrum of wind and wave conditions. Such an analysis is, however, beyond the scope of this work.

It is worth mentioning that in spite of the spectral shape discrepancy between the in situ- and radar-measured spectra, accurate wave height estimations are routinely retrieved under the conditions shown in Figure 4.10, when the spectral energy is mostly concentrated around 0.14 - 0.15 Hz. This seems to be in accordance with Zhou and Wen (2014), who found strong correlations between the ratio of the SHP to the first-order Bragg peaks, and the significant wave height. They fitted a linear regression model between in situ-measured wave height and the normalised SHP energy, and used it to retrieve estimates that presented a 0.34 and 0.26 m

standard deviation for single and dual radar estimations, respectively. Here, using Doppler spectra which had their maximum and most of their energy at either 0.14 or 0.15 Hz, we found RMS errors of 0.25 m and 0.55 m for the buoy and ADCP-E datasets, respectively.
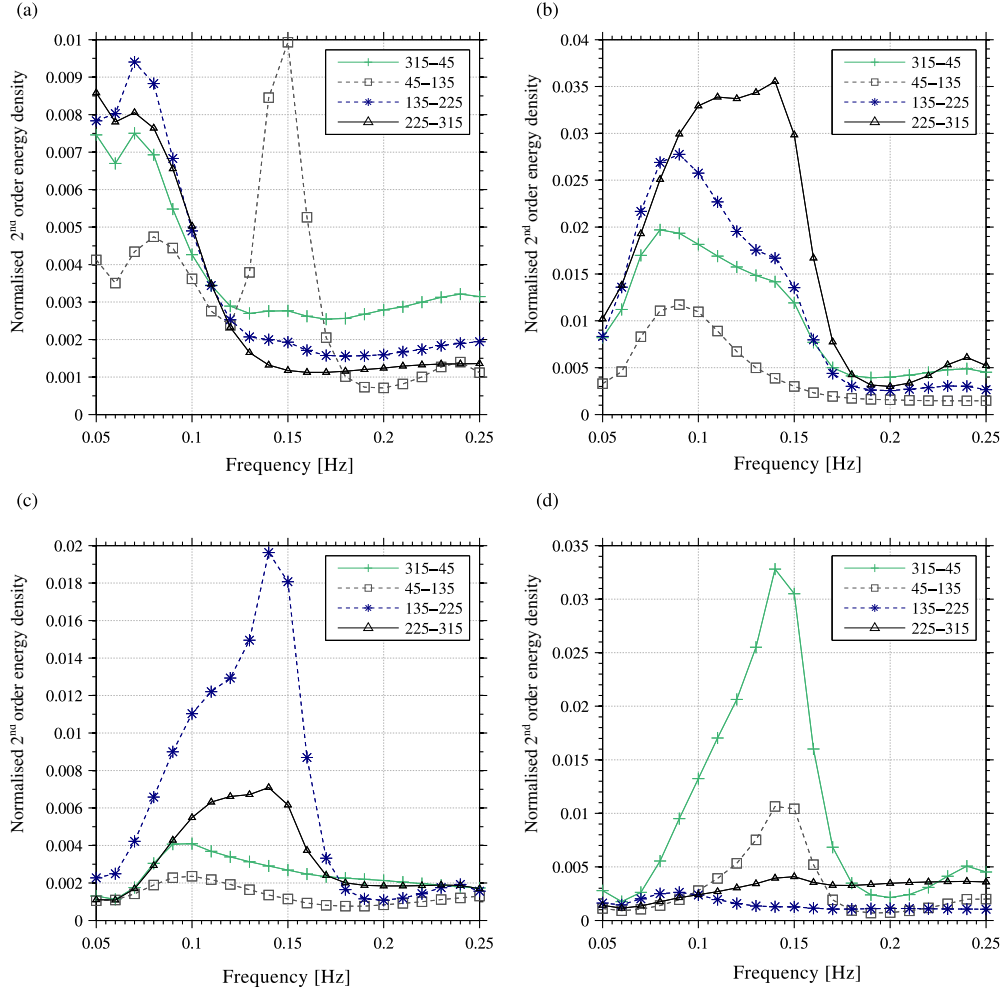
Figure 4.10: Nine-month averages of Doppler 2nd order sidebands measured at the buoy location and discretised by wind direction. (a) Negative sideband at Perranporth. (b) Positive sideband at Perranporth. (c) Negative sideband at Pendeen. (d) Positive sideband at Pendeen. The Doppler sidebands are shown as outputted from the WERA software. Wind directions are as specified in the legend and expressed following the meteorological convention.

4.5   Conclusions

An empirical algorithm used to retrieve wave spectra from HF radar returns has been presented and calibrated for the area where the radar is deployed. By conducting the longest quantitative validation of one of such empirical algorithms, and adding wave spectra and period to the more typical wave height comparisons, this work has provided a deeper insight into the algorithm's skill and the source of any inaccuracies. The validation of the results demonstrated that, locally calibrated, the algorithm performs better than in its original form in all metrics considered here. Additionally, the results show that the error associated with using a uniform set of calibration coefficients for the entire radar coverage is less than 9%, at the locations examined.

The improvement obtained with the new coefficients is most noticeable on the T_e estimations, and more specifically, on the results obtained using data from Perranporth's station only, which see their error notably reduced by 25% in the case of wave height, and by 30% for the wave period. Attempts to improve Pendeen's single estimations have also been undertaken by using correction factors fitted with data collected by that radar only, as well as introducing a specific set for westerly blowing winds, associated with the highest underestimations of H_s. However, the weak signal recorded, and an almost invariable shape of the Doppler spectra, limit the retrieval of reliable wave data from this station. The aforementioned invariable shape of the Doppler spectrum seems to be associated with a major effect of the second harmonic peaks, which under certain conditions can mask the rest of the Doppler spectrum structure. The inclusion of a weighting function, such as that proposed by Barrick (1977), might therefore be necessary to correct for this frequency localized problem.

In an attempt to determine the spatial reliability of the radar estimations, in situ measurements acquired at two locations 12 km apart were compared against each

other, in order to determine the variability captured by such devices. The same exercise was then conducted with radar estimations at equivalent positions. The in situ devices revealed highly correlated measurements between the two points, and a reduction of the highest wave heights and periods from the deeper to the shallower location. Although this is also the case on the radar-to-radar H_s comparison, the bias is 12% lower. The T_e radar estimations are only 6% less correlated than the in situ pair, but the period reduction between points is not evident. Despite the differences mentioned, the point measurement devices and the radar seem to capture the same variability between two distant points, and considering the small differences found in the error variances obtained with triple collocation for the wave buoy and ADCP-E sites, it seems reasonable to assume that in the absence of instrumental error derived in this case from sidelobe issues, most differences can be attributed to the differing measuring technique (Krogstad et al., 1999).

The results presented hereby point to the setting of the Plymouth University radar as adequate for wave estimation on this area, especially for dual estimations. Single-site retrieval of wave spectra, on the other hand, has proven to be more challenging, particularly at the station looking roughly perpendicularly to the direction of travel of prevailing swell waves. However, the inclusion of its measurements was beneficial for dual functioning, as it diluted directional effects on the results. The main limitation of the algorithm has been found to be related to the estimation of both, long period waves (> 12s) and wind seas (< 6s), which are over- and under-estimated, respectively. Significant wave height, on the other hand, has proven to be a very robust measurement, especially when the returns from the two stations are combined, which resulted in correlations above 0.9 at the three locations examined, including one grid point affected by antenna sidelobe contamination.

Chapter 5

Theoretical Estimates of Two-Dimensional Wave Spectra

5.1 Introduction

The algorithm included in the Seaview software (Wyatt, 1990) is based on the numerical inversion of the non-linear integral equation relating the HF radar backscatter and the ocean wave directional spectrum (Equation 2.10). The accuracy of its results has been extensively examined in several publications (i.e. Wyatt et al., 1999; Wyatt et al., 2003), some of which were reviewed on Chapter 2. The results, which in general are very satisfactory, have revealed limitations that were mainly related to the theory that underpins the inversion, or derived from inadequate radar configurations. As mentioned before, the longer integration time period used to obtain the radar estimates analysed in this work is expected to mitigate the contribution of the latter through reducing the errors derived from sampling variability, which in turn will allow quantification of the contributions of other known limitations, as well as the ranges for which reliable data can be obtained.

5.2   Materials and methods

5.2.1   Wave inversion algorithm

The algorithm is an iterative scheme that is initialized with a Pierson-Moskovitz spectrum and a cardioid model for the directional distribution, both of which are defined using information directly extracted from the radar-measured Doppler spectrum (Wyatt et al., 1985). This initial guess of the ocean wave spectrum is then used to derive a Doppler spectrum by integration of the equation relating the two (Equation 2.10). The integrated result is then compared to that measured, and if the spectra differ from each other, the initial estimate of the ocean wave spectrum is adjusted in the following iteration until a certain convergence criterion is met (Wyatt, 2000).

The above process is performed as long as the SNR of the second order Doppler spectrum is higher than 15 dB, and the amplitude of the local minima around the strongest Bragg peak is less than 3 dB. The result is a wave number directional spectrum with varying wave numbers and 30 directions. The reason why the spectrum is not always calculated over a fixed band of wave numbers is the linearization performed before inverting the second order Doppler spectrum, which limits the maximum frequency obtainable depending on factors such as the transmitting frequency, the intersection angle between the radar beams, and the wind direction (Middleditch, 2013).

5.2.2   Data

Data collected between April and November 2012 (Figures 5.1 and 5.2) were used to establish the accuracy of the Seaview results through comparison against in situ measurements and modelled products. During the 8-month period, the two

radars were simultaneously operational 98% of the time. The maximum wave data return of the inversion algorithm during the operational hours at any one cell within the radar coverage was 55% (Figure 5.1). Low data return was found to be associated to benign wind conditions, which result in low signal-to-noise ratios (SNR). Under wind speeds between 0 and 4 m s^{-1}, the data availability at the three cells where the in situ devices were deployed (see Figure 5.1) did not exceed 12%. Wind direction seems to also have an effect on data availability, and the highest rate of success on the inversion is attained when the wind is blowing from the west. In that situation, there were data inverted 60% of the time, while this percentage decreased to about 40% when the wind was blowing from the three remaining quadrants.
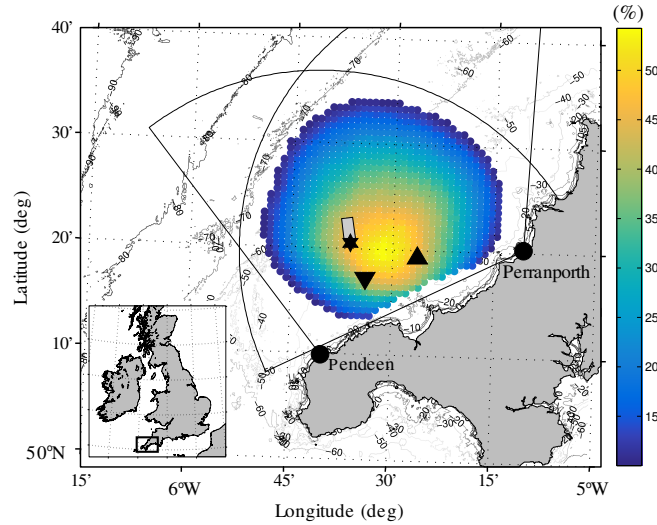
Figure 5.1: Radar stations (black circles), their coverage (fans) and measuring grid. Depth contours also shown and expressed in meters. The temporal data coverage of each radar cell is shown as a percentage of the time each cell had inverted data. The in situ mooring devices are also depicted: wave buoy (star), ADCP-W(inverted triangle) and ADCP-E (triangle). The grey rectangle delimits the Wave Hub test site for marine renewable energy (MRE) devices.
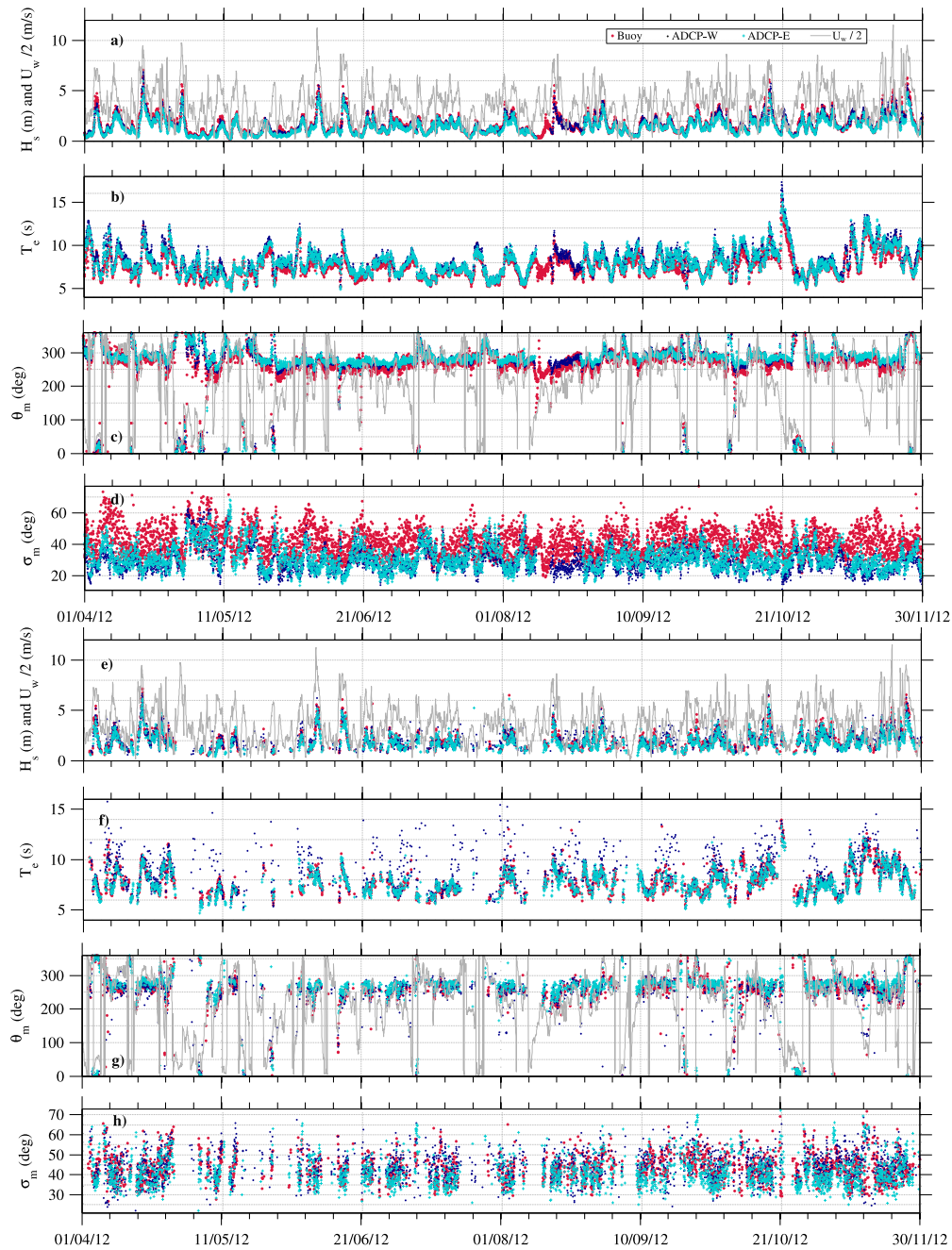
Figure 5.2: Wave parameters measured in situ (a-d) by the wave buoy (red star) and ADCPs (ADCP-W in dark blue dots and ADCP-E in light blue crosses) from April to November 2012. The same is shown in panels (e-h), but the results were obtained with the radar. Panels (a) and (e) show the significant wave height and the wind speed (gray line). Panels (b) and (f) are the energy period. Panels (c) and (g) show the wave direction (direction of approach) and the wind direction (gray line), and panels (d) and (h) depict the mean directional spreading.

The wave number spectrum retrieved by Seaview as described in the previous section was posteriorly converted into the directional frequency spectrum using

the wave dispersion relation as follows:

$$S(f, \theta) = S(k, \theta) \frac{4\pi k \sqrt{gk \tanh kd}}{g \tanh kd + gkd \operatorname{sech}^2 kd} \tag{5.1}$$

where,

$$f = \frac{\sqrt{gk \tanh kd}}{2\pi} \tag{5.2}$$

The frequency spectrum was obtained integrating the result of Equation 5.1 over the available range of directions. Finally, this spectrum was interpolated to a 0.01 Hz resolution over the frequency range 0.05 - 0.25 Hz. Wave parameters were obtained from the frequency spectra and the first two directional Fourier coefficients recovered from the directional spectra, as described in Chapter 3. The time series of significant wave height (H_s), energy period (T_e), mean direction (θ_m) and mean directional spreading (σ_m) derived from the in situ and radar measurements are shown in Figure 5.2. The calculations were performed for the whole frequency range (0.05 to 0.25 Hz) and three additional sub-ranges; 4 s to 6 s, 6 s to 10 s, and 10 s to 20 s, using Equations 3.5 to 3.8, presented in Chapter 3.

5.2.3   Validation methodology

5.2.3.1   Integrated parameters

Common error metrics were used to evaluate the agreement between radar- and in situ-measured wave parameters, and the results are graphically represented in a Taylor diagram (Taylor, 2001). The symbols are placed in the diagram according to their correlation coefficient (Equation 3.14), and normalized standard deviation,

$$NSTD = \frac{\sqrt{\frac{1}{n} \sum_{i=1}^{n} (y_i - \bar{y})^2)}}{\sqrt{(\frac{1}{n} \sum_{i=1}^{n} (x_i - \bar{x})^2)}} \tag{5.3}$$

In addition to the above, circular statistics were used to evaluate the mean direction and spreading parameters. The toroidal correlation was calculated with Equation 3.19 and the circular standard deviation (Equation 3.18) replaces its linear counterpart for these two parameters.

The above analyses are complemented by an investigation of the random errors associated to each of the data sets used for comparison. The ETC method introduced in Chapter 3, provides an idea of the variances of the random errors associated to the radar, model and in situ measurements, and will help to determine whether the one-sided regressions performed in order to obtain the descriptive statistics enumerated above are the correct approach.

5.2.3.2   Frequency dependent parameters

Validation of either wave models or remote sensing wave products is generally based on comparisons of the bulk wave parameters derived from the wave spectrum, such as those provided in the previous section. However, agreement on the integrated parameters obtained with different measuring techniques does not ensure correspondence on the spectra from which they are derived. Inspection of graphical representations of cases associated to a variety of meteorological conditions, average spectra, or spectral ratios, are among the most common approaches to comparison between spectra derived from different methods. A more comprehensive technique, based on the study of the spectral distribution of the energy density, has been developed as part of the Coastal Data Information Program (CDIP). The method uses the energy in the frequency spectrum and the first four Fourier coefficients of the directional energy distribution. The spectrum of each of the data sets compared is discretized in frequency-energy bins, and calculations are performed on the data that falls in each of these bins. Here, we limit the analysis to the spectra energy content, mean wave direction and directional spread,

calculated from the lower order Fourier coefficients. To express the dissimilarities between the two methods, we calculate the difference between both measurements and normalize it by the average value of the two,

$$\Delta = \frac{\text{Radar - in situ}}{\frac{1}{2}(\text{Radar + in situ})} \tag{5.4}$$

The result of the above equation is symmetric about zero and will take a positive value when the radar measurement is higher than the in situ value and vice versa. In addition, we used the methods presented in Dabbi et al. (2015). These are based on the parallel comparison of two parameters, which according to the authors can give valuable information about the differences in magnitude or shape between two spectra. Differences in wave height are studied together with differences in maximum spectral energy, and give an idea of the dissimilarities in spectral areas. In addition, differences in peak frequency and maximum energy, give an idea of any frequency offsets. The aforementioned parameters are complemented with measures of the mean width deviation, skewness and kurtosis of the wave spectrum.

5.2.3.3 Directional spectra

Direct comparison of directional spectra is not a straightforward task (Krogstad et al., 1999) and qualitative comparisons, based on the description of the graphical representation of the two types of results, is the common approach to this exercise. Here we provide a detailed analysis of three representative cases, with the aim of capturing the behaviour of the algorithm under different conditions. These include the longest swell recorded over the period analysed, a bimodal sea state formed by a low frequency system and a wind sea both very close in frequency and direction, and a sea state formed by a weak south-westerly swell and a north easterly wind sea.

5.3   Results

5.3.1   Integrated parameters

Figure 5.3 shows the results of the above metrics for the frequency bands mentioned in the text (Figures 5.3a to 5.3c) and for the full range of available frequencies (Figure 5.3d). The colours represent the three individual in situ devices, and each symbol corresponds to a different wave parameter. The full straight lines show the correlation coefficients between radar and in situ measurements, and the dotted arcs correspond to the standard deviation of the radar estimates normalized by the in situ value. Only records common to all devices have been used for the calculations.

Significant wave height is consistently well estimated across all frequency bands. Standard deviations are close to those of the in situ devices for the energy containing waves (Figure 5.3b) and the full range of frequencies (Figure 5.3d), and correlations (R) are close to 0.9 or above. The locally generated wind waves exhibit the lowest correlation to the in situ measurements (between 0.8 and 0.86), as well as a greater variability, represented by a standard deviation 1.5 times higher than the in sitiu values.

The results for the energy and mean periods are very similar between them and show the same pattern seen for the significant wave height, with correlations above 0.9 for the bulk of the energy spectrum and around 0.8 for waves between 6.7 and 10 s. The results degrade at the lowest frequency band, where the radar shows lower standard deviation than in situ measurements, and correlations decrease to values between 0.4 and 0.6. On this same frequency band, the poorest agreement appears on the ADCP-W comparison. As explained in the previous chapter, this is a result of antenna sidelobes and current variability, which introduce spurious energy at the low frequencies of the wave spectra.
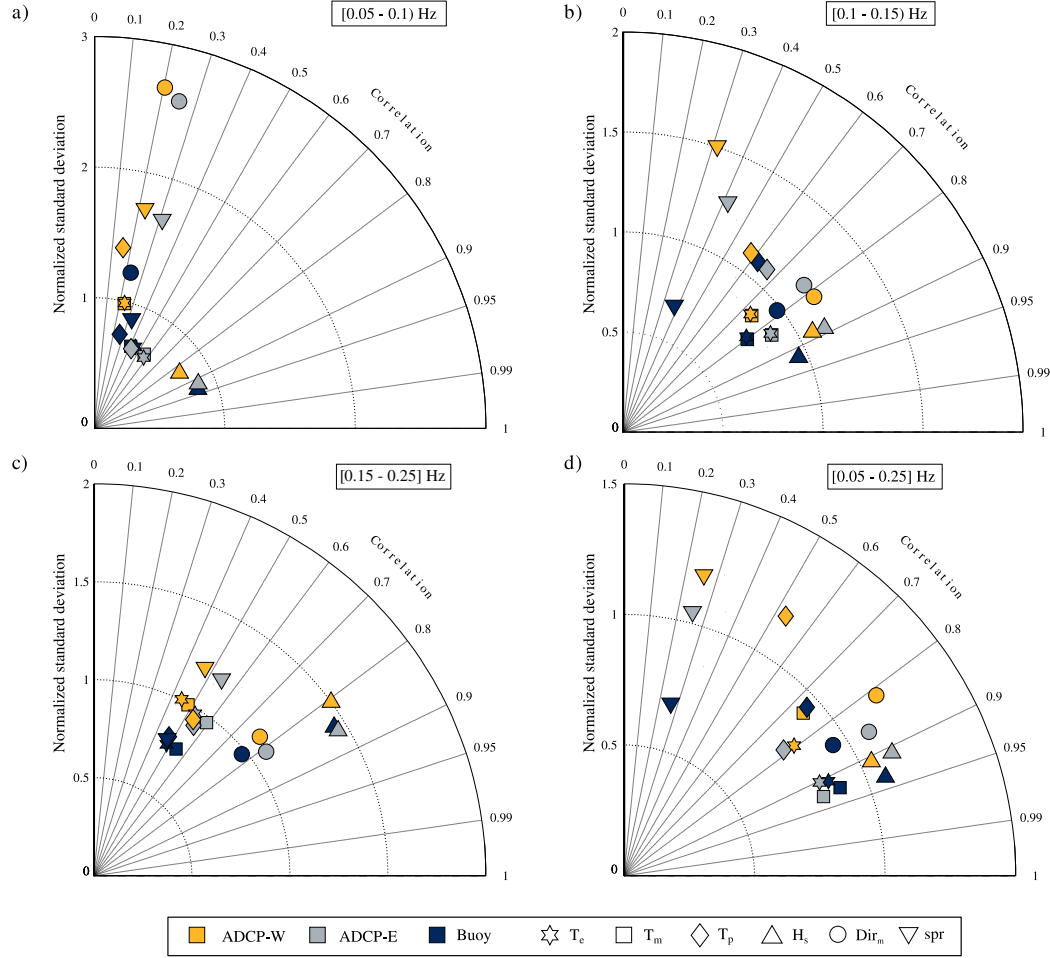
Figure 5.3: Taylor diagram showing the result of the comparison between radar- and in situ-measured wave parameters. Colours represent the three in situ devices, buoy (blue), ADCP-E (grey) and ADCP-W (yellow). The symbols denote the different wave parameters evaluated: energy period (T_e; star), mean period (T_m; square), peak period (T_p; diamond), significant wave height (H_s; triangle), mean wave direction (Dir_m; circle), directional wave spread (spr; inverted triangle). The symbols are placed in the diagram according to their NSTD (dotted arcs) and correlation coefficient (full lines). Results are shown for three frequency bands and the full range of available frequencies: a) 0.05 to 0.1 Hz, b) 0.1 to 0.15 Hz, c) 0.15 to 0.25 and d) 0.05 to 0.25 Hz.

Finally, peak period is the least correlated parameter to the in situ measurements. This is not a surprising result, given its high sampling variability. The results of the buoy and ADCP-E comparisons are similar, and show lower standard deviation than the in situ measurements at the lowest frequency band and correlations around 0.4. The agreement improves when comparing shorter swell and the bulk of the spectrum, both of which show similar results. Correlations in these cases are between 0.6 and 0.8, and radar standard deviations are equivalent to the wave buoy

and lower than the ADCP-E. The agreement between the methods for the short waves resulted in correlations between 0.5 and 0.6, standard deviations equivalent to the buoy and ADCP-E and lower than ADCP-W. As with the other parameters, the radar estimate at the ADCP-W site shows the poorest agreement to the in situ measurements at the lower frequency bands, while the results for the short waves are very close to those obtained at the other two sites.

The agreement on the mean wave directions estimated by the radar and the in situ devices is generally very satisfactory, and as already observed for the other parameters, the poorest performance is found at the low frequency band. Directional measurements at these low frequencies are usually related to low levels of energy and therefore low signal-to-noise ratios. Consequently, is not uncommon to find inconsistencies between measuring platforms (i.e. Herbers and Lentz, 2009; Work, 2008), which might be contributing to the differences found. Above 0.1 Hz correlations increase to 0.8, and while the wave buoy and the radar show similar standard deviations, the ADCP distributions seem to be more tightly grouped.

The other directional parameter presented in Figure 5.3, the directional spread, shows the best performance at the highest frequency band for all three locations, while the correlations of the spread of longer waves and the bulk of the spectrum are all below 0.5. Worth mentioning is the considerable difference between the standard deviation of the radar measurements when compared to the wave buoy and the ADCPs, which indicate the radar estimates have higher standard deviation than the ADCPs, but are lower than the wave buoy. The directional spreading is a variable that hardly ever compares well between platforms, which again might be all contributing to the differences found. Whether the different behaviour of the spreading at the ADCP sites and the buoy is due to differences in the radar or the in situ estimates will be discussed later in the text.
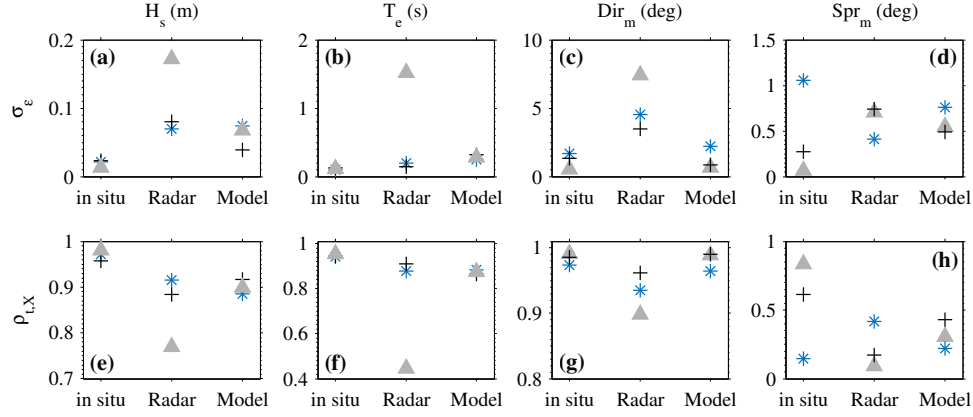
Figure 5.4: (First row): Triple collocation estimates of the error variances of the (a) H_s, (b) T_e, (c) Dir_m and (d) Spr_m estimates for the radar and in situ measurements, and the model products. (Second row): Extended triple collocation estimates of the correlation coefficient between the unknown truth and the radar, in situ, and model products of (e) H_s, (f) T_e and (g) Dir_m and (h) Spr_m. The results were calculated at the locations of the in situ devices: buoy (blue asterisk), ADCP-E (black cross) and ADCP-W (grey triangle).

Having hypothesised that the differences in directional parameters may be in fact derived from errors in the in situ measurements as well as in the radar, it seems appropriate to analyse the results using the ETC method introduced in Chapter 3. The results are shown in Figure 5.4, and provide clear evidence of the noise in the radar measurements acquired at the position of the ADCP-W, which present the highest error variances for all three parameters evaluated. At the other two locations, the radar's error variances are closer to those obtained for the modelled H_s (Figure 5.4a), especially at the wave buoy location. For T_e (Figure 5.4b), the highest error variances are associated to the wave model. The results of the latter are generally smother than those obtained with the radar and the in situ devices, hence the model seems to be penalised for not resolving the same details than the other two measuring systems. This is not the case when studying wave direction, for which the random error of the radar estimates becomes more important than the smoothness of the model. High error variances are observed for the radar directional spread, which according to the ETC is barely correlated to the unknown truth. Similarly, the wave model and the wave buoy present large random errors

and low correlations. The ADCPs seem to have less noise affecting their measurements, which, opposite to the wave buoy, are well correlated to the underlying "true" value. These results seem to indicate that the lower standard deviations of the radar directional spreading in comparison to the wave buoy, might be in fact a result of large random errors affecting the surface following device.

5.3.2   Spatial comparisons

The same spatial analysis performed in the previous chapter was applied here to the results obtained with Seaview. The measurements of the in situ devices were compared in pairs, and the results are quantitatively reported as measures of the bias, RMSE, scatter index, and correlation between the two data sets. The same procedure was then carried out for radar measurements acquired at equivalent positions. As done when evaluating the semi-empirical algorithm, the discussion focuses on the buoy - ADCP-E pair, since comparisons involving measurements acquired at the ADCP-W site will be hindered by the noise that characterises the measurements at such location.

Table 5.1: Statistical indicators resulting from the comparison of radar-to-radar and in situ-to-in situ H_s, T_e, and D_m estimates. The first column indicates the sites used for comparison. (B-W) corresponds to the comparison between the buoy and the ADCP-W, (B-E) is the buoy and ADCP-E, and (E-W) corresponds to the two ADCPs, east and west. The results of the buoy - ADCP-E pair, referred to in the text, are shown in bold.

Pair	N	Param	Bias		RMSE		SI		R	
			In situ	Radar	In situ	Radar	In situ	Radar	In situ	Radar
B-W	1649	H_s	-0.07	-0.05	0.28	0.39	0.12	0.17	0.94	0.89
		T_e	-0.20	0.40	0.49	0.99	0.06	0.12	0.95	0.76
		D_m	-9	-0.1	14	21	0.05	0.08	0.95	0.91
B-E	**1900**	H_s	**-0.30**	**-0.2**	**0.24**	**0.38**	**0.10**	**0.16**	**0.94**	**0.89**
		T_e	**-0.40**	**-0.08**	**0.50**	**0.47**	**0.06**	**0.06**	**0.94**	**0.93**
		D_m	**-10**	**-8**	**13**	**23**	**0.05**	**0.09**	**0.95**	**0.90**
E-W	1649	H_s	0.30	0.10	0.25	0.44	0.13	0.20	0.95	0.85
		T_e	0.30	0.40	0.46	0.93	0.06	0.12	0.96	0.78
		D_m	3	9	6.8	23	0.03	0.09	0.98	0.90

The in situ devices exhibited highly correlated measurements between the wave buoy and ADCP-E for all three parameters evaluated (Table 5.1). The bias is negative, indicating smaller measured conditions at the ADCP-E, both in terms of H_s and T_e. As mentioned in the previous chapter, the modification of the wave field between these two locations is due to its interaction with the varying seabed and possibly the tidal flow. With the exception of the lower bias in the T_e retrieved at these two locations, the statistics resulting from the radar-to-radar comparison are very close to those obtained from the in situ measurements. In summary, the radar-to-radar comparisons of the buoy - ADCP-E pair revealed 30% more scatter (SI), and 30% less bias on the H_s results than the in situ comparisons. The T_e estimations derived from the radar are only 1% less correlated between the two locations than the in situ pair, and show the same SI, but unlike the latter do not show smaller T_e measured at the ADCP-E. Finally, the wave direction retrieved by the radar at these two sites is only 5% less correlated than the in situ devices and shows otherwise similar results to the latter.

In order to provide a general overview of the accuracy of the spatial measurements, these were also compared to the results of the wave model. The agreement between the two methods (Figure 5.5) is quantified in terms of the correlation coefficient, which resulted in values above 0.8 over most of the radar's coverage, and for all three parameters examined, excluding the directional spread. The errors are not distributed evenly across the radar coverage, and as observed when examining the results obtained at the ADCP-W site, the south eastern part of the grid shows the greatest disagreement between radar and wave model. Correlation of both wave height and period decreases to values around 0.5 and 0.6 over this area, which seems to be affected by the same spurious low energy frequency seen at the ADCP-W comparisons. Although following the same pattern as H_s and T_e, the correlation reduction in mean direction is less pronounced, and stays above 0.7 at all points analysed. Finally, the directional spread shows a poor agreement

between methods, with the best results localized in a strip on the northern part of the coverage area.
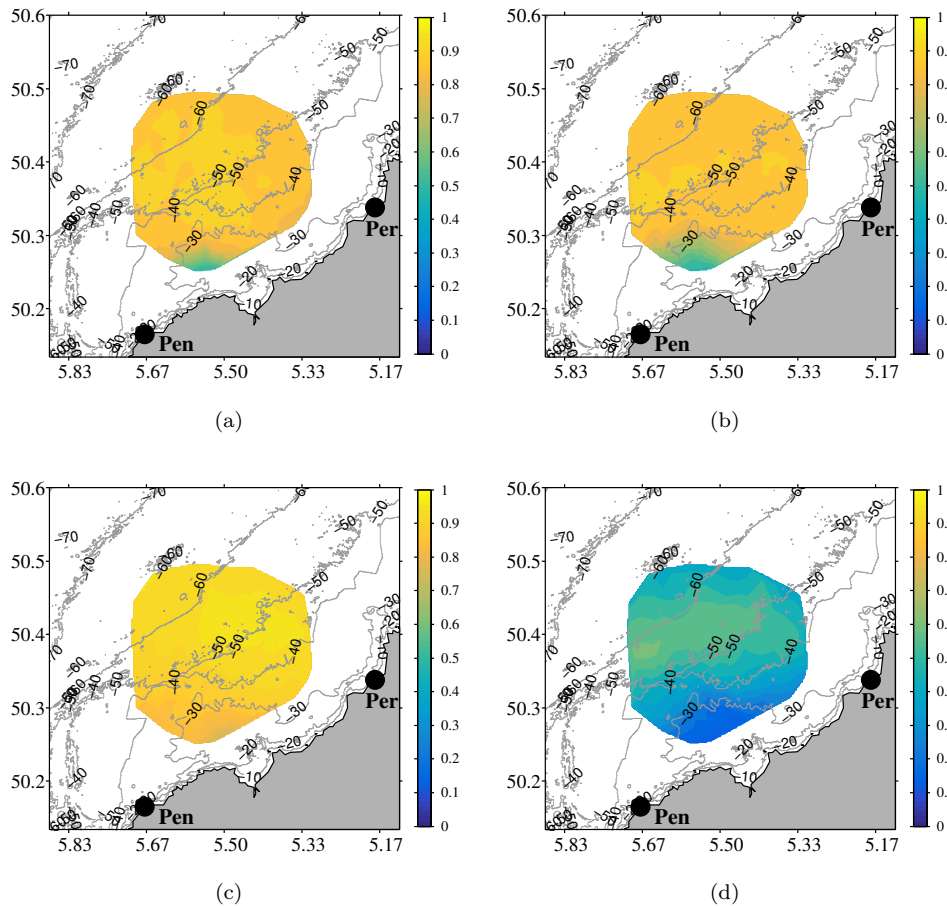
Figure 5.5: Linear correlation coefficient between radar and model estimates of (a) Significant wave height, (b) Energy period, (c) Mean wave direction and (d) directional spread. Model and radar grid points closer than 500 m were used for the computations.

5.3.3   Frequency dependent parameters

The first row of Figure 5.6 shows the differences in spectral energy between radar and in situ devices, as calculated with Equation 5.4. The results are very similar at the three locations examined, with the highest discrepancies appearing at the low frequencies and for the smallest waves. As mentioned before, the signal to noise ratio for any wave measuring device is low in these conditions, and the sampling variability will be high, making the intercomparisons difficult.

In the particular case of the wave buoy, restoring forces acting on the mooring, and interactions with local tidal streams near the surface, introduce an even higher degree of uncertainty in the measurements (Bouferrouk et al., 2016). Radar energy overestimations at these low frequencies have also been found, and attributed to antenna sidelobes and current variability (Wyatt et al., 1999). This would be a feasible explanation for the discrepancies found for the ADCP-W comparisons, which as seen in the previous section are affected by this issue; however, we do not expect this to a be a problem at the other two sites, located at lower angles from the boresight of the radar stations. The latter, and the fact that these low amplitude waves are also overestimated at the rest of the frequency bins, seems to indicate that there might also be a systematic error probably derived from the radar technique, which has a lower measuring limit of 0.4 m waves at the frequency used by our radars. It is also on these low frequency bins, up to 0.06 Hz, where the standard deviation of the differences between the in situ and radar estimates (not shown) are the highest. As mentioned above, this might be a result of the high sampling uncertainty for small long period waves.

On the other hand, the energy at the peak of the spectrum is underestimated by the radar. This is in agreement with the results found in Wyatt et al. (1999), where it was suggested that the underestimations might be linked to the poorer resolution in the radar measurements, which is in turn associated with the averaging that takes part in the inversion. The recurrence of this situation is further demonstrated by using the methods presented in Dabbi et al. (2015) and introduced in the previous section. Using these metrics confirmed that more than 50% of the spectra obtained at the three locations examined are broader and have lower peak energy than the in situ devices. In addition to the lower energy, the position of the peak is generally shifted to higher frequencies, resulting in a shorter peak wave period. At the ADCP-W, the cases when the peak energy is higher and located at a lower frequency become important with respect to the other two locations. This is in

agreement with the assumption of spurious peaks appearing at the low frequencies as a consequence of sidelobes and current variability.
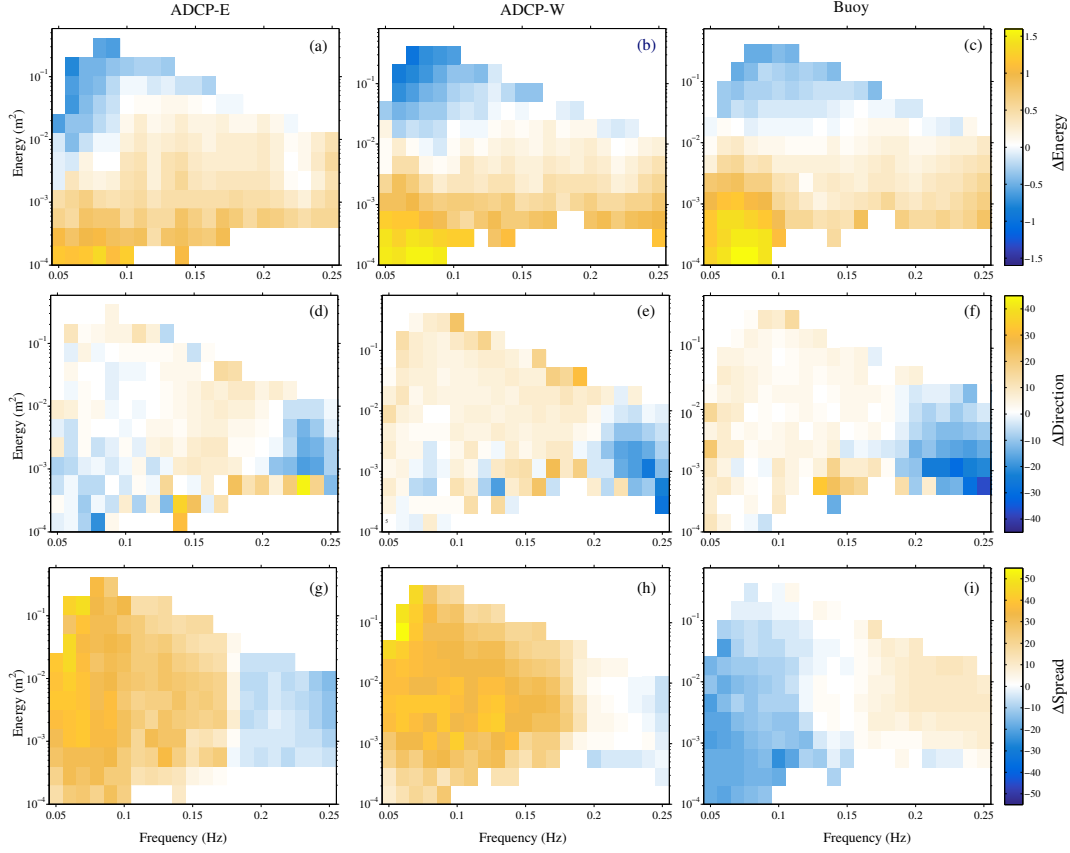
Figure 5.6: Differences between radar and in situ measurements, calculated for different frequency/energy bins. Orange/yellow colours suggest that the radar is higher than the in situ value, and blue indicates the opposite. Each column corresponds to a different location: Left (a, d, g): ADCP-E, Middle (b, e, h): ADCP-W, Right (c, f, i): Buoy. The three rows are: Top: differences in energy, Middle: differences in mean direction, Bottom: differences in directional spread.

The differences in mean direction shown in Figure 5.6 are low at most energy-frequency bins. The radar directions are approximately 10° lower than the in situ measurements at the high frequencies and slightly higher at the low frequencies. The standard deviation of the differences (not shown) shows the same pattern as the errors, with the highest values matching the bins where the highest differences between radar and in situ measurements were found.

The directional spread shows almost identical results for the two ADCPs and the opposite at the wave buoy. Compared to the ADCPs, the radar spread is

an average 20° higher than the in situ measurements for the frequency band up to 0.18 Hz, and only 5° lower at the upper frequency band. Compared to the buoy, the underestimates are localized around the frequencies up to 0.1 Hz and reach maximum values of 10°, while overestimates appear at the high frequencies, but stay as low as about 5° degrees on average. The standard deviation of the differences between the buoy and the radar is also lower than that resulting from the ADCP-radar comparisons. Among the latter, the highest standard deviations are observed at the lower energy-frequency bins of the ADCP-W comparison, but this again might be a result of the noise in the radar measurements.
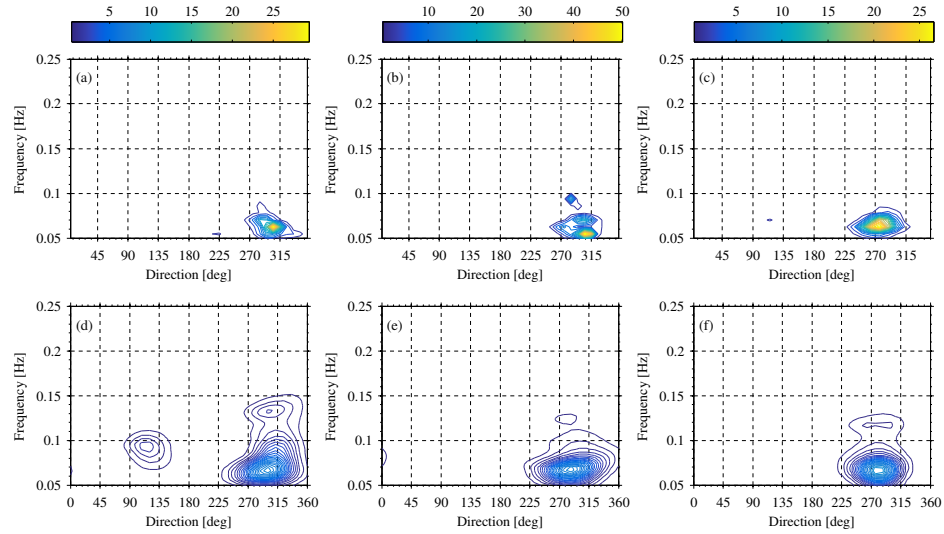
Figure 5.7: Radar and in situ estimates of wave directional spectra on 21 October 2012 at 1000 UTC. The upper panel shows the results obtained from the in situ measurements, and the bottom panel are the radar estimates. ADCP-E spectrum (a, d). ADCP-W spectrum (b, e). Wave buoy (c, f). The colorbar represents the directional energy density (m²/Hz/deg).

5.3.4   Directional spectra

In the three cases analysed here, the radar spectrum is broader than that inferred from the in situ devices, the energy is spread over the frequencies and there is less energy at the peak, which is underestimated. Wyatt et al. (1999) also found this behavior, which they attributed to lower spectral resolution in the radar estimates.

The longest swell recorded over the period analysed here arrived to the study area on the first hours of 21 October. At 1000 UTC, a moderate wind was blowing from the east at 7 m s^{-1} and the wave field was dominated by this long period system, whose peak direction was determined to be about 280 $\pm$ 10° by both radar and in situ devices. At the ADCP-E site (Figures 5.7a and 5.7d), the radar detected a secondary mode close to 0.1 Hz and 120° which is not observed by the in situ device. The same system had been observed by the radar at the other two locations the previous two hours, and there is some energy on the buoy spectrum around the same direction, which seems to indicate that is not an error on the radar estimate. The radar's peak frequency differs in 0.01 Hz from those of the in situ devices.
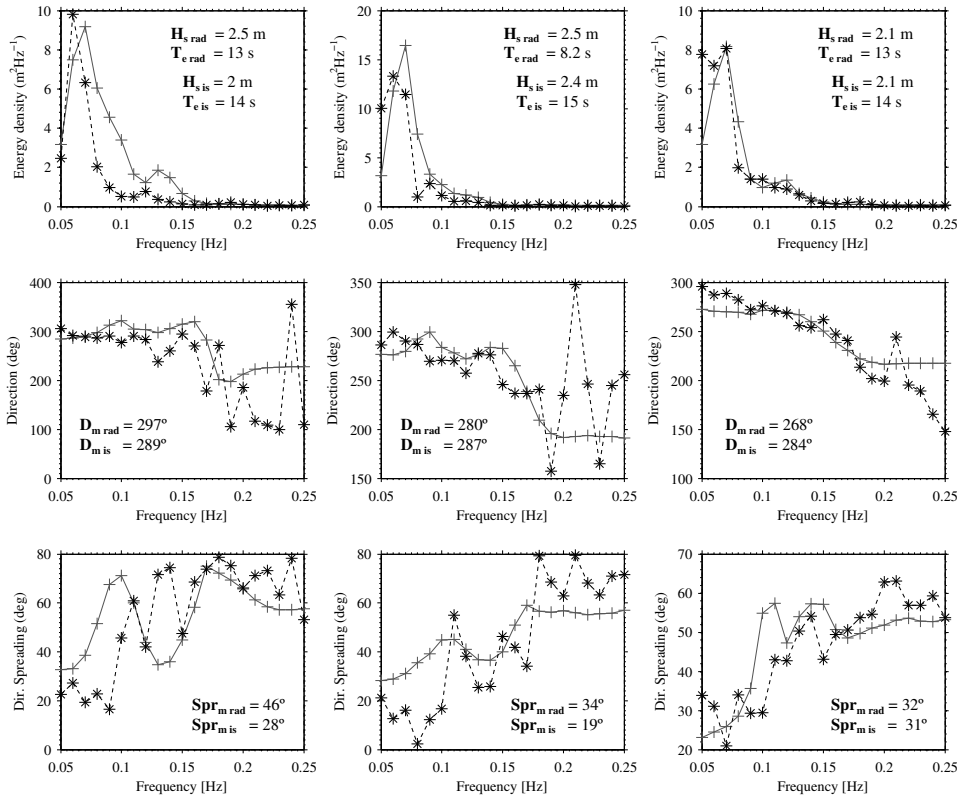
Figure 5.8: Radar and in situ estimates of one-dimensional spectra, mean direction and directional spreading as a function of frequency on 21 October 2012 at 1000 UTC. Panel a) ADCP-E (dashed black line and *) and radar (gray line and +). Panel b) ADCP-W (dashed black line and *) and radar (gray line and +). Panel c) Buoy (dashed black line and *) and radar (gray line and +). The bulk parameters derived from the spectra are shown for the radar (X_{rad}) and the in situ devices (X_{is}).

Figure 5.8 shows the integrated one-dimensional representations of spectral energy, direction and spread. The spectra match very well across the three sites. The biggest disagreement is on the ADCP-E comparison, with the radar estimate being much broader than the in situ measurement. The directional spread measured by both techniques shows what was seen on the previous section, radar measurements higher than the ADCP's over the low frequencies and sightly lower at the higher frequency end. The opposite is observed at the buoy.
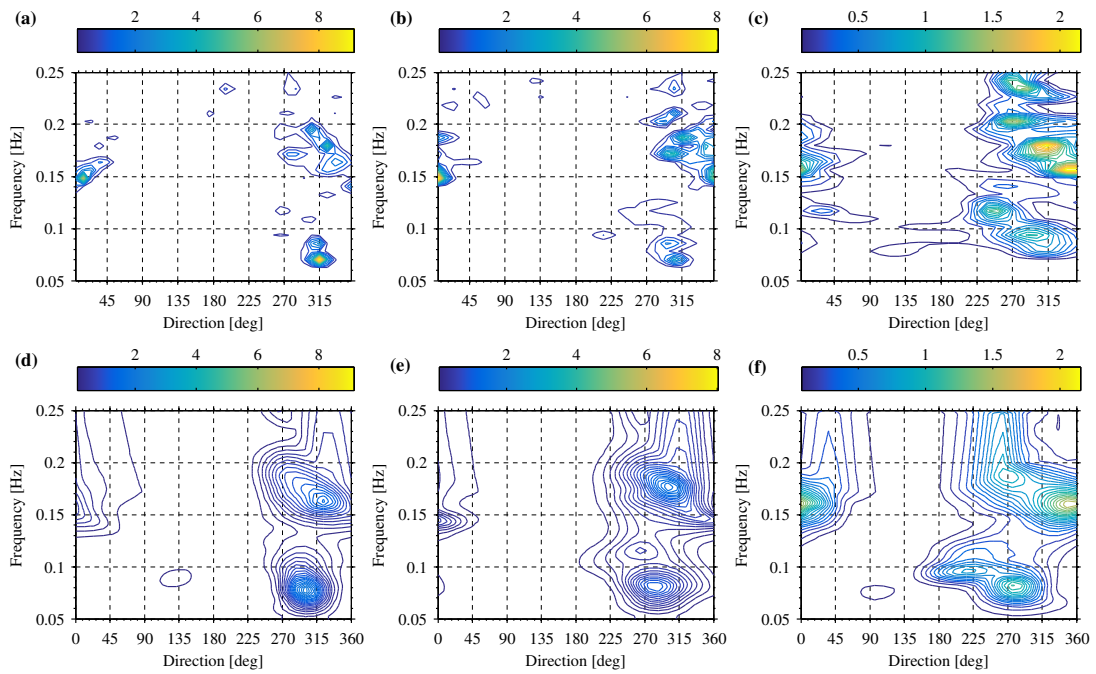
Figure 5.9: Radar and in situ estimates of wave directional spectra on 24 September 2012 at 1100 UTC. The upper panel shows the results obtained from the in situ measurements, and the bottom panel are the radar estimates. ADCP-E spectrum (a, d). ADCP-W spectrum (b, e). Wave buoy (c, f). The colorbar represents the directional energy density (m^2/Hz/deg).

On 24 September at 1100 UTC, the wave field was formed by a low frequency system and a wind sea both very close in direction (Figure 5.9). On the afternoon of the day before, the wind speed had grown very rapidly from 5 to 11 m s^{-1} while turning north from a more easterly direction. At the time of the observations described here the wind had been steadily blowing for about 14 hours and had a westerly direction. The radar-derived two dimensional spectra show broader distributions than the in situ spectra. The differences are higher when compared

to the ADCP spectra, which are sharper than the buoy, possibly because the greater number of degrees of freedom in the measurements (Strong et al., 2000).
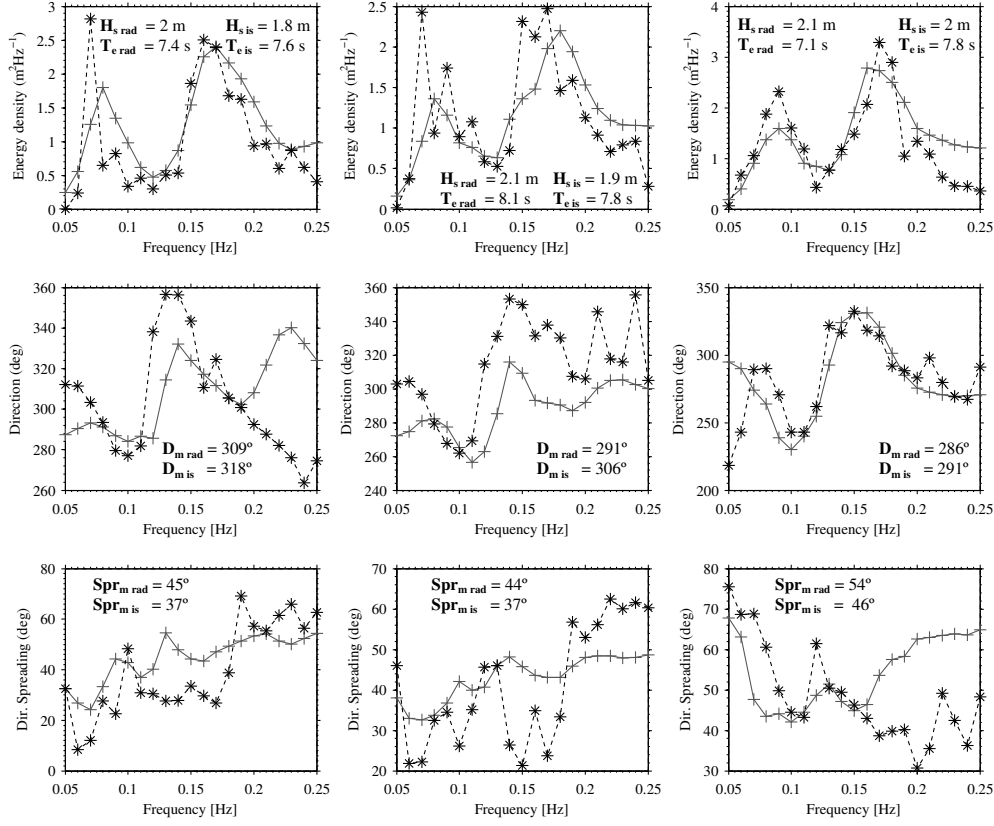
Figure 5.10: Radar and in situ estimates of one-dimensional spectra, mean direction and directional spreading as a function of frequency on 24 September 2012 at 1100 UTC. Panel a) ADCP-E (dashed black line and *) and radar (grey line and +). Panel b) ADCP-W (dashed black line and *) and radar (grey line and +). Panel c) Buoy (dashed black line and *) and radar (grey line and +). The bulk parameters derived from the spectra are shown for the radar (X_{rad}) and the in situ devices (X_{is}).

The low frequency system measured by the radar at the buoy site exhibits two modes propagating from 220° and 280°, and very close in frequency. Although the same is reported by the in situ device, the direction of arrival is about 10° further north and at slightly higher frequencies. Looking at the spectral directions (Figure 5.10), we can see, both in situ and radar estimates follow the same trends, but the radar estimates are lower. Results of the wave directional spreading show the general observations given in Figure 5.8, with higher spreading on the low frequencies of the radar estimates as compared to the ADCPs, and lower above 0.19 Hz. Again, as seen in Figure 5.8, this is reversed on the buoy comparison,

where the radar spread is lower at the low frequency and higher above 0.16 Hz. The agreement on wave parameters derived from these spectra is very good, and the shape of these is also very similar in the in situ and radar derived estimates.

On the 26 October at 0100 UTC, the directional spectra measured at the buoy and ADCP-W sites is formed by a weak south-westerly swell and a north easterly wind sea (Figure 5.11). The latter is also observed at the ADCP-E, but there is no evidence of the low frequency system on the radar estimate and very little energy appears at about 0.09 Hz on the in situ spectrum. The swell measured by the radar
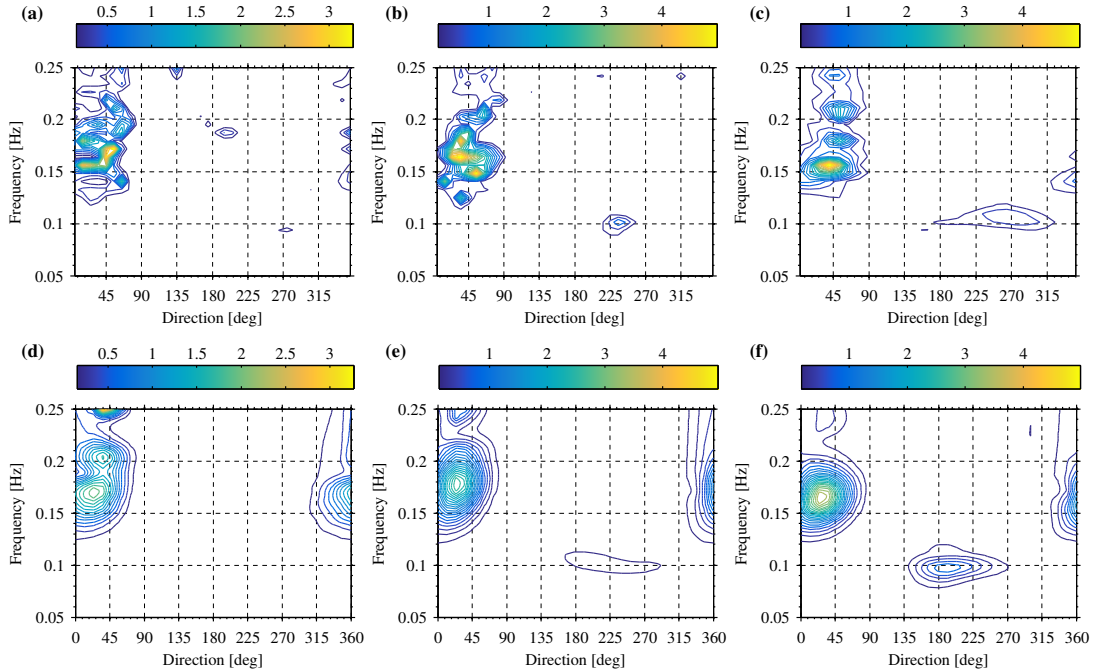
Figure 5.11: Radar and in situ estimates of wave directional spectra on 26 October 2012 at 0100 UTC. The upper panel shows the results obtained from the in situ measurements, and the bottom panel are the radar estimates. ADCP-E spectrum (a, d). ADCP-W spectrum (b, e). Wave buoy (c, f). The colour bar represents the directional energy density (m^2/Hz/deg).

at the ADCP-W location is more spread in direction than the in situ measurement, and displaced toward the south with respect to the wave buoy. The direction of the high frequency system compares well at all locations and the different measuring techniques, but the contours are broader in the radar estimates. There are three modes on the radar measurement at the ADCP-E site, which are slightly stronger

than the in situ measurement and result in a higher wave height. The direction of the spectral components above 0.13 Hz agree well, with differences up to 20°. The same can be observed at the low frequencies and the greater disagreement is found between 0.1 and 0.13 Hz. The directional spread estimated by the radar follows the same pattern as the in situ measurements, showing a better agreement to the buoy measurement and higher values than the ADCPs up to 0.2 Hz.
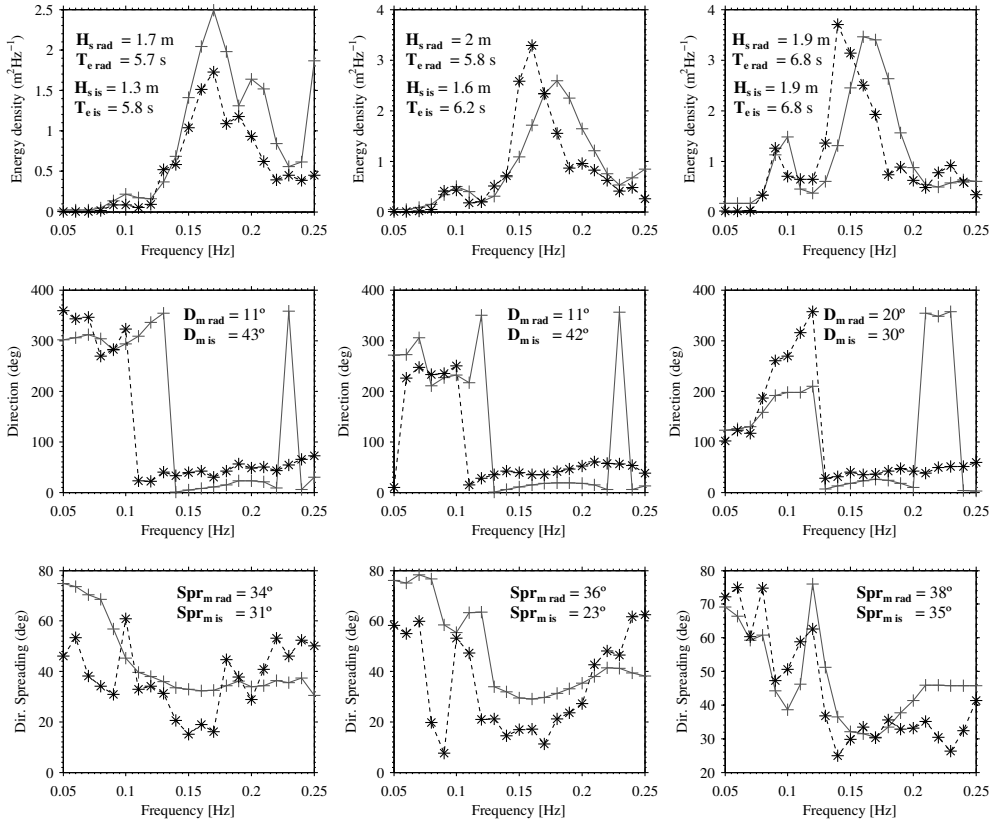
Figure 5.12: Radar and in situ estimates of one-dimensional spectra, mean direction and directional spreading as a function of frequency on 26 October 2012 at 1100 UTC. Panel a) ADCP-E (dashed black line and *) and radar (grey line and +). Panel b) ADCP-W (dashed black line and *) and radar (grey line and +). Panel c) Buoy (dashed black line and *) and radar (grey line and +). The bulk parameters derived from the spectra are shown for the radar (X_{rad}) and the in situ devices (X_{is}).

5.4   Discussion

One of the main causes of the differences between radar and in situ wave spectra is the lower spectral resolution of the former, which generally results in broader

spectra. In terms of parameter estimation, this is generally translated in an underestimation of wave periods. However, the broad radar spectra usually have a slightly lower energy content at the peak of the spectrum. Combined, these two peculiarities result in an overall spectral energy content equivalent to the in situ measurements, and consequently, significant wave height is accurately estimated by the radar.

The inversion algorithm has shown a high skill estimating mean wave direction, which is highly correlated to the in situ measurements at all the frequency bands studied, with the only exception of the low end of the spectrum. Differences between devices in this frequency band, where energy levels and signal-to-noise ratios are usually low, are not uncommon (Work, 2008), therefore part of the discrepancies might be introduced by the different methods. For example, the Fourier coefficients obtained with four buoys deployed in a nearby location, and identical to the one used for this study, have been reported to have a greater variability and less accuracy at frequencies below 0.07 Hz (Saulnier et al., 2011).

The radar's directional spread showed a negative bias below 0.16 Hz when compared against the wave buoy measurements. The opposite outcome arose from the analysis against the measurements acquired by both ADCPs. These results were reversed on the high frequencies, where the radar spread was lower than wave buoy, and higher than the ADCP estimate. Measuring directional spread is not an easy task, and all three devices involved in the intercomparison have been reported to produce biased estimates for different reasons. HF radar directional spread has been found to be biased high owing to the resolution of the directional spectra (Wyatt et al., 2003), pitch-roll buoys have been reported to produce inaccurate measures of directional spread when low levels of noise appear in the surface elevation signal (Kuik et al., 1988), and low signal-to-noise ratios in ADCP velocity estimates at low frequencies were found to bias the directional spread results (Herbers and Lentz, 2009).

Our TC error estimates pointed to the buoy spread as having the largest random error, and the lowest correlation to underlying true value. However, the measurements seem to be within the limits of those presented in Saulnier et al. (2011), which were acquired with the same device and in close proximity to our measurements. It is therefore not clear whether the contrasting behaviour observed was caused by differences in the radar or the in situ measurements between the sites; hence additional discussion of these observations is provided below.

The first disparity between the in situ measurements is evidenced by Figure 5.2, where it can be seen that the wave buoy spread is considerably higher than the estimates retrieved by the two ADCPs. Another distinctive feature, although not evident in Figure 5.2, is a stronger tidal modulation of the buoy measurements, which oscillate up to 20° in 6-h cycles. This is in fact believed to be, at least in part, responsible for the differing results found, and examination of the autocorrelation function of the difference between the wave buoy and the ADCPs should provide further insight on to whether the differing measures of spread obtained with the wave buoy and the ADCPs are due to tidal effects. The results obtained using data from the wave buoy and the ADCP-E are plotted in Figure 5.13a, together with the autocorrelation of the differences between the radar spread at equivalent positions (Figure 5.13b). The residuals obtained from the in situ measurements show a clear tidal signal, with peaks in correlation every six hours, which is not observed when comparing the radar's spread measured at the same locations. Using the ADCP-W measurements produced the same outcome (not shown). These results indicate that the differences between the in situ devices at these two locations are in fact caused by a differential effect of the tidal current on the measurements.

Six-hour modulation cycles in mean directional spreading were also reported in Saulnier et al. (2011), where they observed a correlation between wave spread and current intensity, characterised by minimum values during slack water, which then increased during the flood and ebb phases of the tide. According to this
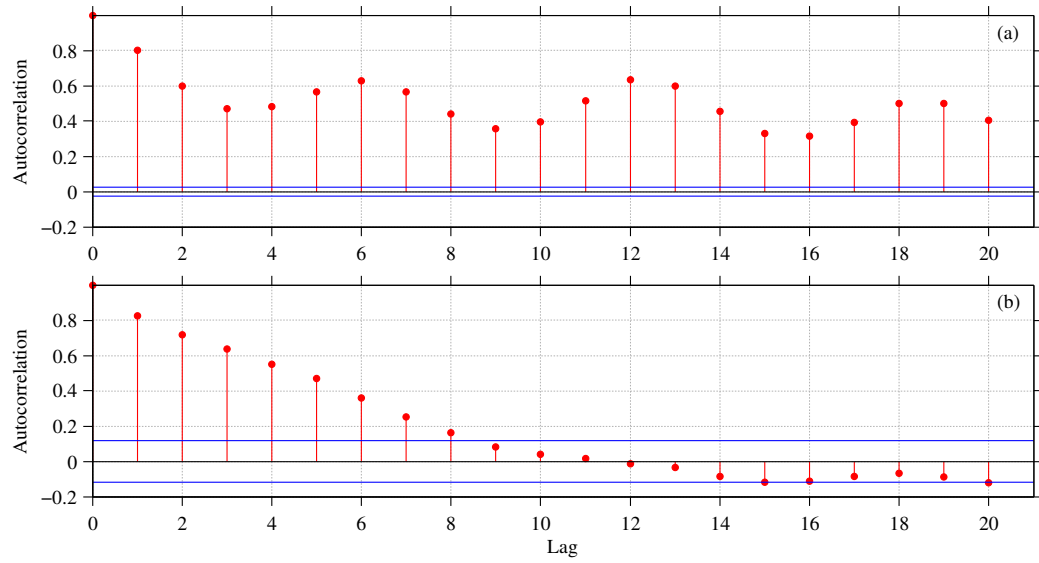
Figure 5.13: Autocorrelation function of the time series of the differences between directional spread measured at two locations. (a) Autocorrelation of differences between the wave buoy and the ADCP-E spread. (b) Autocorrelation of the differences between the radar spread estimates obtained at the buoy and ADCP-E sites. The confidence bounds are shown in blue.

observation, the lower modulation of the spread measured by the ADCP-E could be related to the weaker currents (see Chapter 7) for details on the current field) affecting the area where it was deployed. However, the differences in current intensity between the wave buoy location and the ADCP-W, are probably not enough to explain the strong dissimilarity in the spread values, which might, however, be explained by the location of the devices. The ADCPs were deployed closer to shore, at sites were the water column was about 20 m shallower, hence the effects of refraction in reducing directional spread might be responsible for the lower values measured by these devices. In addition, and as evidenced in section 5.3.4, the ADCP spectra have higher resolution than the buoy, and this might result in lower spread measured by the optical devices (Work, 2008).

After the above analysis is still not clear whether the location of the devices, and therefore the differential effect of the tide, is responsible for the differences observed, or if part of the disagreement is derived from how the instruments themselves respond to the tidal current. Therefore, we can conclude that while further

investigation is required to determine the reason for the differences found, the results presented here show the value of the HF radar spatial data in identifying inconsistencies such as those observed.

5.5   Conclusions

Overall, the inversion algorithm has shown to be capable of providing accurate estimates of directional spectra, and at present the main drawback of the method is the data return, which did not exceed 55% over the 8-month period studied here. Increasing this rate through improvement of the SNR, noise cancelling techniques, and a dedicated maintenance of the radars are possibly the essential requirements to enable the use of HF radar wave spectra at operational level. Nevertheless, the HF radar technique, with its well documented ability to provide accurate measurements of surface currents and the high quality of the directional spectra presented here, has proven it could be of considerable value to any project that requires spatial measurements.

Chapter 6

Comparison between inversion algorithms

6.1   Introduction

One of the research objectives set out in Chapter 1 sought to determine the errors associated to two different wave inversion algorithms. To that aim, several analyses were conducted and presented throughout the two previous chapters, paying special attention into any observed inaccuracies and their driving mechanisms. However, it is difficult to relate and compare the statistical results obtained, since they were derived from slightly different populations. It is, therefore, the aim of this chapter to compare the two approaches using a unified framework, in which only records common to the two methods are evaluated.

The relative accuracy of the two wave inversion algorithms was evaluated in Gomez et al. (2015), using measurements acquired with the same radars that provide the data for this research. The results indicated a slightly better performance of the semi-empirical method in evaluating H_s, which had a RMSE 12% lower than that retrieved by Seaview. On the other hand, the numerical inversion showed

a superior skill in estimating T_e and D_m, which had respectively 68% and 35% less error than the semi-empirical retrievals of these two parameters. However, while this work will evaluate the full version of the Seaview software, the latter comparisons were based on the results of a reduced version of such software.

6.2   Materials and methods

In order to avoid including the data used to calibrate the semi-empirical algorithm in Chapter 4, the analyses to follow are based on the remaining 5-month period used for validation in that same chapter. Within the 5-month period, only estimates obtained during dual-radar operation are selected for further examination.

The methods used in this chapter are shared with the previous one, and their detailed description can be found there, as well as in Chapter 3. Common error metrics are used to evaluate the agreement between radar- and in situ-measured wave parameters, and the results are graphically represented in a Taylor diagram (Taylor, 2001). The computed statistics are complemented by an investigation of the random errors associated to each of the data sets used for comparison. Such analysis is based on the triple collocation technique reviewed in Chapter 3.

6.3   Results

6.3.1   Comparison of data return rates

The first difference between the two inversion methods lies in their distinct capability of producing results over time and space, and these are compared here. One the main reasons of differing data return rates between the two approaches, is their SN requirements. While the semi-empirical method presented in Chapter 4

requires a second-order Doppler spectrum with a SNR higher than 10 dB in order to perform the wave inversion, this number must be above 15 dB for Seaview's numerical inversion to be executed. This is probably responsible for the average 20% difference in temporal data return achieved by two methods throughout the 8 months analysed in this work (Figure 6.1b).
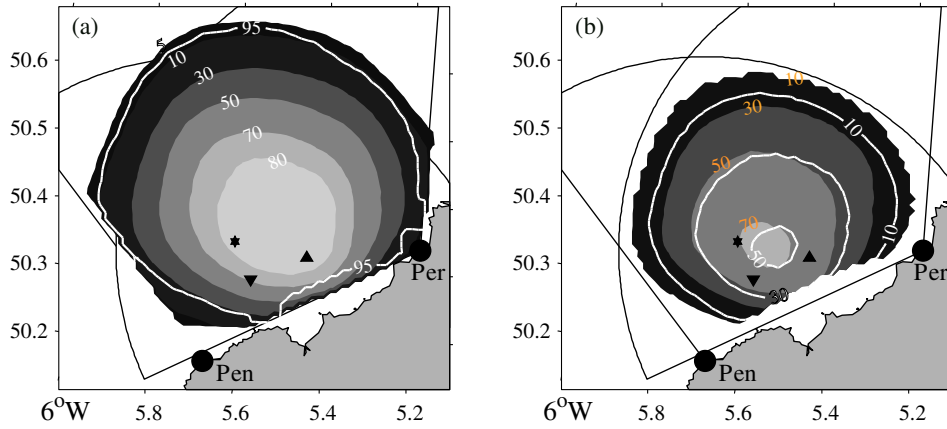
Figure 6.1: Temporal data coverage shown as a percentage of the time each cell within the radars wave coverage had inverted data over an 8-month period. The filled contours in (a) show the WERA's algorithm total percentage of data return. Both directional information derived from the two radars, and non-directional results obtained with only one station were accounted for. The white contour line demarcates the area where surface currents were acquired over 95% of the time. The filled contours and orange numbers in (b) show the percentage of directional results obtained with the WERA algorithm when both stations acquired good quality data simultaneously, and the white contours demarcate the areas where Seaview wave spectra were available over 10% and 50% of the time. Radar stations (black circles), their wave coverage (fans) and in situ mooring devices are also depicted: wave buoy (star), ADCP-W (inverted triangle) and ADCP-E (triangle).

The percentage of data return increases considerably when non-directional results obtained with only one station are accounted for. Although Seaview produces single-site estimates, these were not analysed here, and the percentage of combined data return was obtained using WERA's retrievals. The results reveal that 1D spectra can be obtained over 80% of the time, in an area of about 20-by-20 km in the centre of the radar's field of view (Figure 6.1a). However, as seen in Chapter 4, the increase in data return comes at the expense of data quality. Single-radar estimates are more sensitive to factors such as wind direction, current speed, or

the sea-state; hence the results are prone to be affected by a greater number of outliers. Nonetheless, RMSE errors in significant wave height and energy period, were only found to increase an 11% in average when both single- and dual-radar estimates were compared to in situ measurements at three different locations. Such a number is far from disappointing, and indicates that these two parameters can be measured with a rate of success of 80%, and RMSE errors below 0.4 m and 0.9 s in wave height and energy period, respectively.

6.3.2   Comparison of integrated parameters

Figure 6.2 shows the results of comparing wave parameters obtained with both algorithms against those measured by the three in situ devices deployed in the area. Calculations were performed for three frequency bands (Figures 6.2a to 6.2c) and for the full range of available frequencies (Figure 6.2d). The correlation between radar and in situ measurements is shown on the full lines, and the dotted arcs correspond to the standard deviation of the radar estimates normalized by the in situ value.

The wave heights retrieved by both schemes are very similar to each other, and in good agreement with the in situ measurements at all the frequency bands examined. Seaview performs marginally better when comparing the energy containing waves (Figure 6.2b), as well as the estimates obtained at the buoy and ADCP-E sites for the lowest frequency band. Although still well correlated, the wave heights estimated by Seaview at the highest frequency band (Figure 6.2c), seem to be nosier than the in situ measurements, which have a standard deviation 1.5 times lower than the radar wave heights. This is not the case of the wave heights obtained with WERA, which although slightly less correlated to the in situ values, show standard deviations very close to them. The most favourable statistics are obtained when evaluating the bulk of the spectrum, which resulted in wave height

correlations higher than 0.9 for all devices and the two methods, and standard deviations very close to those measured by the in situ devices.
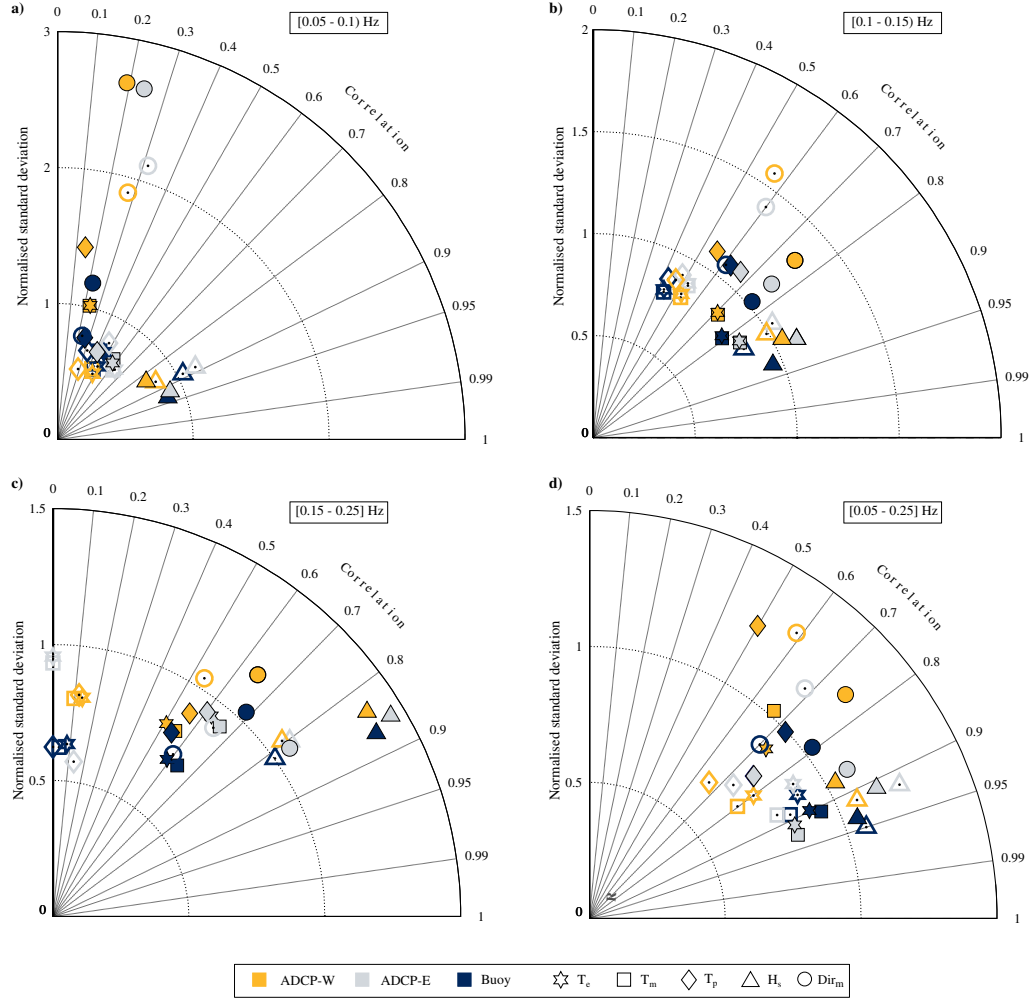
Figure 6.2: Taylor diagram depicting the results from the comparison between radar- and in situ-measured wave parameters. Colours represent the three in situ devices, buoy (blue), ADCP-E (grey) and ADCP-W (yellow). The symbols denote the wave parameters evaluated: energy period (T_e; star), mean period (T_m; square), peak period (T_p; diamond), significant wave height (H_s; triangle), and mean wave direction (Dir_m; circle). Empty and full symbols correspond to the results obtained with the WERA and Seaview algorithms, respectively. The symbols are placed in the diagram according to their NSTD (dotted arcs), and correlation coefficient (full lines). Results are shown for three frequency bands and the full range of available frequencies: a) 0.05 to 0.1 Hz, b) 0.1 to 0.15 Hz, c) 0.15 to 0.25 and d) 0.05 to 0.25 Hz.

The estimates of energy and mean periods show more differences between the two schemes, with improved results obtained using Seaview. At the lowest frequency band, both methods show a poor performance when compared to the in situ values. Away from the low frequencies, the numerical inversion performs better than the

semi-empirical approach, especially in the band 0.1 - 0.15 Hz, where the correlations between the radar-retrieved wave period and that of the buoy and ADCP-E are above 0.8. On the other hand, WERA produced period estimates, which resulted in correlation coefficients of about 0.4 when compared against the in situ devices. The accuracy decreases for the short periods, which Seaview estimates with correlations ranging between 0.5 and 0.6, and lower variability than the in situ measurements. The wave periods retrieved by WERA in this frequency band are uncorrelated to the in situ measurements.

With the exception of the lowest frequency band, the mean wave directions estimated by Seaview are well correlated to the in situ measurements, with coefficients between 0.7 and 0.8, and standard deviations increasing from the buoy to the ADCP-W, as it was discussed in the previous chapter. Correlation decreases to about 0.6 - 0.7 when evaluating WERA directions.

In addition to the descriptive statistics presented in Figure 6.2, the variance of the errors associated to the results of each algorithm was evaluated using triple collocation. The results are presented in Figure 6.3 and indicate similar error variances associated to the two approaches. One of the main differences is the significantly higher variance of the Seaview estimates of H_s and T_e errors at the ADCP-W site. The source of the larger errors at this location has been discussed before, and attributed to the effects of antenna sidelobes and current variability; however, these results show that part of the error variance is also algorithm-specific. This is probably related to the way the two approaches delineate and separate the first- and second-order parts of the Doppler spectrum, which in the case of the WERA algorithm seems to be more effective in separating the spurious features from the second-order Doppler structure than Seaview. The variance of the H_s error obtained with the WERA algorithm at the other two sites is also slightly smaller than that resulting from the Seaview estimates. The situation reverses when examining the error variances of the T_e and D_m estimates, which are both lower for

the Seaview results. While the difference is minimal for the period results, the WERA mean wave directions are clearly noisier than those estimated by Seaview.
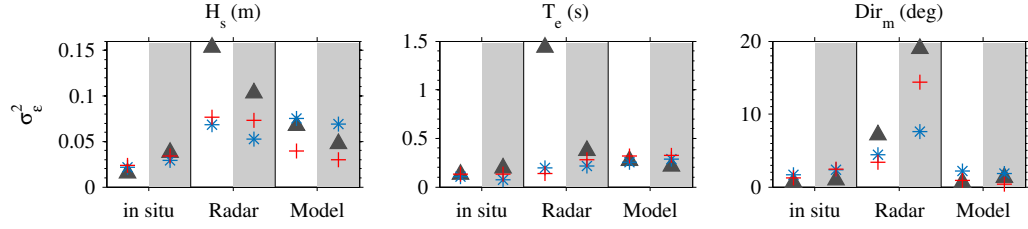
Figure 6.3: Triple collocation estimates of the error variances of (left) H_s, (middle) T_e, and (right) Dir_m. The white columns show the results of the triple collocation between in situ, Seaview, and model parameters, while the grey shaded columns show the results obtained with the in situ, WERA, and model parameters. The analysis was performed at the locations of the in situ devices: buoy (blue asterisk), ADCP-E (red cross) and ADCP-W (grey triangle).

A further step on the error analysis consisted on dividing the data into subsets according to different values of wave height, current velocity, and wind direction, with the aim of investigating how different environmental factors affect the radar measurements. The results are presented in Figure 6.4, and show the error variances associated to wave heights lower and higher than 3 m (Figure 6.4a); current speeds lower and higher than 0.5 ms^{-1} (Figure 6.4b), and wind directions from western and eastern sectors (Figure 6.4c). Evidencing the prevalence of wave heights smaller than 3 m in the data sets examined, the results obtained for the first class of wave heights (Figure 6.4a) are very similar to those obtained for the full data set (Figure 6.3). However, when H_s is above 3 m the variance of the errors associated to the WERA estimates increases considerably, exceeding the values obtained for the Seaview retrievals. The variances of the errors in the wave energy period estimates are also affected by the sea state, but contrarily to wave height, show less variance at the upper range of wave heights. This is also the case of wave direction, which seems to be much more stable when the wave height is above 3 m.
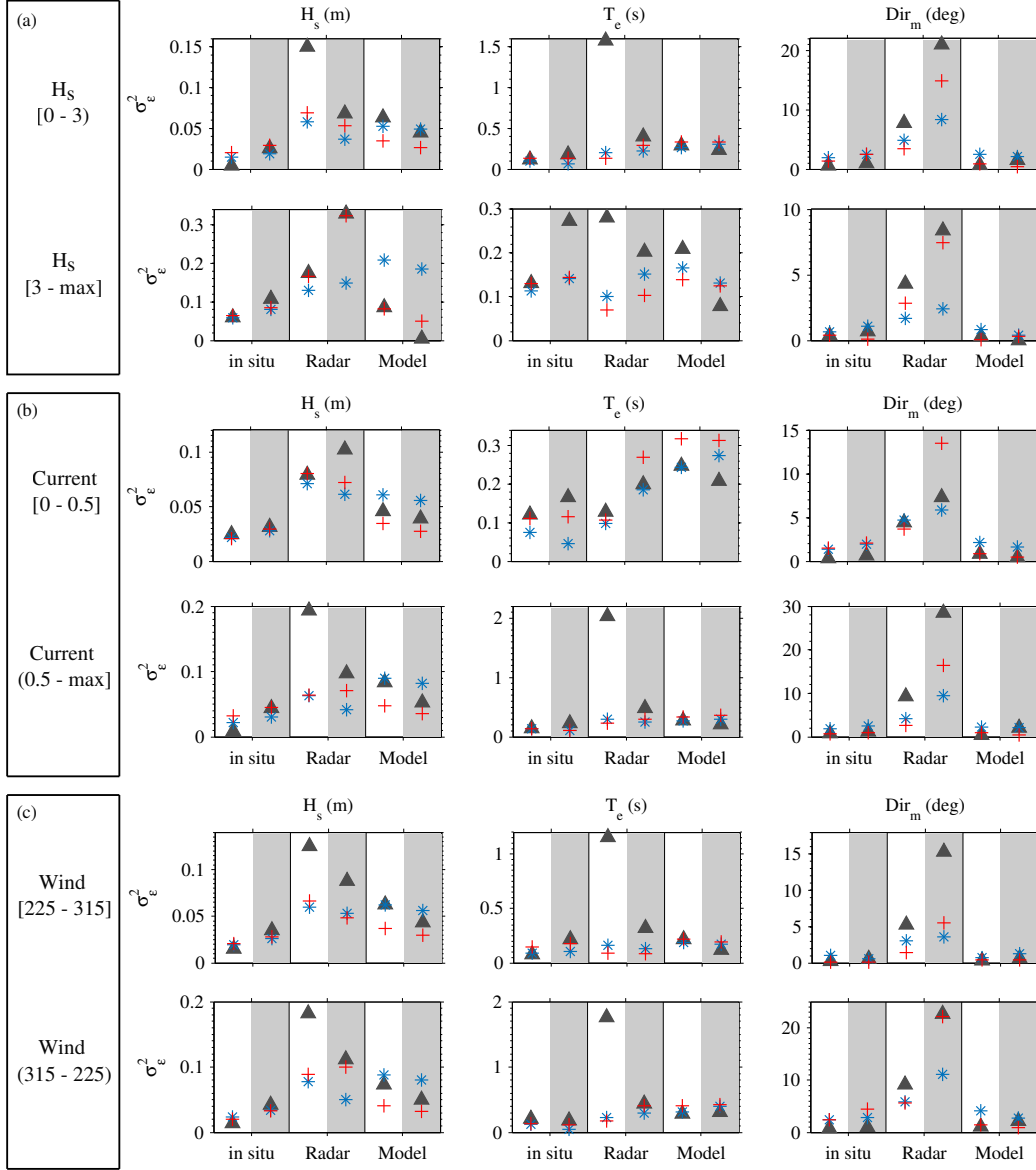
Figure 6.4: Triple collocation estimates of the error variances of the radar, in situ, and model (left) H_s, (middle) T_e, and (right) Dir_m. Panel (a) shows the results obtained discretizing the data in two classes according to the in situ H_s value. In (b) the results were obtained for two classes depending on current speed, and in (c) the data were binned according to the model wind direction. The results were calculated at the locations of the in situ devices: buoy (blue asterisk), ADCP-E (red cross) and ADCP-W (grey triangle), and using the Seaview (white columns), and WERA (grey shaded columns) data sets.

In the previous two chapters, high current speeds were seen to be detrimental to the radar estimates. The variance of the errors was therefore examined for two groups of data classified according to current speed (Figure 6.4b). The results show an evident increase in the error variances with current speed. The H_s and

T_e estimates obtained with Seaview, and the mean direction retrieved by WERA at the ADCP-W site, are the most affected by the high current speeds.

The last environmental variable used to classify the data was wind direction. The results are shown in Figure 6.4c, where it can be seen how the variance of the errors is similarly distributed in the two direction subclasses. In fact, the variance of the errors in the in situ parameters remains almost identical under the two wind regimes. This is also the case of the Seaview retrievals of H_s and T_e, which, with the exception of the results obtained at the ADCP-W site, are also stable and seem relatively insensitive to wind direction. The products of the WERA algorithm, on the other hand, seem to be more susceptible to this variable. In particular, the error of the H_s obtained at the ADCP-E site is seen to double its variance when the winds blow from directions other than the west. A similar result was obtained for the wave directions retrieved by both approaches, which are seen to increase their error variances for wind blowing from the sector comprised between 315° and 225°.

6.4   Discussion and conclusions

The specific method used to invert the radar backscatter into an estimate of the ocean wave spectrum that generated such backscatter will result in slightly different results. The first difference between the two schemes examined here is their differing data return rate, which is an average 20% lower for Seaview as compared to WERA's algorithm. Although an exhaustive analysis was not conducted to confirm it, our hypothesis is that the difference is due to the additional 5 dB in SNR required by Seaview in order to perform the wave inversion. The differing signal requirement is related to the increased complexity of Seaview's algorithm, which retrieves the full directional spectrum, while the semi-empirical approach only produces estimates of the omnidirectional spectrum. Nonetheless, and in

view of the good results obtained with the semi-empirical algorithm, a reduction of 5 dB in the SNR threshold, which could result in a 20% increase in retrieved data, merits further investigation.

In terms of parameter estimation, our results agree with Gomez et al. (2015), who similarly to us found a slightly better performance of the WERA algorithm in retrieving significant wave height at the wave buoy site, and a superior skill of Seaview for the other two parameters evaluated. Here, examination of the estimates for different frequency bands revealed further insight into the relative performance of each method. At the lowest frequency band, and excluding estimates of H_s, both algorithms are barely correlated to the in situ measurements. As mentioned in the previous chapter, discrepancies between methods at these low frequencies are not exclusive to comparisons involving radar estimates, but commonly reported for several wave measuring techniques, which are all affected by the high sampling uncertainty associated to the small long waves characteristic of this band. The agreement improved on the energy containing part of the spectrum, where Seaview performed better than WERA for all the parameters evaluated. At the high end of the spectrum, only the wave height and mean direction estimated with WERA show any correlation to the in situ measurements. The inaccurate short wave periods derived from the semi-empirical scheme evidence the disagreement of the spectral shape at the high frequency band obtained with this method.

Further comparison between methods was performed by examining the variance of the errors in the three parameters evaluated. The spatial location within the radar's coverage was found to greatly affect the error variances of wave height and period, which were found to be significantly higher at the ADCP-W site. This result is in accordance to what was reported by Caires (2000), who states that the variance of the sampling errors associated to radar measurements depends mainly on the location of the measurement within the radar's coverage. Sova (1995) and Krogstad et al. (1999), on the other hand, found that the variance of the sampling

errors associated with the radar's H_s measurements depends mainly on sea state, which in the case of H_s, translates to a dependence on its own value. However, according to Caires (2000), the results obtained in Sova (1995) are not realistic because the sampling errors were derived from Monte Carlo simulations based on synthetic data. Consequently, the estimated sampling errors do not take into account the different signal to noise ratio of the measurements, or the influence of split peaks on the spectra; two factors Caires (2000) found to greatly affect the measurements and their associated errors. Our results agree with Caires (2000) in that the effect of split peaks generated by sidelobes and current variability, which becomes important in the south-eastern part of the domain, represents the main contribution to the variance of the errors. Besides the spatial location within the radar's domain, our results coincide with Sova (1995), and show that the variance of the errors in the H_s estimated by both algorithms is associated to its own value, increasing with higher wave heights.

The effects of other environmental variables on the results obtained with the two approaches was also examined through the variance of the errors associated to different scenarios. Differences between algorithms arose when studying the variance of the errors in wave energy period, and while Seaview's T_e is more affected by high current speeds, WERA estimates reach their maximum error variance when the wind is blowing from the eastern sector. Error variances in wave direction are also mostly affected by the direction the wind is blowing from, and reach maximum values when this is from the sector comprised between 315° and 225°. The exception to the latter is found at the ADCP-W site, where the wave direction estimates derived from both algorithms increase their error variance with increased current speed, confirming its contribution to the occurrence of split peaks over the area located at high angles from Perranporth, where the ADCP-W was located.

In summary, both algorithms are capable of providing highly accurate estimates of significant wave height, which were nonetheless seen to be affected by sidelobes

and current variability at the south-eastern part of the radar domain. Under these unfavourable conditions, the wave height obtained from the semi-empirical approach shows a lower component of error variance as compared to the retrievals from the numerical inversion. It was hypothesised that the way the two algorithms delineate the first- and second-order Doppler signal might be responsible for this difference. Therefore, implementing in Seaview a technique similar to that used in the WERA algorithm could improve the results. As opposed to the spectral energy content, wave period and direction showed further differences between schemes. When examined at different frequency bands, the agreement between Seaview's estimates and the in situ measurements was found to be better than that obtained for the semi-empirical estimates at all the frequency ranges, but the lowest (0.05 - 0.1 Hz). Following the results obtained, the use of the wave period and direction retrieved by the WERA algorithm is only recommended if the interest is on the bulk of the spectrum.

Chapter 7

Characterising surface currents, waves, and their interactions from HF radar measurements

The aim of this chapter is to offer an overview of the surface currents off the Cornish coast and link them to changes observed in the wave field. The general patterns of the surface circulation, as well as the wave climate measured during the eight months analysed in this research are first described. Observed interactions between the two are then examined.

7.1   Introduction

Ocean waves propagating through an unsteady and spatially varying current field modify their statistical properties as a result of the interaction processes reviewed in Chapter 2. Although with some limitations (i.e. Tamura et al., 2008; Van der Westhuysen, 2012), the effects of the surface current upon the wave field are represented in the formulation of wave action conservation, hence phase-averaged

wave models are commonly used to study wave-current interactions (Tolman, 1991; Ris and Holthuijsen, 1996; Guedes Soares and de Pablo, 2006; Tamura et al., 2008; Ardhuin et al., 2012; Van der Westhuysen, 2012). Quantitative spatial measures of both waves and surface currents are, on the other hand, rather scarce (Liu et al., 1989; Masson, 1996). Given that HF radars are capable of producing estimates of both surface currents and waves, this chapter intends to examine the usefulness of these data to observe such interactions, and contribute to fill the current gap in spatial measurements of waves and surface currents.

HF radar's dual capability of measuring surface currents as well as waves has not yet been extensively exploited in wave-current interaction studies, but some cases exist. Examples include the investigation of temporal and spatial variability of the short wave directions in the vicinity of atmospheric and oceanic fronts (Hisaki, 2002), identification of locations of enhanced local wave heights near the mouth of an estuary (Haus et al., 2006), analysis of the fetch-limited growth of wave energy over a region characterised by a strongly sheared current (Haus, 2007), or the energy evolution of a wind-sea propagating toward the coast (Ramos et al., 2009). However, with the exception of Hisaki (2002), these works only used the significant wave heights retrieved by the radars. Analysis of other statistical descriptors of the wave spectra is however mostly limited to validation studies, while their use in scientific research has been very limited. This chapter therefore intends to analyse wave periods and directions estimated by Seaview, in terms of their response to the tidal current that flows across the area twice per day.

7.2   Data and methods

7.2.1   Surface current

The surface current data set was derived from the same backscattered signals
used for wave inversion, collected between April and November 2012. Over this
period, the radars were operational 98% of the time, and retrieved surface current
information was close to 100% at most cells within the wave coverage area (Figure
7.1).
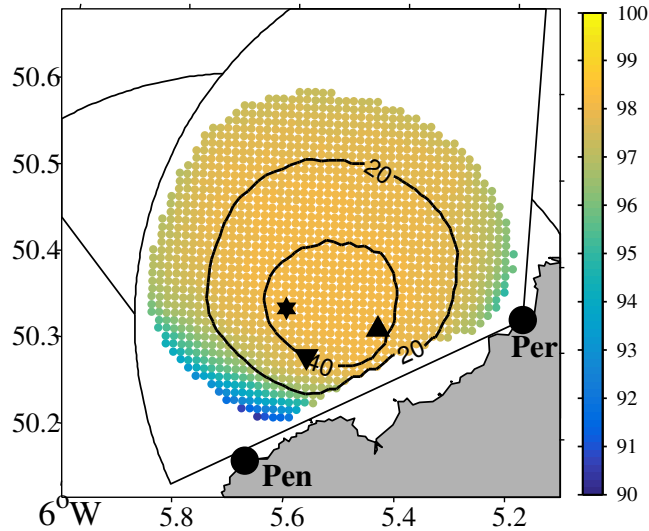
Figure 7.1: Temporal data coverage shown as a percentage of the time each cell within
the radar's wave coverage had surface current information over an 8-month period. The
two black contours demarcate the areas where wave data were available 20% and 40% of
the time. Radar stations (black circles), their wave coverage (fans) and in situ mooring
devices are also depicted: wave buoy (star), ADCP-W (inverted triangle) and ADCP-E
(triangle).

Initial processing and quality assessment of both radar and ADCP measurements
was performed as described on Chapter 3. Then, the accuracy of the radar surface
current was assessed through comparison against the uppermost bin of the ADCP
measurements. The latter was obtained after removal of the first 10% of the
water column, in order to avoid sidelobe contamination. Correlation analyses
were performed on the north and east components of the current measured with

the two techniques, and common descriptive statistics were calculated as described in Chapter 3.

The tidal signal was extracted from the complex-valued current vectors using the least-squares method implemented on the T-tide Matlab software of Pawlowicz et al. (2002). Rotary spectral analysis (Gonella, 1972) was then carried out on the surface current measured at the locations of the two moorings. The power spectral and cross-spectral density of the complex-valued current was first obtained applying Welch's method to 512-h sections of data with 50% overlap, and a Hamming window. These were then used to calculate the rotary components as described in Emery and Thomson (2001). Finally, the residual current was obtained by time-averaging the vector components of the full measured signal at each grid point. These averages were then used to obtain the vorticity and divergence fields over the study region.

7.2.2   Wave data

Following the results presented in the previous chapters, the data set obtained with the Seaview software was selected for investigation of wave-current interactions. Although gaps are widespread in this data set, the estimates have proven to be generally more accurate than the results of the empirical algorithm in terms of wave direction and period. Notably, the variance of the error in the semi-empirical wave directions calculated in Chapter 6 was found to be significantly higher than that obtained for the Seaview estimates. Regarding the errors of the latter, these were seen to be significantly affected by spurious returns from sidelobes, particularly at the southern part of the domain. In this chapter, their effect has been mitigated through a strategy designed for such purpose. The methodology is presented in the following section, and the data used in the rest of the chapter have been treated with it.

The selected data set is therefore that analysed on Chapter 5, obtained from the inversion of radar backscattered signals acquired between April and November 2012, using the Seaview software. The only modification to the data presented in Chapter 5 is an increase of the maximum gap that was interpolated. The intention of the previously presented analyses was to evaluate the skill of the algorithm, hence only short gaps of maximum 3 h were linearly interpolated, in order to preserve the original features of the data as estimated by the algorithm. However, the aim of the present chapter is to observe and analyse any trends in wave parameters, and link them to known effects inflicted by surface currents. Increasing the data availability therefore becomes crucial, hence the maximum interpolation gap was increased to 6 h. Additionally, the interpolation method was substituted by a least squares approach, capable of reproducing the trends on the data more accurately than a linear interpolation.

In addition to the radar estimates, wave and current measurements collected by the three in situ devices described in Chapter 3 are used for comparison with the radar outputs. Spatial information is provided by the wave model described in Chapter 3. As it was mentioned there, the model was run including both water levels and surface currents, and is therefore expected to be able to resolve the surface current effects upon the wave field.

7.2.2.1 Mitigation of sidelobe effects

In the previous chapters, antenna sidelobes were seen to introduce spurious energy at the low frequencies of the wave spectra retrieved by the radar, affecting the estimates obtained at the location of the ADCP-W and deeming the results unusable in some cases. A mitigation strategy has therefore been designed with the aim to detect and correct these erroneous spectra.

At high angles from the radar's boresight, the beamforming technique used by phased array systems to get azimuthal resolution and digitally steer the beam to the desired direction looses accuracy, the beam gets broader, and the antenna side-lobe levels are not effectively reduced. This increases the sensitivity to unwanted signal returns from areas outside the main lobe, hindering wave estimation, especially in the presence of strong currents which vary across the radar coverage.

An example of the above is shown in Figure 7.3, which depicts two Doppler spectra measured at 28 km range from Perranporth, but at different steering angles. In the figure, is possible to appreciate how the Bragg peak of the spectrum obtained at 14.6° (cell 3757) (Figure 7.2) from Perranporth's normal appears as part of the signal obtained at 45° (cell 3682), where the ADCP-W was deployed. As explained in Wyatt et al. (2005), when the differences in first-order Doppler shifts along the same range are large, the Bragg peaks originating from directions other than that of the main lobe can be incorrectly identified as second order structure, and result in large low frequency components in the estimated ocean wave spectrum (Middleditch, 2006).
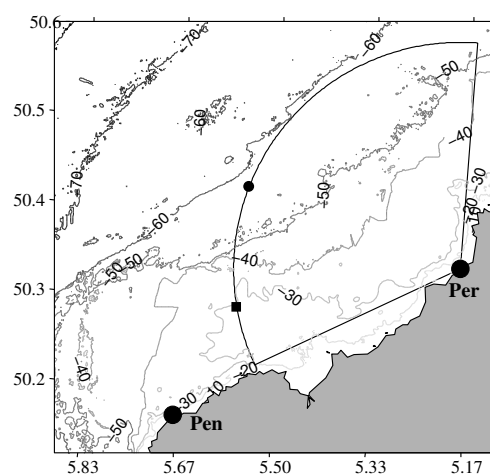
Figure 7.2: Map showing the two cells used to study the effect of sidelobes and current variability on the Doppler spectra. The arc shows the 28 km range from Perranporth's station. The dot indicates the location of a cell located at 14.6° from Perranporth's boresight (cell 3757), and the square is the location of the ADCP-W (cell 3682).

The effects of sidelobes and current variability was therefore studied through analysis of the Doppler spectra collected at the two cells shown in Figure 7.2. It was observed that when the difference in Doppler shift differed more than approximately 0.1 Hz from one location to the other, the first order peak of cell 3757 appeared at the second order region of Doppler spectrum obtained at cell 3682. Further investigation revealed that the latter occurred more frequently when the current speed was larger than 0.6 m s^{-1}.
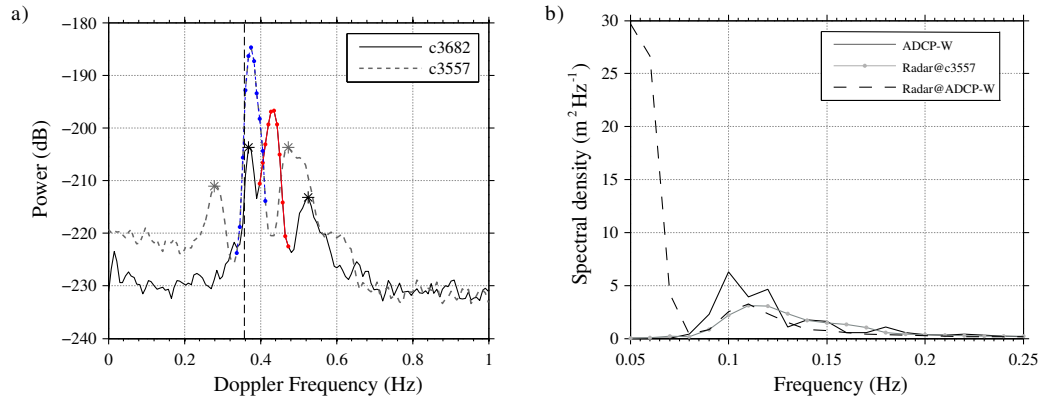
Figure 7.3: Radar measurement affected by antenna sidelobes. Panel a) shows Doppler spectra measured at cells 3682 (black solid line, and red demarcating the first-order region) and 3557 (grey dashed line, and blue demarcating the first-order region). The second-order peaks are marked with asterisks. Panel b) shows the ocean frequency spectra derived from the radar Doppler spectra shown in panel a), and that measured in situ by the ADCP-W. The spectrum obtained at cell 3557 is shown in grey, that obtained at the position of the ADCP-W (cell 3682) is the black dashed line, and the in situ measurement is the black full line.

The effect of the spurious Doppler energy was seen to affect the ocean frequency spectra at frequencies below 0.1 Hz. In order to design a filter to remove it, the wave frequency spectra derived from Doppler spectra flagged as having a large separation between Bragg peaks at the two chosen cells, were assessed for peaks below 0.1 Hz. If found, the energy in each was compared, and whenever this was 50% larger at the ADCP-W corresponding cell, the result was flagged as potentially erroneous. In order to keep as much data as possible, the spectra were not directly rejected, but reconstructed whenever possible. For that, the first trough of the spectrum at cell 3682 was identified, and all data below that frequency was set

equal to that of cell 3557. The latter requires assuming spatial homogeneity on the swell energy across the distance that separates the two points. Although this is not strictly correct (Ashton, 2011), the error derived from the assumption is certainly lower than that derived from the spurious low frequency energy, and given the low data return, keeping as much data as possible was deemed more important than the small error introduced by the spatial homogeneity assumption.

The above methodology was applied to all grid points located at the southern part of the domain, at angles exceeding 45° from Perranporth's boresight. From the whole data set processed at the ADCP-W site, 11% of the results were flagged as having a large difference between Bragg peaks at the two cells examined. From the flagged spectra, 29% were corrected, while the rest of the records were either discarded because there were no data to compare with at cell 3557, or left unmodified if the difference between the energy below 0.1 Hz of the two spectra was not significant.

7.3   Results

7.3.1   Surface current

As introduced in Chapter 3, the surface current in the study area is largely driven by tides, which typically account for 90% of the measured temporal variability (Howarth and Proctor, 1992). The most energetic tidal component is the semidiurnal M_2, which travels as a Kelvin wave, propagating from the Atlantic into the Celtic Sea, and along the western coast of the UK, until the end of the Irish Sea basin, where is reflected back to travel along the Irish coast (Coughlan and Stips, 2015).

In addition to tides, wind and density gradients are also important forcing mechanisms driving the circulation over the area, and in fact govern the long-term residual flow (Carrillo et al., 2005). Although the thermohaline structure is generally the dominant mechanism from the two, wind forcing becomes important during winter (Brown et al., 2003), when winds blow preferentially from the west-south-west with speeds of about 5 ms^{-1}. During spring and summer the direction becomes more westerly and wind speed decreases to about half the winter values (Pingree, 1980). Thermohaline circulation dominates the flow structure during these months, when thermal stratification develops in areas where there is not enough tidal turbulence to maintain mixing against the input of surface buoyancy through solar heating (Simpson and Hunter, 1974). Tidal-mixing fronts then appear in the transitional zones separating these areas from well-mixed waters that persist where the tidal stirring is strong enough to prevent stratification (Simpson and Hunter, 1974; Pingree, 1975; Pingree and Griffiths, 1978). In addition to the seasonal tidal mixing fronts, persistent localised features also exist around Lands End and north Cornwall, and are related to the interactions of the current with topographical features.

7.3.1.1 Validation

The results of the correlation analysis (Figure 7.4) are very similar at the two sites examined and for the two components of the current, which are in close agreement between radar and current meters. The least correlated variable was the northward component of the current measured at the ADCP-E site, which still resulted in an R value of 0.92. The eastward component of the current showed higher bias (3 cm) than the northward component (1 cm), which is consistent with the stronger east-west currents. Root-mean-squared errors are all below 10 cm s^{-1}, with slightly higher values obtained for the ADCP-W comparison; a result that is also consistent with the stronger currents measured at this site.
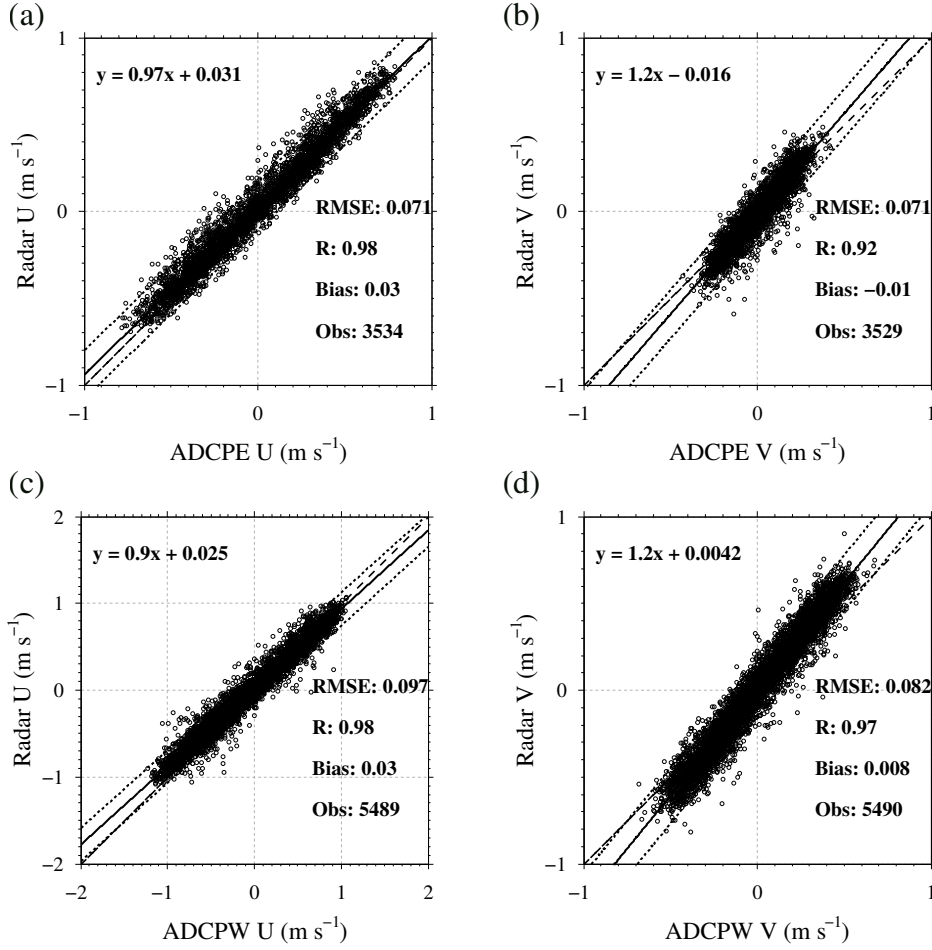
Figure 7.4: Scatter plots of radar- and ADCP-measured current components. Panels (a-b) show the ADCP-E comparison and (c-d) are the ADCP-W results. (a) and (c) are the east component comparisons, and (b) and (d), the north component.

7.3.1.2 Tidal Analysis

A tidal analysis was first conducted to recover the dominant tidal constituents in the study region. The results obtained at the locations of the two moorings indicate that tides account for 92% and 96% of the current variability measured at the ADCP-E and ADCP-W sites, respectively. The semi-diurnal constituents (M_2, S_2, N_2, K_2) are the main contributors to the variance of the signal, followed by quarter-diurnal (M_4), sixth-diurnal (M_6), and diurnal (K_1) components. The significance of the higher order harmonics, M_4 and M_6, shows the importance of

the non-linear interactions between the tidal flow and the coastal topography in the area.

(a)   (b)
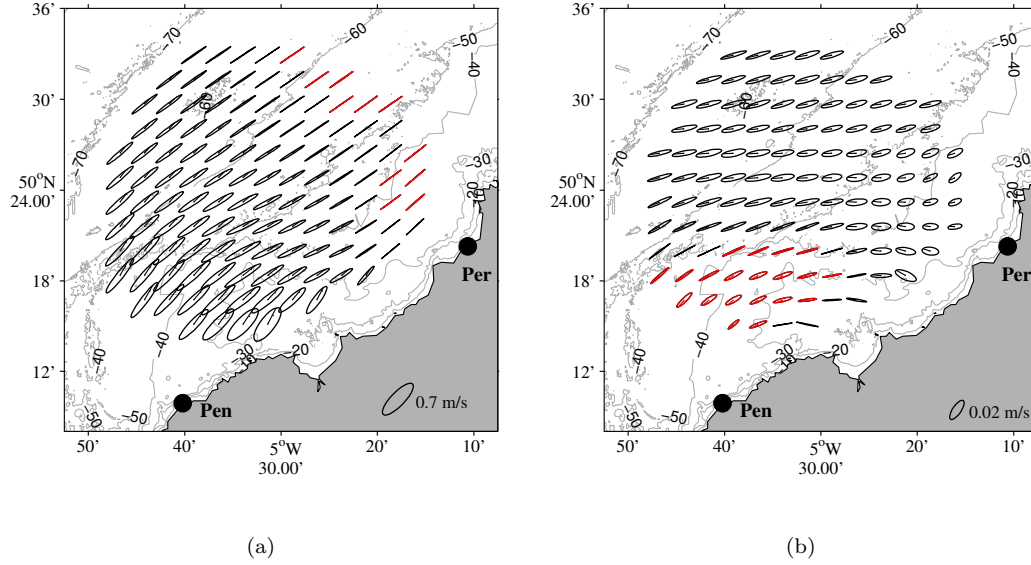
Figure 7.5: Tidal ellipses for the (a) M2 and (b) K1 tidal constituents obtained from the analysis of the surface currents measured over the period April - November 2012. Clockwise rotating ellipses are depicted in black, while those with counter-clockwise rotation are shown in red.

This influence can also be seen on the tidal ellipses of the M_2 and K_1 constituents shown in Figure 7.5, which align with the bathymetric contours, especially at the southern end of the domain. Offshore and north of that area, the ellipses of the M_2 are orientated toward the north-east and almost rectilinear, while the K_1 ellipses have their major axis more eastward oriented, and have a slightly more circular shape. The eccentricity of the M_2 ellipses, defined as the quotient between their major and minor axes, decreases over the shallow area, where the current is further constrained against the coast. Contrarily to the rectilinear ellipses observed at the northern part of the domain, which are the result of a current flowing backwards and forward, the behaviour of the current in the southern part of the domain is closer to a vector rotating about a point, and consequently, the ellipses become closer to a circle. Over the same region, the ellipses of the diurnal component have high eccentricity, but change the rotation to counter-clockwise, probably because

of bottom friction effects. The change of rotation is not seen on the M_2, which
conforming to the expected behaviour of a progressive wave travelling northward,
and subject to the effect of Coriolis force, rotates clockwise over most of the
domain.

7.3.1.3   Spectral analysis

Spectral analysis at the two mooring sites was conducted for a further investigation
of the main features of the surface current. Rotary spectra derived from the radar
measurements at these locations are shown in Figure 7.6. The results, very similar
at the two sites, show a clear tidal dominance of the surface current, with peaks at
diurnal, semi-diurnal, quarter-diurnal, and sixth-diurnal frequencies. The rotary
components suggest a low polarization of the current, with a nonetheless greater
variance contained in the clockwise rotations.
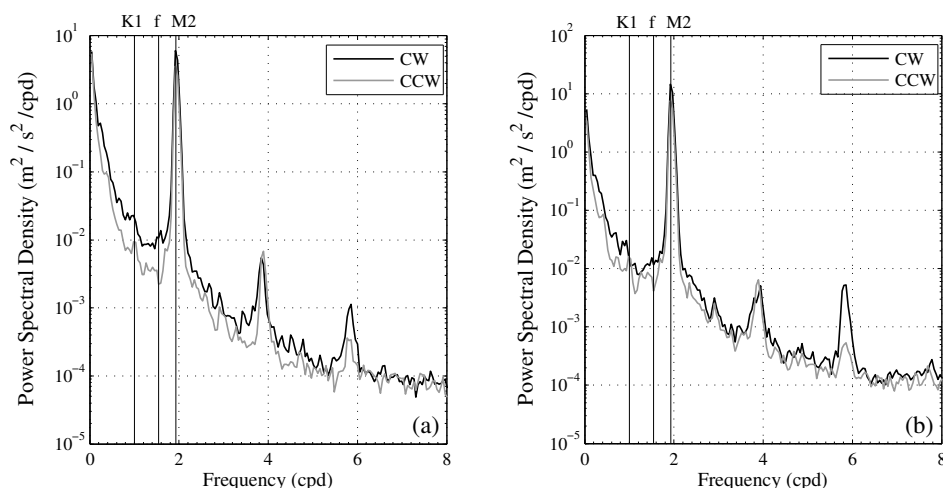
Figure 7.6: Power spectral densities of the radar current measured at the (a) ADCP-E
site and (b) the ADCP-W site. As indicated in the legend, the grey line shows the
counter-clockwise fluctuations and the black line indicates the clockwise fluctuations.
The approximate frequencies of the K1 and M2 harmonic components, and the inertial
frequency at this latitude are shown with vertical black lines.

7.3.1.4 Residual current

The residual flow was obtained by averaging the radar surface currents during the complete period of available measurements, as well as for each of the eight months that conform the dataset. Accordingly to what was found in Brown et al. (2003) for most of the Celtic Sea, the results reveal a net north-eastward flow with maximum speeds of about 0.1 ms^{-1} throughout the eight months analysed (Figure 7.7a). Additionally, the monthly means reveal an alternation between the latter
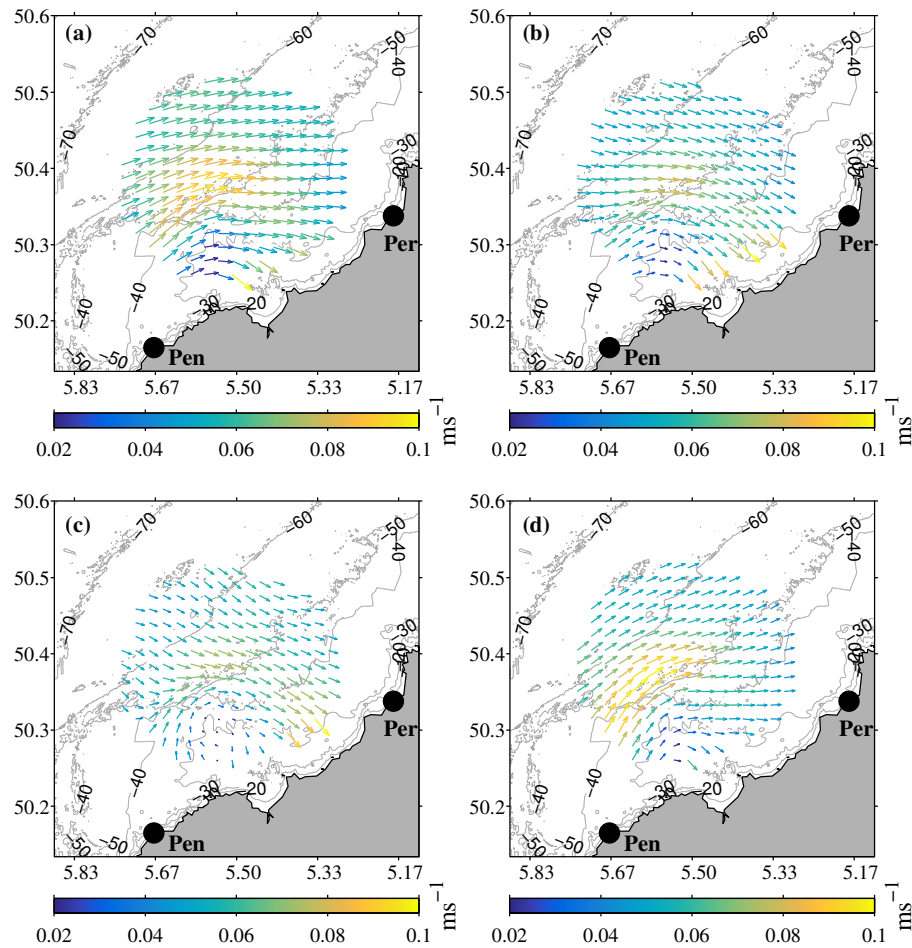
Figure 7.7: Mean surface current for (a) the period April to November 2012, (b) April, (c) July, and (d) October 2012. Vectors indicate the time-averaged current, and their colour indicates their magnitude, according to the colour bars below each figure. The units are ms^{-1}. Only half of the vectors are shown for clarity.

and a more eastward flow during April, July (Figure 7.7c), and September. This variability appears to be related to the wind direction (not shown), which was predominantly from the west-north-west during the months of eastward flow dominance, as opposed to the more common situation of south-western winds.

At the south-west part of the domain, in the vicinity of the 40 m isobath, eastward flows such as that observed in Figure 7.7c are strongly deflected and strengthened toward the north. The result is an along-shore flow that persists until reaching the region of straight isobaths further north, where the vectors are seen to veer east to move in a shore-normal direction again. During July (Figure 7.7c), this circulation pattern results in the formation of a clockwise rotating eddy-like structure off St. Ives bay, at the southern part of the domain. Although a fully formed eddy cannot be observed, a similar pattern, with a close to zero net flow appears at the same region in September (not shown).

Spatial variations on the mean current magnitude (Figure 7.7a) appear to be mainly controlled by the topography, which plays a significant role in modifying coastal tidal currents. An acceleration of the flow is visible over the area of greatest bathymetric gradient, in the central part of the domain, where the squashing of the tidal current, and its non-linear interaction with the topography produce a jet-like residual current (Pingree and Maddock, 1985). Toward the north, where the isobaths are further spaced and rectilinear, the flow is weaker, and its offshore direction and strength are barely altered.

The flow deflection observed in Figure 7.7c is translated into a region of increased positive vorticity close to the 40 m isobath (Figure 7.8), in the south-western part of the domain. The stretching and squashing of the water column as it flows across water depth contours, together with frictional effects, are responsible for the generation of vorticity in this area of complex bathymetry (Pingree and Maddock, 1985).
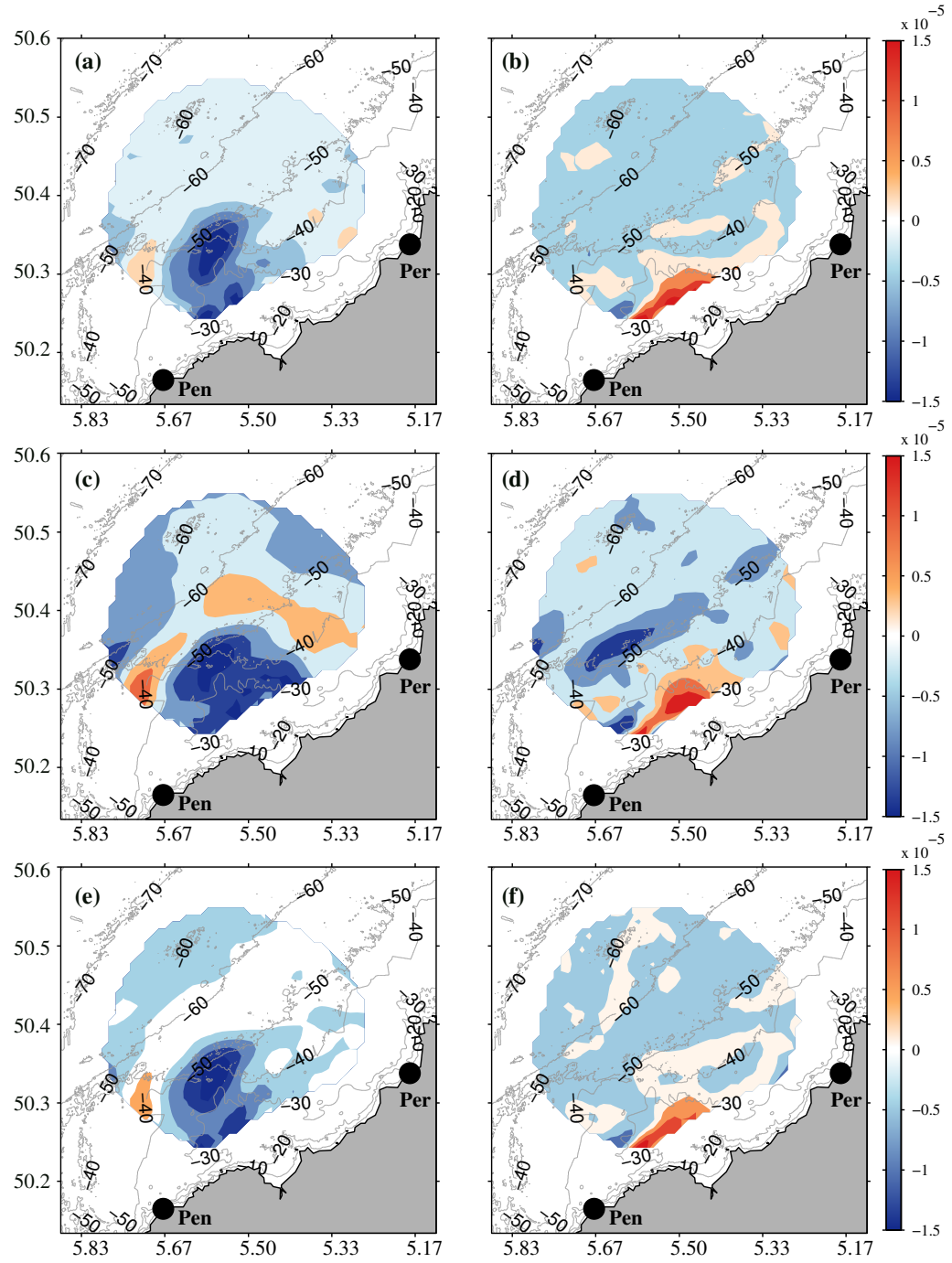
Figure 7.8: Relative vorticity (left column) and divergence (right column) calculated for (a, b) the period April - November 2012, (c, d) August, and (e, f) October 2012. The units are s^{-1}.

Although positive values of vorticity are observed throughout the eight months

analysed, both the magnitude and extent of the CCW rotating residual flows increase during the spring/summer months, with the maximum occurring in August (Figure 7.8c). It is therefore anticipated that this observation is associated to the effects of density stratification characteristic of these months (Pingree, 1975; Hill et al., 2008.

On average, the highest vorticity magnitudes obtained for the 8 months analysed are negative, and appear in the southern part of the domain, coinciding with the region of lowest depths. As found in Pingree and Maddock (1985), the effects of bottom friction and the Earth's rotation on a clockwise rotating flow work in the same sense, and the residual currents are directed clockwise (in the Northern Hemisphere). The divergence (Figure 7.8b) shows low negative values over most of the domain, with the only exception of a strip of positive values located at the area facing the coastline. The last two rows of Figure 7.8 depict the spatial distribution of vorticity and divergence during the months August and October, which are representative of the general patterns during the spring-summer and autumn-winter periods, respectively. While August (Figure 7.8c-d) is characterised by a high vorticity convergent region, the observed pattern during October is very similar to the 8-month average, with a patch of rotating flow localised at the southern part of the domain, and low values of both vorticity and divergence throughout the rest of the measurement region.

As mentioned above, the increased values of vorticity observed during August are thought to be due to the density stratification that develops over the study area during the spring and summer months. To support this hypothesis, the surface current patterns averaged over the period 8 - 14 August 2012 are presented in Figure 7.9 together with information based on sea surface temperature (SST) provided by NEODASS. The SST composite image (Figure 7.9a), reveals a clear dichotomy between the near-shore area on the southern part of the domain, and the offshore waters, where the sea surface temperature was about 3°C higher. The

presence of these two water masses of differing temperature results in the formation of a thermal front in the area of maximum temperature gradient, following the 50 m isobath (Figure 7.9b), and coinciding with a region of steep topographic gradient.
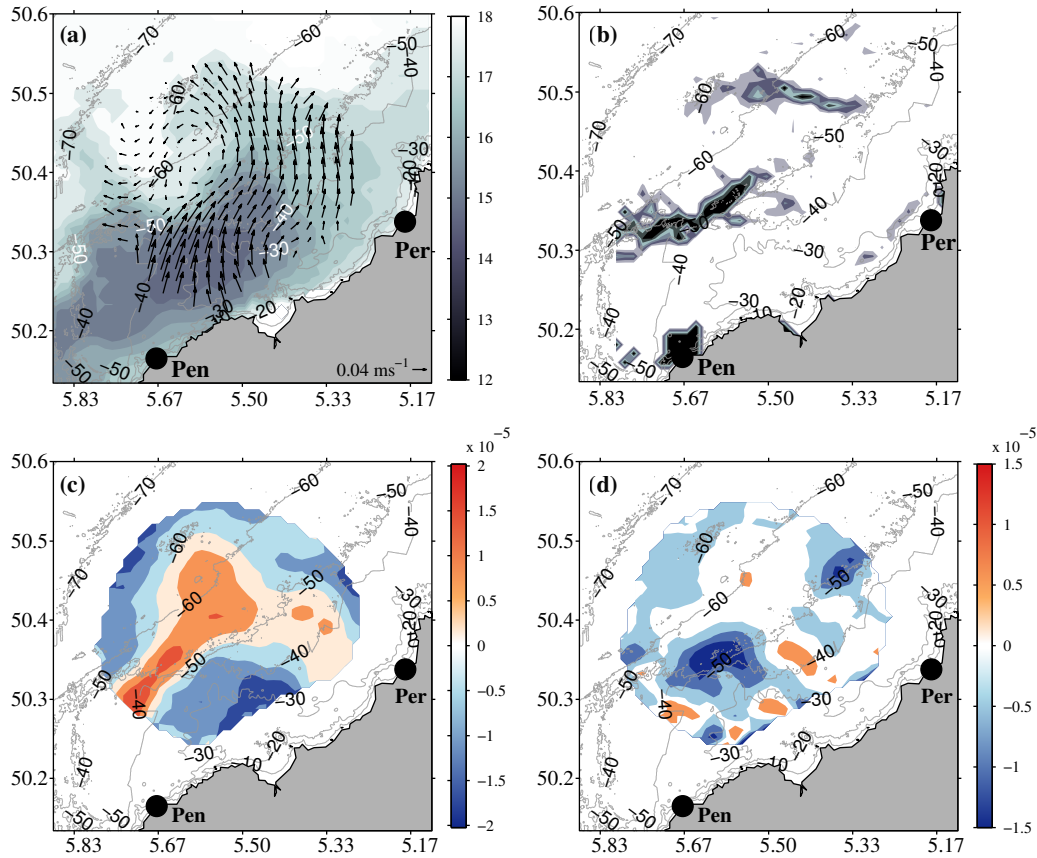
Figure 7.9: Current patterns measured during a week of tidal frontal activity (8 - 14 August 2012). (a) Mean surface current overlaid in a week SST composite. (b) Front position extracted from a composite map (Miller, 2009) calculated during the same period indicated above. (c) Relative vorticity, and (d) divergence. The SST units in panel (a) are Celsius degrees, and the vorticity (c) and divergence (d) are expressed in s^{-1}.

Frontal activity is evidenced by the appearance of a cyclonic eddy (Figure 7.9a), similar to those reported in Pingree (1978), which according to the author are associated to baroclinic instability in the frontal boundary. As a result of the cyclonic motion, the SST shows a hook-like pattern represented by a warm water meander intruding the shallower cold waters. At both sides of the front, the rotational patterns of the surface current oppose each other, and while the offshore

waters show positive vorticity generated by the cyclonic eddy, this is seen to be negative onshore of the 50 m isobath (Figure 7.9b). As a result, a convergent region appears at the separation zone (Figure 7.9d), where the front was located (Figure 7.9b).

7.3.2   Wave conditions

As described in Chapter 3, the wave climate in the study area is a combination of long-period swell and locally generated wind waves, which are both modified by the current field (SWRDA, 2006). Based on the results of a 15-year hindcast obtained with WW3, the latter reference reported prevailing wave directions approaching from the west and south-west, and mean wave conditions composed of waves with 1.6 m significant wave height and 6 s mean period.

The eight months of radar measurements analysed in this work are characterised by wave heights ranging between 2 and 2.7 m across the radar domain (Figure 7.10a), and mean wave periods from 6.3 to 7 s (Figure 7.10d). The prevailing direction is from the west, and the directional spread varies from 43° to 51° throughout the radar's field of view (Figure 7.10g) . The highest mean wave heights are measured offshore, in a strip with west-northwest orientation. The mean H_s is then seen to progressively decrease while the contours slightly align with the bathymetry as the waves refract in their advancement towards the shore. Heights in the upper range of the calculated mean H_s can also be observed at the southern part of the domain. Although the interpretation of the results in this area must be done with caution owing to the sidelobe issue described before, the results of maximum H_s measured in the area (Figure 7.10c) do not point to the presence of outliers, giving confidence in the results. The slightly higher mean H_s obtained here as compared to the averages given in SWRDA (2006), is probably related to the signal-to-noise ratio (SNR) required for the wave inversion. Low sea states are related to SNRs

that are often below the threshold marked by the algorithm, and are commonly
not inverted into wave spectra. Consequently, the results are biased towards wave
heights higher than approximately 1 m, and the calculated temporal mean is biased
high.

The highest means on wave period are obtained for a diagonal strip across the
central part of the domain, between the 50 and 60 m bathymetric isolines. This
same area was seen in the previous section to be subject to a high residual flow.
Furthermore, the region was also found to be a convergent zone, with positive
vorticity during the spring summer months, suggesting that the increased periods
over this area might be a result of an energy redistribution caused by wave-current
interactions.
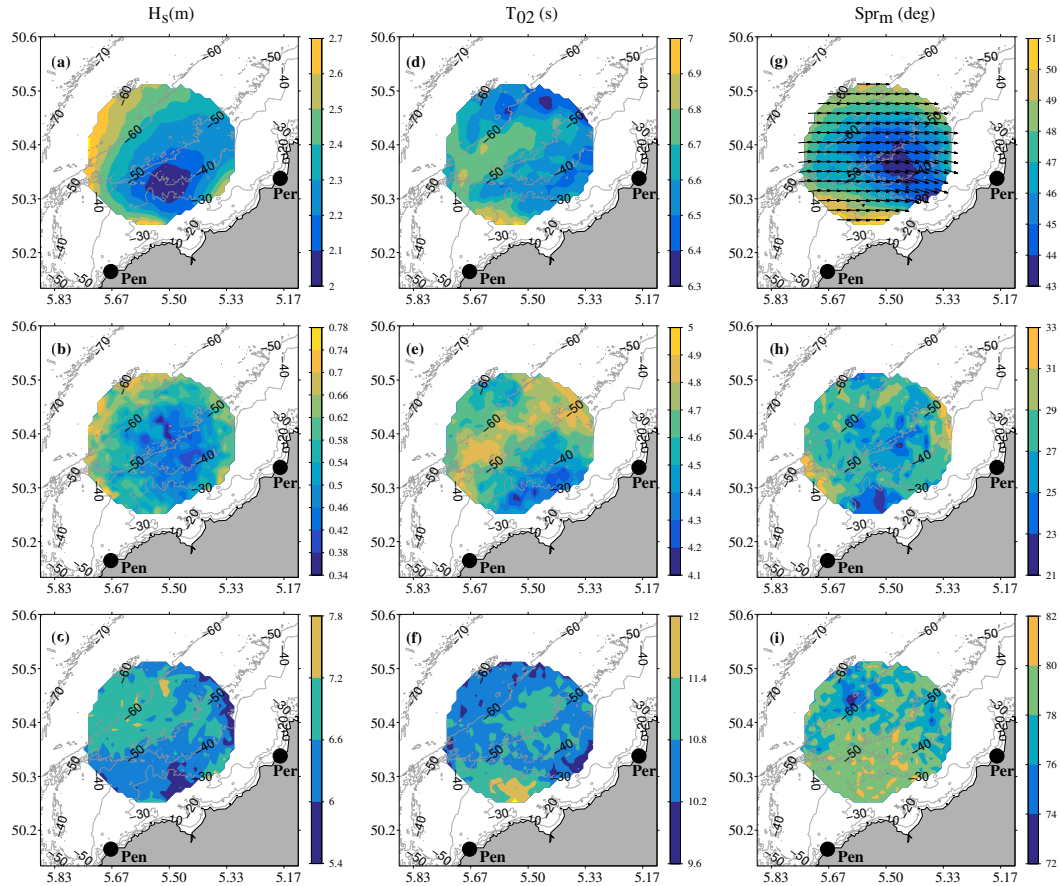
Figure 7.10: Maps of mean (top row), minimum (middle row), and maximum (bottom
row) H_s (a-c), T_e (d-f), and directional spread (g-i) calculated over the period April
- November 2012. The arrows in panel (g) correspond to the mean wave direction
calculated over the same period. Note that the scales in each figure are different.

7.3.3 Observations of surface current effects on the wave field

The relatively strong tidal current that flows across the radar coverage twice per day has been found to modulate the wave parameters measured over the radar domain. The effect can be easily recognized on the wave period and direction time series, which are both affected by current-induced refraction.

Wave direction
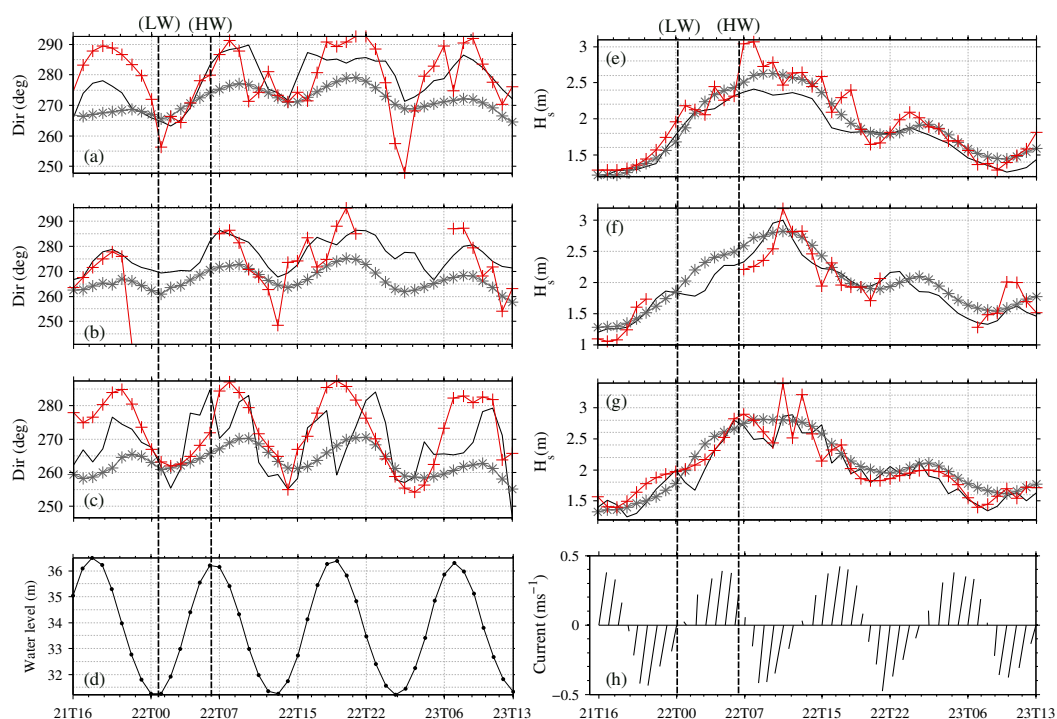
Figure 7.11: Radar-observed (red line and crosses), in situ-measured (black solid line), and modelled (grey line and asterisks) mean wave direction (a - c), and significant wave height (e - g) at the (a) ADCP-E, (b) ADCP-W, and (c) wave buoy sites from 21 June 1600 UTC to 23 June 1300 UTC 2012. (d) Water depth, and (h) current vectors measured at the ADCP-W.

An example of observed and modelled modulations of wave direction is presented in Figure 7.11. The measurements were collected during spring tides, under a strong wind directed to the north-east that had been steadily growing since the early hours of 21 June, until reaching a maximum speed of 14 ms^{-1} on 22 June

at 0700 UTC. Significant wave height and mean period followed the same trend, increasing from about 1 to 3 m, and 6 to 7 s, respectively. After the 22 June, the wind slowed down and both wave height and period decreased accordingly.

Over this period, the tide was seen to affect both the in situ and radar measurements, producing large variations in the mean wave direction, up to 30° between tidal cycles. A modulation of directions is also observed in the modelled results, but the waves only veer about 10° between high and low water. The direction reaches its most westerly position shortly after low water (LW) at both the observations and the model results. Thereafter, waves commence to veer toward the north-west during flood. The northernmost wave approach is seen to occur 1 to 2 hours after HW at the ADCP-E site, both in the observations and the modelled directions. The situation is very similar at the other ADCP site, where the radar estimates are, however, too scarce to comment on them. At the buoy site, the wave direction estimated from the in situ measurements shows a double peak, with a trough in between coinciding with the radar's northernmost wave approach during slack tide. This observation has been found to be relatively common in the buoy data set during spring tides, and might be a result of a decrease in the drag forces exerted on the mooring during slack water.

Wave period

Tidal modulations of the relative mean wave periods were recorded at the mooring sites (Figure 7.12) between 4 and 6 April 2012. Winds were generally strong (higher than 12 ms^{-1}) and blowing from the north-east until the 05 of April at 1200 UTC (Figure 7.12). Thereafter, the wind speed started falling until reaching 6 ms^{-1} on 06 of April at 0400 UTC, while the direction stayed relatively stable from the north-east. The sea state measured over this period was formed by wave heights decreasing from about 4 to 1 m, and wave periods also decreasing

from 8 to 5 s. The wave direction, on the other hand remained stable from the north-north-east during the 3-day period.
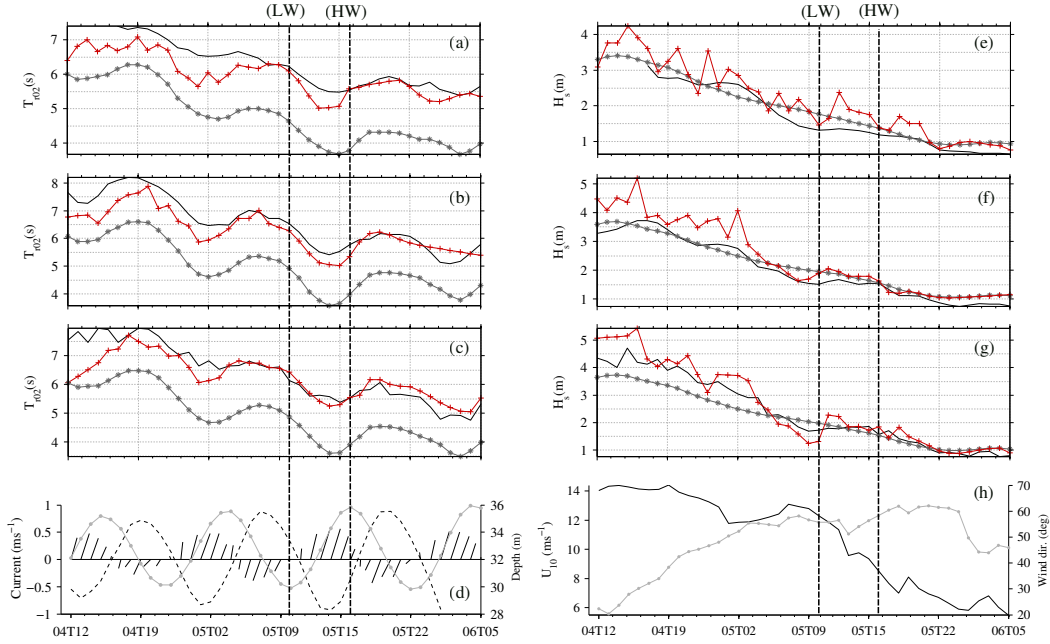
Figure 7.12: Radar-observed (red line and crosses), in situ-measured (black solid line), and modelled (grey line and asterisks) mean relative wave period (a - c), and significant wave height (e - g) at the (a) ADCP-E, (b) ADCP-W, and (c) wave buoy sites from 4 April 1200 UTC to 06 April 0500 UTC 2012. (d) Current vectors (black lines), current on the wave direction (black dashed line), and water depth (grey line and dots) measured at the ADCP-W site. (h) Wind speed (black solid line) and direction (grey line and dots).

The left panel in Figure 7.12 shows the measured and modelled relative period, calculated with Equation 2.11. The plotted parameter shows modulations with a ratio of maximum to minimum wave period of about 1.5 s throughout a tidal cycle. The lowest periods are observed during the flood phase of the tide, when the current opposes the wave propagation. The latter modulation was not observed on the absolute period (not shown), indicating that the inhomogeneity of the current field, and not its unsteadiness, was the main driver governing the variations in wave period (Tolman, 1991). As such, a stationary or slow varying current approximation should accurately describe the observed modulation in relative frequency, which would be equivalent to the opposite of the Doppler shift (Tolman,

1991),

$$\Delta\sigma = -k_0 U_p \tag{7.1}$$

where U_p is the current velocity in the mean propagation direction of waves, and
k_0 is the initial wave number, extracted directly from the measurements. The
results obtained with Equation 7.1 are shown in Figure 7.13 together with the
de-trended relative wave frequency, and show how the quasi-steady approximation
closely matches the measured values.
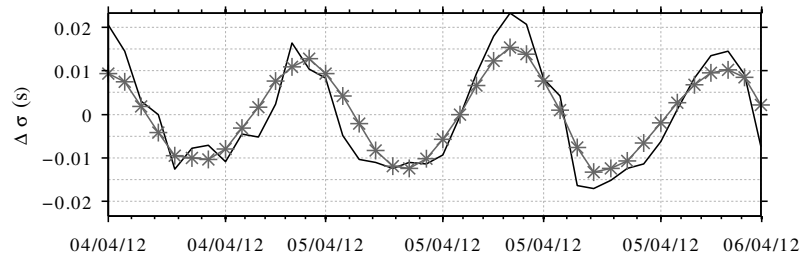
Figure 7.13: De-trended variations in radar relative frequency (grey line and asterisks),
and variations calculated from the quasi-stationary approximation (black solid line),
obtained at the wave buoy site. from 4 April 1200 UTC to 06 April 0500 UTC 2012.

Another case of modulation of wave periods was observed on the last days of June
and the beginning of July. In this case, both waves and wind were propagating
from the south-west, and steadily turning west. Around the first of July, the wind
direction dropped back to the south-west and the waves followed hours later. As
opposed to the previous event, the absolute mean period does show some tidal
modulation in this case, which resulted to be slightly coherent with the current
velocity at the tidal period. The spectral analysis shown in Figure 7.14 shows that
the maximum absolute wave period is reached about an hour before than the time
of maximum horizontal current velocity. The wave model shows similar results, but
the maximum period preceded that of the radar in one hour. The semi-diurnal
peak on relative period occurs about 50 minutes before the maximum current
velocity both in the model and radar results. The direction of the waves measured

by the radar peaked at 3 hours after the current velocity, while that of the wave model was delayed in 2 hours respect to the radar.
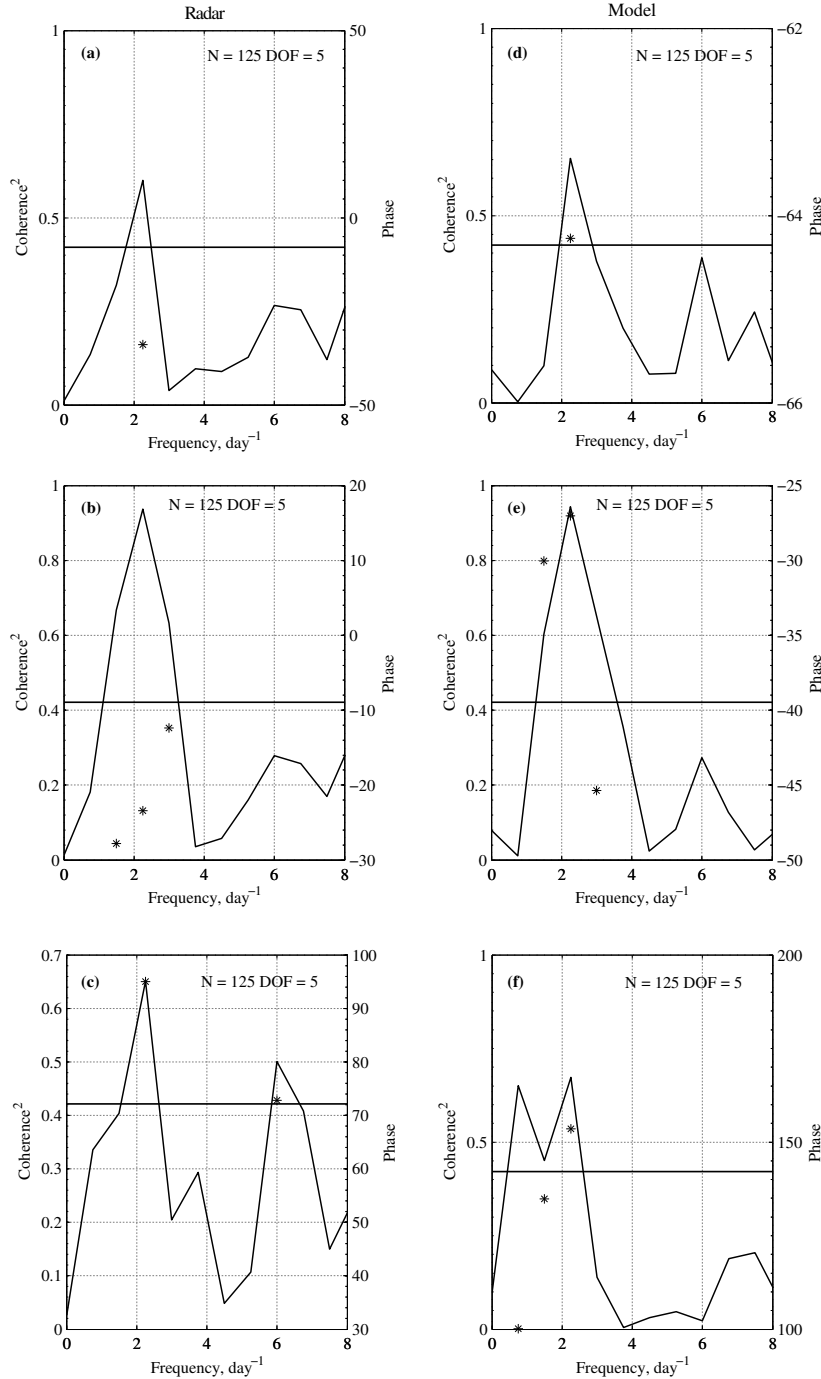
Figure 7.14: Cross-spectral coherence between radar (a-c) and model (d -f) parameters and the east component of the surface current from 29 June 1300 UTC to 03 June 1700 UTC 2012. The parameters shown are (a, d) absolute wave period, (b, e) relative wave period, and (c, f) mean wave direction. The black line represents the calculated cross-spectral coherence (left axis) for each frequency component. The horizontal black line represents the 95% confidence level of the coherence calculation, and the asterisks denote the phase of the coherent frequency components.

The same current gradients that generate the observed temporal modulations in
relative period will also result in spatial variations of this parameter over the
radar domain. This can be seen in Figure 7.15, where differences up to 0.5 s are
observed over the 17 km that separate the two extremes of the transect shown
in Figure 7.15a, which during the studied event was aligned with the direction of
wave propagation.
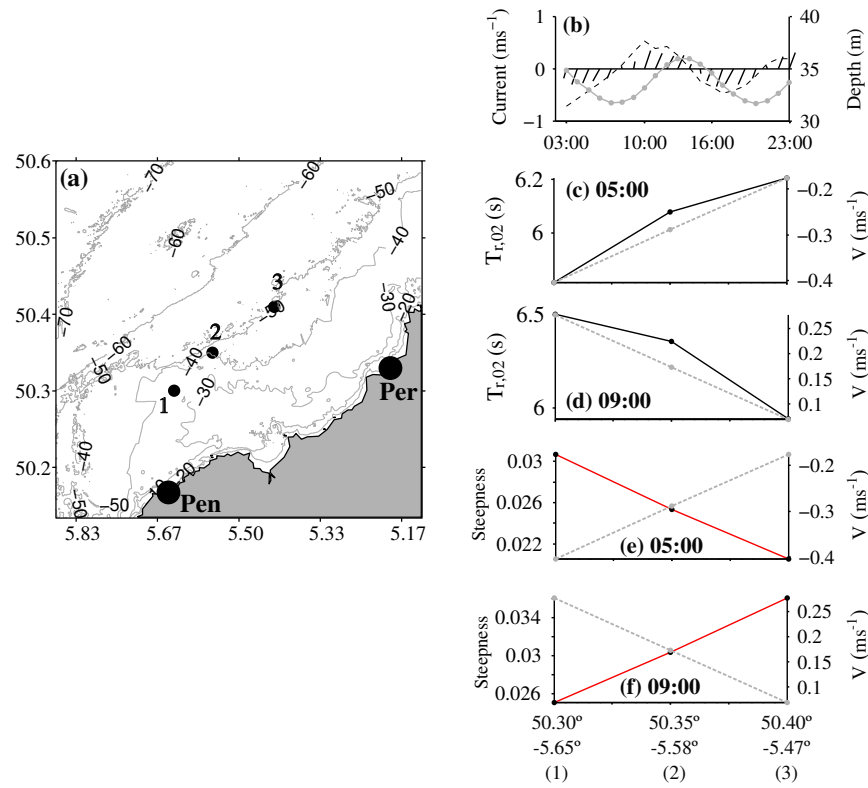
Figure 7.15: (a) Map showing the location of the three points used to study tidal
modulations in wave period. (b) Water depth (grey line and dots), surface current
(black lines), and surface current in the wave direction (dashed line), all measured at
the ADCP-W site on the 30 June 2012. (c - d) Relative period (left axis; black line)
and northern component of the surface current (right axis; grey dashed line) measured
along the transect shown in (a) at the times indicated in the figures. (e - f) Wave
steepness (left axis; red full line) and northern component of current (right axis; grey
dashed line), both measured at three different locations along the transect on the 30
June at (e) 0500 UTC and (f) 0900 UTC.

On 30 June 2012 at 0500 UTC, the wave field was propagating through an op-
posing current with decreasing strength. In this situation, an increase of 0.4 s in

the relative wave period (Figure 7.15c), and a concurrent decrease of wave steep-
ness (Figure 7.15e) was observed as the waves propagated toward the north-east,
where they encountered a weaker opposing current. Four hours later, the wave
field propagated through a decelerating current, which was in this case flowing
in the direction of wave propagation. As a result of the negative current gradi-
ent, the relative wave period (Figure 7.15d) and wavelength decreased. This had
a concomitant increase in wave height, and a consequent 30% increase in wave
steepness between the two extremes of the transect (Figure 7.15f).

7.4   Discussion and Conclusions

The surface current and wave fields obtained with HF radar over an 8-month
period have been described in this chapter. Surface currents were first compared
against in situ measurements acquired with two ADCPs. The results showed a
high degree of agreement between the two techniques, represented by correlations
between 0.92 and 0.98, and a maximum RMSE of 0.01 ms^{-1}.

The results of harmonic and spectral analyses indicated that surface currents are
mainly driven by tides, which account for over 90% of the measured current vari-
ability. The semi-diurnal constituents were found to be the main contributors to
the variance of the signal, followed by the higher order harmonics, M_4 and M_6.
The high contribution of the latter gives an indication of the importance of the
non-linear interactions between the tidal flow and the coastal topography in the
area.

The time-averaged currents revealed a net north-eastward flow with maximum
speeds of about 0.1 ms^{-1}, which are consistent with previous observations made
on the Celtic Sea (Brown et al., 2003). Additionally, the monthly means revealed
an alternation between the latter and a more eastward flow, which appears to be

related to the wind direction. The relative vorticity was found to be predominantly
negative, which is consistent with the slight dominance of the clockwise rotations
in the area. The highest magnitudes appear in the southern part of the domain,
coinciding with the region of lowest depths. An exception to the general vortic-
ity pattern appears during the spring/summer months, when an area of cyclonic
rotation and associated current convergence appears in the area. Investigation of
the residual flow calculated from a week average, together with an SST compos-
ite obtained over the same period, indicated that the rotation pattern observed
was a result of a cyclonic eddy, which developed in the area due to baroclinic
instability (Pingree, 1980) in the vicinity of a tidal mixing front. The existence of
tidal fronts in the Celtic Sea is well known and documented, and these are usually
characterised from SST imagery and data obtained in field campaigns. However,
the level of detail provided by the HF radar surface currents is unprecedented. In
the longer term, these data could constitute an essential piece of information for
the research of the impacts of the wave energy devices located in the Wave Hub
over the current physics. The surface current structure has been found to exert a
major control over the distribution of marine fauna in the area (Cox et al., 2016);
hence, alterations in the small scale circulation caused by the presence of Wave
Hub, can have concomitant effects in ecological distributions, the monitoring of
which can be supported by the type of data presented in this chapter.

The mean wave climate obtained from the radar measurements was characterised
by mean wave heights ranging between 2 and 2.7 m across the radar domain, and
mean wave periods from 6.3 to 7 s. The prevailing mean direction is from the west,
and the directional spread varies from 43° to 51° throughout the radars field of
view. These means are in general good agreement with the results from a 15-year
hindcast obtained for the area (SWRDA, 2006), and only the wave height was
found to result in a significantly higher mean. This was attributed to the signal-
to-noise ratio (SNR) required for the wave inversion, which frequently excludes

low sea states owing to their low SNRs. As a result, the rate of success of the wave inversion is almost proportional to the sea state, and the mean is biased high. The above-mentioned relation between SNR and the energy of the measured sea state, results in different data returns depending on the time of the year. As such, low energetic months like May have almost no data inverted. Consequently, monthly means or other statistics of the wave climate were not included in this work, as these would lack representativeness.

The influence of the surface current on wave phase parameters was investigated at the locations of the three moored devices deployed in the area. The results showed that the unsteadiness of the surface current, which varies both temporally and spatially, can significantly affect the wave field. The periodic changes on the tidal current were seen to modulate the direction of propagation of waves, producing large variations up to 30° in the measured directions, which were almost in phase with the tidal elevations. The wave model was also seen to be able to simulate the oscillation in wave direction. However, the variations are only about 10° and show a smoother pattern, and a slower turning of the wave direction, especially during flood. This is probably related to asymmetries or other fine details of the tidal current, which are not represented by the tidal constituents used in the model. Wave period was also found to be modulated, both owing to effects of temporal and spatial variations of the current field. The first case examined showed waves propagating from the north-east, which were only modulated in their relative period. The strong wind (14 ms^{-1}) that prevailed during the first part of the analysed period, could have generated the six second waves observed only 80 km away from the wave buoy site, and after about 8 hours blowing. It would only then take about 2 hours before these 6 s waves reach the wave buoy site, which is probably why the temporal variations in the surface current in its travel toward the radar domain are not as important as its inhomogeneity. The waves measured during the second case propagated from the south-west, and were

probably generated at a longer fetch. Consequently, they experienced further temporal variations in the current field, which together with the spatial gradients they travelled across during their approach toward the radar domain, resulted in modulations of both the absolute and relative wave periods.

The main advantage of using HF radar outputs to study the effects of surface currents upon the wave field, is the opportunity of investigating the spatial patterns of their interactions. While wave-current interaction studies are usually focused on the effect of steady currents that are either following or opposing the wave field, it is known that the interaction is dictated by the current gradient (Van der Westhuysen, 2012; Rapizo et al., 2016) rather than its direction; hence spatial information is essential for an accurate analysis of tidal-induced modulations. Evidence of the latter was presented in this work through an example of a decelerating surface current flowing in the same direction of the wave field. Although theory predicts a reduction of the wave steepness on the presence of a following current, the results showed an increase on this parameter owing to the negative current gradient the waves travelled through. Given the challenges of modelling the effects of adverse flows on wave propagation, the observations made in this work show that the simultaneous measurement of waves and currents retrieved by HF radar, could represent an invaluable source of data for calibration and validation of models including wave-current interactions.

Chapter 8

Summary and Conclusions

This research work was conceived with the main aim of demonstrating the wave measuring capabilities of HF radar. Although research had previously been undertaken in this field, a review of published works testified that most relied on data collected with radars originally installed and optimised to measure surface currents. The negative implications of the latter are mainly derived from the short measuring periods commonly used for current measurement. These are not long enough to reduce sampling variability impacts on wave estimates (Wyatt et al., 2009), which are consequently affected by random noise. Based on the currently available validations of HF radar wave measurements, it is therefore difficult to separate the relative contribution of the short averaging from additional sources of error, such as those derived from the limitations of technique itself, or the algorithm used to invert the radar backscatter into ocean wave spectra. It is through using longer averaging periods, and two different inversion algorithms, that this research has aimed to discriminate between the artifacts emanating from different sources; thus providing new insights into the advantages and limitations of the HF radar technology in measuring the sea sate.

A secondary aim to this work was to use the validated wave products in combination with the surface currents, also retrieved by the radars, to characterise the hydrodynamic conditions over the radar domain. More specifically, the research sought to evaluate whether the results obtained could be useful in studying wave-current interactions.

The main findings of these two parts of the study are independently summarised below.

8.1   Validation of HF radar wave measurements

Existing inter-comparisons of wave measurements acquired with different sensors suggest that the errors of each of the data sets involved should be accounted for, as even the most reliable wave measuring techniques are subject to errors, which at the very least, will be due to sampling variability (Allender et al., 1989; Krogstad et al. (1999) Graber et al., 2000; Drennan et al., 2003; Pettersson et al., 2003; (Mackay, 2009); Collins et al., 2014). The latter should therefore be calculated and taken into account when comparing the measurements against each other. However, the calculation of sampling variability for remotely sensed products is not straightforward. That of HF radar has been obtained through computer simulation (Sova, 1995), and numerical methods (Caires, 2000). However, the former approach relied on synthetic data for the simulation, and does not recover the real variability of the measurements (Caires, 2000), and the numerical methods have been reported to be inappropriate when the magnitudes of the errors of each technique involved are very different (Caires and Sterl, 2003), which is often the case when comparing the radar's spatial measurements to in situ point measurements. Therefore, a combination of ordinary least square analyses, and the estimation of error variances through triple collocation was adopted in this work.

Applying these statistical techniques, Chapters 4, 5 and 6 were devoted to the analysis of the results obtained with two inversion algorithms, which were then compared to each other in a separate chapter. The results obtained are summarised below, in relation to their contribution to the main objectives set out in Chapter 1.

Estimation of the errors associated to two different inversion algorithms

Chapter 4 focused on the evaluation of a semi-empirical method (Gurgel et al., 2006), used to estimate wave frequency spectra from radar backscatter. This constitutes the first work evaluating all the wave products that can be obtained with the algorithm, and has contributed to gain deeper insight into its skill and the source of the inaccuracies found. The main limitations of the method were found to be related to the use of a prescribed set of coefficients to invert the radar backscatter into ocean wave spectra, and from the linear relation between Doppler and ocean frequencies assumed by the algorithm; two elements that revealed themselves as inaccuracies at both ends of the frequency spectrum. In spite of the often inaccurate shape of the spectra derived from the above limitations, their variance is usually accurately estimated by the algorithm. As a result, the significant wave height has proven to be a very robust retrieval, which can be estimated with Pearson correlation coefficients between radar and in situ measurements above 0.9 over 70% of the time.

Chapter 5 evaluated a second algorithm, based on the numerical inversion of the equation relating the radar backscatter and ocean directional spectrum. This method is not only capable of producing estimates of frequency spectra like the approach evaluated in Chapter 4, but also provides estimates of the full directional spectrum. The directional spectra obtained were seen to be accurate, but of lower resolution than their in situ measured counterparts. Commonly reported limitations of the algorithm have been related to the previously mentioned short

averaging, and a limitation of the theory underpinning the inversion in high sea states. The former fades in this research due to the longer integration times used, and the latter has not been found to significantly affect the wave height estimates evaluated in this work, which reached a maximum value of 7 m that was accurately estimated by the radar. The difference between this study and some of the most exhaustive available validations of the method (i.e. Wyatt et al., 1999; Wyatt et al., 2003) is the frequency at which the radars operate. While our system transmits at 12 MHz, a frequency which until now remained relatively untested in the literature for WERA radars, the aforementioned works used radars operating at 27.75 MHz, a frequency limited in its description of wave heights higher than 3 m.

Further insight into the errors associated to each method was gained from the comparison of their estimates. This work was presented in Chapter 6, and constitutes one of the first evaluations of the relative skill of two different wave inversion schemes for HF radar. The first difference between the two was related to their data return rates, which were 20% higher for the semi-empirical approach, owing to its slightly lower signal-to-noise requirements. Further evaluation was focused on concurrent measurements from the two approaches, and sought to find whether any differences in the quality of the estimates of each method remained when using exactly the same data, with equal signal quality. The results showed that both methods retrieve similar estimates of significant wave height, which were also highly correlated to the in situ measurements. When the focus is not on the variance of the spectral energy, the numerical inversion of the equation that relates the radar backscatter with the ocean wave spectrum performed better than the simple semi-empirical relationship between them. Through examination of the variance of the errors associated to the results of each scheme, it was found that Seaview's estimates of H_s and T_e are further impacted by the issue of split peaks than the results obtained with the semi-empirical approach, which were nonetheless affected

on their wave directions. Furthermore, current speed has been demonstrated to exert a major control over the increased error variance at the ADCP-W site, causing split first-order peaks which are interpreted as second-order structure.

Spatial accuracy of HF radar measurements

The literature reviewed in Chapter 2 not only revealed deficiencies related to using radars optimised to measure surface currents, but also highlighted that most validations of HF radar wave measurements were based on a one point comparison, usually against the measurements acquired with an in situ device located at the centre of the radar's field of view. This does not give enough information regarding the spatial accuracy of the measurements to allow establishing the limits within which the accurate results can be obtained.

From the observations presented throughout this thesis, and more specifically from the results presented in Chapter 4 and 5, it can be established that our radars are capable of producing an accurate representation of the wave field over most of the area within the 20% of Seaview's data availability. The exception is the southern part of the domain, where the radar results are affected by antenna sidelobes and current variability. This was revealed both through comparison with the ADCP-W, located in this area, and also through comparisons against the wave model. A mitigation strategy designed in Chapter 7 was able to remove a large part of the outliers resulting from this issue. However, some remained, and the method eliminates data, which are already scarce, so a better approach should act on the Doppler spectra before performing the wave inversion. Based on these results, an area of about 20-by-20 km can be delimited where accurate spatial maps of wave height, period and direction can be obtained with both methods.

8.2 Characterising surface currents, waves, and their interactions from HF radar measurements

Following the good results obtained in the first part of the thesis, the radar wave retrievals were deemed appropriate to conduct a first evaluation of the hydrodynamic conditions over the study area from HF radar measurements.

First, the HF radar surface currents were analysed to reveal the main aspects of their spatial and temporal distributions. Although the Celtic Sea circulation has been thoroughly studied over years (Pingree and Griffiths, 1978; Pingree, 1980; Brown et al., 2003; Carrillo et al., 2005), the fine detail provided by the spatial measurements analysed in this thesis is unprecedented, and provided close insight into the patterns of the surface circulation in the area.

A tidal analysis revealed a dominance of the semi-diurnal constituents in controlling the tidal flow over the area, but also showed the importance of higher harmonics, characteristic of areas where bottom friction becomes important. Although the former are accurately estimated by circulation models, the modelling of higher harmonics poses further challenges, which can be alleviated by the type of data presented in this work. Moreover, the data proved valuable for detecting and studying the effects of the seasonal stratification present in the study area during the spring and summer months. These results indicate that, if extended through continuous acquisition over the years, a reliable statistical description of the variability of the frontal structures, as well as of their associated circulation patterns, could be extracted from these data. In the area monitored by the radars used in this work, this could have relevant implications for the assessment of the physical alterations derived from the presence of wave energy devices in the Wave

Hub. Furthermore, these data are essential for estimating the ecological implications derived from the modification of the physical environment, and hence the appropriate planning and management of MRE sites (Shields et al., 2011).

Following the surface circulation, the radar's wave retrievals were analysed to extract the statistics describing the wave climate over the area. The results, which were biased high in the mean wave height statistics owing to the quality requirements of the wave inversion, were otherwise in good agreement with published results covering the same area (SWRDA, 2006). The radar's wave data, which proved to be valuable in providing detailed spatial information, are however limited in the characterisation of wave climate statistics owing to the numerous gaps appearing throughout the datasets.

Finally, both waves and currents were simultaneously analysed with the aim of studying their interactions. More specifically, the effects of current-induced refraction onto the period and direction of waves were characterised. The scarce body of research on wave-current interaction using HF radar has been mainly focused on the analysis of significant wave height. However, no prior information existed on the ability of the technique to represent current-induced alterations in the phase parameters of waves. The analyses conducted in Chapter 7 were therefore devised as a first evaluation of the radar outputs for their use in this type of research. Consequently, the focus was on their comparison against the in situ measurements and the wave model, in order to determine whether the radar reproduced the current induced modulations on wave parameters. The results show a high agreement between the three methods, and the adequacy of the radar data for such purpose, with the main limitation represented by the rather discontinuous character of the wave data set. Moreover, the spatial measurements provided by the HF radar have proved valuable in addressing the effects of current gradients in the waves. The data have therefore shown their potential to fill the spatial gap in the measurement of surface waves and currents to characterise their interactions.

In an area such as the focus of this research, where the wave energy resource must be carefully studied and characterised, these data can be an important addition to the already available observations. There is an increasing body of research suggesting that tidal currents can have a significant impact on wave energy (i.e. Saruwatari et al., 2013; Hashemi and Neill, 2014). Neglecting the effects of wave-current interaction could therefore lead to significant errors on the estimations of wave energy resource (Hashemi and Neill, 2014), which could result in incorrect designs and imprecise tuning of wave energy devices (Saruwatari et al., 2013). The relevance of the results presented in this work lies on their ability to map the spatial patterns of the surface current, which are essential for the investigation of their effect upon waves. For example, the parametrization of energy dissipation in the presence of a negative current gradients still poses a challenge for wave modelling (Van der Westhuysen, 2012), and these types of information can be of aid for model improvement and validation. Further research should be focused on evaluating the effects at a spectral level, since this type of observation is very limited in the literature (Rapizo et al., 2016).

8.3   Conclusions

This thesis has shown that with an appropriate configuration, HF radar is capable of accurately measure the sea state. Both a simple relationship between the radar backscatter and the ocean wave spectrum, and a complex numerical inversion of the expression relating the two, were shown to produce very accurate estimates of significant wave height. In addition, the latter method was also seen to generate spectra which were accurate in shape, producing wave period estimates that were in good agreement with in situ measurements. Furthermore, the latter parameter showed lower error variance than a wave model evaluated together with the in situ and remotely sensed measurements. Although each of the two inversion methods

evaluated showed its own advantages and limitations, both were constrained by singularities related to the technique. Specifically, wave measurement at high angles from the radar's boresight, where the pattern of the surface circulation differs from the rest of the radar domain, was found to be challenging irrespective of the algorithm used. In addition, factors such as wind direction, and current speed were found to not only affect the quality of the estimates, but also the data return. These findings point to the important role that environmental conditions have in the quality and extent of the measurements, and suggest that a thorough analysis must be conducted before the deployment of the radar stations. Even more importantly than the evaluation of the accuracy, the work presented here showed that most errors in the data can be identified and linked to their source, which is essential for their detection and removal.

The validation effort conducted in the first part of this work established the accuracy of the measurements, and indicated their suitability to studying the effects of the tidal current upon the wave field. The radar's wave direction and period presented clear evidence of tidal modulations, which were equivalent to those measured by the in situ devices. Furthermore, the radar has shown to be able to add detail to the generally accurate but smooth oscillations estimated by the wave model. The main limitation faced when conducting these analyses was the widespread presence of long gaps in the data sets. This limited the accurate interpretation of trends in the data, as well as spectral analyses, which require continuous data sets. Future efforts should therefore be concentrated in increasing the data return rates. With continuous data, the opportunities of these data are immense, allowing for the validation of models, and to generally further our understanding of wave-current interactions.

References

Allender, J., Audunson, T., Barstow, S. F., Bjerken, S., Krogstad, H. E., Stein-bakke, P., Vardtal, L., Borgman, L. E., and Graham, C. (1989). The WADIC project: a comprehensive field evaluation of directional wave instrumentation. *Ocean Engineering*, 16:505–536.

Anctil, F., Donelan, M., Forristall, G., Steele, K., and Ouellet, Y. (1993). Deep-water field evaluation of the NDBC-SWADE 3-m discus directional buoy. *Journal of Atmospheric and Oceanic Technology*, 10(1):97–112.

Ardhuin, F., Roland, A., Dumas, F., Bennis, A.-C., Sentchev, A., Forget, P., Wolf, J., Girard, F., Osuna, P., and Benoit, M. (2012). Numerical wave modelling in conditions with strong currents: dissipation, refraction and relative wind. *Journal of Physical Oceanography*, 42:2101–2120.

Ashton, I. G. (2011). *Spatial variability of wave fields over the scale of a wave energy test site.* PhD thesis, Exeter University.

Atanga, J. N. and Wyatt, L. R. (1997). Comparison of inversion algorithms for HF radar wave measurements. *IEEE Journal of Oceanic Engineering*, 22(4):593–602.

Barber, N. F. (1949). Behaviour of waves on tidal streams. *Proceedings of the Royal Society of London. Series A*, 198:81–93.

Barrick, D., Evans, M., and Weber, B. (1977). Ocean surface currents mapped by radar. *Science*, 198:138–144.

Barrick, D. E. (1970). The interaction of HF/VHF radio waves with the sea surface and its implications. In *AGARD Conference Proceedings 77*, pages 1–18, Sprinfield, VA. Clearinghouse for Federal Scientific and Technical Information.

Barrick, D. E. (1972a). First order theory and analysis of MF/HF/VHF scatter from the sea. *IEEE Transactions on Antennas and Propagations*, AP-20:2–10.

Barrick, D. E. (1972b). Remote sensing of sea state by radar. In Der, V., editor, *Remote Sensing of the Troposphere*, chapter 12, pages 1–6. NOAA/Environmental Research Laboratories.

Barrick, D. E. (1977a). Extraction of wave parameters from HF radar. *Radio Science*.

Barrick, D. E. (1977b). The ocean waveheight nondirectional spectrum from inversion of the HF sea-echo Doppler spectrum. *Remote Sensing of the Environment*, 6(3):201–227.

Barrick, D. E. (1978). HF radio oceanography - A review. *Boundary-layer meteorology*, 13:23–43.

Birkemeier, W., Long, C., and Hathaway, K. (1996). DELILAH, DUCK94 & SandyDuck: Three nearshore field experiments. In *Coastal Engineering Proceedings*.

Boudiere, E., Maisondieu, C., Ardhuin, F., Accensi, M., Pineau-Guillou, L., and Lepesqueur, J. (2013). A suitable metocean hindcast database for the design of marine energy converters. *International Journal of Marine Energy*, 3-4:40–52.

Bouferrouk, A., Saulnier, J.-B., Smith, G. H., and Johanning, L. (2016). Field measurements of surface waves using a 5-beam ADCP. *Ocean Engineering*, 112:173–184.

Bowers, J. A., Morton, I. D., and Mould, G. I. (2000). Directional statistics of the wind and waves. *Applied Ocean Research*, 22(1):13–30.

Brodtkorb, P., Johannesson, P., Lindgren, G., Rychlik, I., Ryden, J., and Sjo, E. (2000). WAFO - a Matlab toolbox for analysis of random waves and loads. In *Proceedings of the10th International Offshore and Polar Engineering Conference, ISOPE, Seattle, USA*, volume 3, pages 343–350, Seattle.

Brown, J., Carrillo, L., Fernand, L., Horsburgh, K., Hill, A. E., Young, E., and Medler, K. (2003). Observations of the physical structure and seasonal jet-like circulation of the Celtic Sea and St. George's Channel of the Irish Sea. *Continental Shelf Research*, 23(6):533–561.

Caires, S. and Sterl, A. (2003). Validation of ocean wind and wave data using triple collocation. *Journal of Physical Oceanography*, 108(C3):1–16.

Caires, S. I. (2000). *Comparitive study of HF radar measurements and wave model hindcasts of waves in shallow waters*. PhD thesis, University of Sheffield.

Carrillo, L., Souza, A. J., Hill, A. E., Brown, J., Fernand, L., and Candela, J. (2005). Detiding ADCP data in a highly variable shelf sea: the Celtic Sea. *Journal of Atmospheric and Oceanic Technology*, 22(1):84–97.

Collins, C. O., Lund, B., Ramos, R., Drennan, W., and Graber, H. (2014). Wave measurement intercomparison and platform evaluation during the ITOP (2010) experiment. *Journal of Atmospheric and Oceanic Technology*, 31(10):2309–2329.

Coughlan, C. and Stips, A. (2015). Modelling the tides on the North West European Shelf. Technical report, European Commission. Joint Research Centre.

Cox, S., Miller, P., Embling, C., Scales, K., Bicknell, A., Hosegood, P., Morgan, G., Ingram, S., and Votier, S. (2016). Seabird diving behaviour reveals the functional significance of shelf-sea fronts as foraging hotspots. *Royal Society Open Science*, 3(9):160–317.

Crombie, D. D. (1955). Doppler spectrum of sea echo at 13.56 Mc./s. *Nature*, 175:642–643.

Dabbi, E. P., Haigh, I. D., Lambkin, D., Hernon, J., Williams, J. J., and Nicholls, R. J. (2015). Beyond significant wave height: A new approach for validating spectral wave models. *Coastal Engineering*, 100:11–25.

de Valk, C., Reniers, A., Atanga, J., Vizinho, A., and Vogelzang, J. (1999). Monitoring surface waves in coastal waters by integrating HF radar measurement and modelling. *Coastal Engineering*, 37(3-4):431–453.

Drennan, W. M., Graber, H. C., Hauser, D., and Quentin, C. (2003). On the wave age dependence of wind stress over pure wind seas. *Journal of Geophysical Research: Oceans*, 108(C3):8062.

Emery, W. J. and Thomson, R. E., editors (2001). *Data analysis methods in physical oceanography*. Elsevier Science, Amsterdam, 2nd edition.

Essen, H. H., Gurgel, K.-W., and Schlick, T. (1999). Measurement of ocean wave height and direction by means of HF radar: an empirical approach. *Deutsche Hydrographische Zeitschrift*, 51(4):369–383.

Evans, M. and Georges, T. M. (1979). Coastal Ocean Dynamics Radar (CODAR) NOAA's surface current mapping system. Technical report, Wave propagation laboratory. NOAA.

Folley, M., Cornett, A., Holmes, B., Liria, P., and Lenee-Bluhm, P. (2012). Standardising resource assessment for wave energy converters. *4th International Conference on Ocean Energy*, pages 1–7.

Forget, P., Broche, P., and Maistre, J. C. D. (1981). Sea state frequency features observed by ground wave HF Doppler radar. *Radio Science*, 16(5):917–925.

Gomez, R., Helzel, T., Wyatt, L., Lopez, G., Conley, D., Thomas, N., Smet, S., and Sicot, G. (2015). Estimation of wave parameters from HF radar using different methodologies and compared with wave buoy measurements at the Wave Hub. *MTS/IEEE OCEANS 2015 - Genova: Discovering Sustainable Ocean Energy for a New World.*

Gonella, J. (1972). A rotary-component method for analysing meteorological and oceanographic vector time series. *Deep Sea Research*, 19:833–846.

Graber, H. C. (2005). The shoaling waves experiment. *Journal of Atmospheric and Oceanic Technology*, 22(7):797.

Graber, H. C., Haus, B. K., Chapman, R. D., and Shay, L. K. (1997). HF radar comparisons with moored estimates of current speed and direction: Expected differences and implications. *Journal of Geophysical Research*, 102(C8):18749–18766.

Graber, H. C., Terray, E. A., Donelan, M. A., Drennan, W. M., Leer, J. V., and Peters, D. B. (2000). ASIS – A new air-sea interaction spar buoy: design and performance at sea. *Journal of Atmospheric and Oceanic Technology*, 17:708–720.

Guedes Soares, C. and de Pablo, H. (2006). Experimental study of the transformation of wave spectra by a uniform current. *Ocean Engineering*, 33(3-4):293–310.

Gurgel, K.-W. and Antonischki, G. (1997). Remote Sensing of Surface Currents and Waves by the HF Radar WERA. In *Proceedings of the Seventh IEE Conference on Electronic Engineering in Oceanography*, pages 211–217.

Gurgel, K.-W., Antonischki, G., Essen, H. H., and Schlick, T. (1999a). Wellen Radar (WERA): A new ground-wave HF radar for ocean remote sensing. *Coastal Engineering*, 37(3-4):219–234.

Gurgel, K.-W., Antonischki, G., and Schlick, T. (1998). HF radar systems for wave and current measurement. In *Proceedings of Oceanology'98 conference*, pages 423–433.

Gurgel, K.-W., Essen, H. H., and Kingsley, S. (1999b). High-frequency radars : physical limitations and recent developments. *Coastal Engineering*, 37:201–218.

Gurgel, K.-W., Essen, H.-H., and Schlick, T. (2006). An empirical method to derive ocean waves from second-order Bragg scattering: Prospects and limitations. *IEEE Journal of Oceanic Engineering*, 31(4):804–811.

Gurgel, K.-W. and Schlick, T. (2007). Compatibility of FMCW modulated HF surface wave radars with radio services. In *Proceedings of the International Radar Symposium, IRS 2007*, pages 255–258, Cologne.

Haller, M. C. and Özkan-Haller, T. (2007). Waves on unsteady currents. *Physics of Fluids*, 19(12):1–12.

Harris, F. (1978). On the use of windows for harmonic analysis with the Discrete Fourier Transform. In *Proceedings of the IEEE*, volume 66, pages 172–204.

Hashemi, M. R. and Neill, S. P. (2014). The role of tides in shelf-scale simulations of the wave energy resource. *Renewable Energy*, 69:300–310.

Hashimoto, N. (1997). *Analysis of the directional wave spectra from field data*, volume 3. World Scientific.

Hashimoto, N. and Tokuda, M. (1999). A Bayesian approach for estimation of directional wave spectra with HF radar. *Coastal Engineering Journal*, 41(02):137–149.

Hasselmann, K. (1971). Determination of ocean wave spectra from Doppler radio return from the sea surface. *Nature Physical Science*, 229:16–17.

Haus, B. K. (2007). Surface current effects on the fetch-limited growth of wave energy. *Journal of Geophysical Research*, 112:C03003.

Haus, B. K., Ramos, R. J., Graber, H. C., Shay, L. K., and Hallock, Z. R. (2006). Remote observation of the spatial variability of Surface waves interacting with an estuarine outflow. *IEEE Journal of Oceanic Engineering*, 31(4):835–849.

Haus, B. K., Shay, L. K., Work, P. A., Voulgaris, G., Ramos, R. J., and Martinez-Pedraja, J. (2010). Wind speed dependence of single-site wave-height retrievals from high-frequency radars. *Journal of Atmospheric and Oceanic Technology*, 27(8):1381–1394.

Herbers, T. H. C. and Lentz, S. J. (2009). Observing directional properties of ocean swell with an Acoustic Doppler Current Profiler (ADCP). *Journal of Atmospheric and Oceanic Technology*, 27:210–225.

Heron, M. L. and Rose, R. (1986). On the application of HF ocean radar to the observation of temporal and spatial changes in wind direction. *IEEE Journal of Oceanic Engineering*, 11(2).

Heron, S. F. and Heron, M. L. (1998). A comparison of algorithms for extracting significant wave height from HF radar ocean backscatter spectra. *Journal of Atmospheric and Oceanic Technology*, 15(5):1157–1163.

Hill, A. E., Brown, J., Fernand, L., Holt, J., Horsburgh, K. J., Proctor, R., Raine, R., and Turrell, W. R. (2008). Thermohaline circulation of shallow tidal seas. *Geophysical Research Letters*, 35(11):5–9.

Hisaki, Y. (1996). Nonlinear inversion of the integral equation to estimate ocean wave spectra from HF radar. *Radio Science*, 31(1):25–39.

Hisaki, Y. (2002). Short-wave directional properties in the vicinity of atmospheric and oceanic fronts. *Journal of Geophysical Research*, 107(C11):3188.

Hisaki, Y. (2015). Development of a HF radar inversion algorithm for spectrum estimation (HIAS). *Journal of Geophysical Research: Oceans*, 120:1725–1740.

Holthuijsen, L. (2007). *Waves in oceanic and coastal waters*. Cambridge University Press.

Hopkins, J., Elgar, S., and Raubenheimer, B. (2015). Observations and model simulations of wave-current interaction on the inner shelf. *Journal of Geophysical Research: Oceans*, 120:3261–3285.

Howarth, M. J. and Proctor, R. (1992). Ship ADCP measurements and tidal models of the North Sea. *Continental Shelf Research*, 12:601–623.

Howell, R. K. and Walsh, J. (1993). Measurement of ocean wave spectra using narrow-beam HF radar. *IEEE Journal of Oceanic Engineering*, 18(3):296–305.

Ingram, D., Smith, G., Bittencourt-Ferreira, C., and Smith, H. (2011). Protocols for the equitable assessment of marine energy converters. Technical report, University of Edimburg, School of Engineering.

IOOS (2015). Manual for real-time quality Control of in-situ surface wave data. Technical report, Integrated Ocean Observing System.

Ivonin, D. V., Shrira, V. I., and Broche, P. (2006). On the singular nature of the second-order peaks in HF radar sea echo. *IEEE Journal of Oceanic Engineering*, 31(4):751–767.

Jaffres, J. B. D. and Heron, M. L. (2011). Wave Climate in the southern Great Barrier Reef , Australia Evaluation of an Ocean HF Radar System and Wave-Watch3. In *Oceans 2011*.

Janssen, A., Abdalla, S., Hersbach, H., and Bidlot, J.-R. (2007). Error estimation of buoy, satellite, and model wave height data. *Journal of Atmospheric and Oceanic Technology*, 24:1665–1678.

Janssen, P. A. E. M. (2008). Progress in ocean wave forecasting. *Journal of Computational Physics*, 227:3572–3594.

Jones, B. (2000). A Numerical Study of Wave Refraction in Shallow Tidal Waters. *Estuarine, Coastal and Shelf Science*, 51:331–347.

Jonsson, I. G. (1990). Wave-current interactions. In Le Mehaute, B. and Hanes, D., editors, *The Sea: Ocean Engineering Science*, chapter 3, pages 65–120. B. John Wiley & Sons Inc., New York.

Kahma, K., Hauser, D., Krogstad, H. E., Lehner, S., Monbaliu, J., and Wyatt, L. R. (2005). *Measuring and Analysing the directional spectra of ocean waves.* EU COST Action 714, EUR 21367.

Krogstad, H. (1988). Maximum likelihood estimation of ocean wave spectra from general arrays of wave gauges. *Modelling, Identification and Control: A Norwegian Res. Bulletin*, 9:81–97.

Krogstad, H. E., Wolf, J., Thompson, S. P., and Wyatt, L. R. (1999). Methods for intercomparison of wave measurements. *Coastal Engineering*, 37:235–257.

Kuik, A. J., van Vledder, G. P., and Holthuijsen, L. H. (1988). A method for the routine analysis of pitch-and-roll buoy wave data. *Journal of Physical Oceanography*, 18:1020–1034.

Lazure, P. and Dumas, F. (2008). An external-internal mode coupling for a 3D hydrodynamical model for applications at regional scale (MARS). *Advances in Water Resources*, 31:233–250.

Lehner, S., Pleskachevsky, A., and Bruck, M. (2012). High-resolution satellite measurements of coastal wind field and sea state. *International Journal of Remote Sensing*, 33(23):7337–7360.

Li, J. G. and Saulter, A. (2012). Assessment of the updated Envisat ASAR ocean surface wave spectra with buoy and altimeter data. *Remote Sensing of Environment*, 126:72–83.

Lipa, B. and Barrick, D. E. (1980). Methods for the extraction of long-period ocean wave parameters from narrow beam HF Radar sea echo. *Radio Science*, 15:843–853.

Lipa, B. J. and Barrick, D. E. (1986). Extraction of sea state from HF radar sea echo: Mathematical theory and modeling. *Radio Science*, 21(1):81.

Lipa, B. J., Nyden, B., Barrick, D., and Kohut, J. (2008). HF radar sea-echo from shallow water. *Sensors*, 8(8):4611–4635.

Liu, A. K., Jackson, F. C., Walsh, E. J., and Peng, C. Y. (1989). A case study of wave-current interaction near an oceanic front. *Journal of Geophysical Research*, 94(C11):189–200.

Mackay, E. B. L. (2009). *Wave energy resource assessment*. PhD thesis, University of Southampton.

Maresca, J. W., Evans, M. W., and Georges, T. M. (1980). Measuring rms wave spectra using narrow-beam HF radar. *IEEE Journal of Oceanic Engineering*, 18:295–305.

Marmain, J., Molcard, A., Forget, P., Barth, A., and Ourmieres, Y. (2014). Assimilation of HF radar surface currents to optimize forcing in the northwestern Mediterranean Sea. *Nonlinear Processes in Geophysics*, 21:259–675.

Masson, D. (1996). A case study of wave-current interaction in a strong tidal current. *Journal of Physical Oceanography*, 26:359–372.

McColl, K. A., Vogelzang, J., Konings, A. G., Entekhabi, D., Piles, M., and Stoffelen, A. (2014). Extended triple collocation: Estimating errors and correlation

coefficients with respect to an unknown target. *Geophysical Research Letters*, 41(17):6229–6236.

Middleditch, A. (2006). *Spectral analysis in high frequency radar oceanography.* PhD thesis, University of Sheffield.

Middleditch, A. (2013). Spatiotemporal spectral averaging of High-Frequency radar wave data. Technical Report April, ACORN, University of Western Australia.

Miller, P. (2009). Composite front maps for improved visibility of dynamic sea-surface features on cloudy SeaWiFS and AVHRR data. *Journal of Marine Systems*, 78(3):327–336.

Mori, N., Suzuki, T., and Kakuno, S. (2007). Noise of acoustic Doppler velocimeter data in bubbly flows. *Journal of Engineering Mechanics*, 133(1):122–125.

OESEA3 (2016). UK Offshore Energy Strategic Environmental Assessment 3 (OE-SEA3) - Appendix 1F: Climate and meteorology. Technical report, Department of Energy and Climate change.

O'Reilly, W. C., Herbers, T. H. C., Seymour, R. J., and Guza, R. T. (1996). A comparison of directional buoy and fixed platform measurements of Pacific swell. *Journal of Atmospheric and Oceanic Technology*, 13(1):231–238.

Pawlowicz, R., Beardsley, B., and Lentz, S. (2002). Classical tidal harmonic analysis including error estimates in MATLAB using T_TIDE. *Computers and Geosciences*, 28:929–937.

Peregrine, D. H. (1976). Interaction of water waves and currents. *Advances in Applied Mechanics*, 16:9–117.

Pettersson, H., Graber, H. C., Hauser, D., Quentin, C., Kahma, K., Drennan, W. M., and Donelan, M. A. (2003). Directional wave measurements from three

wave sensors during the FETCH experiment. *Journal of Geophysical Research*, 108(C3):8061.

Pingree, R. D. (1975). The advance and retreat of the thermocline on the continental shelf. *Journal of the Marine Biological Association of the United Kingdom*, 55:965–974.

Pingree, R. D. (1978). Cyclonic eddies and cross-frontal mixing. *Journal of the Marine Biological Association of the United Kingdom*, 58:955–963.

Pingree, R. D. (1980). Physical oceanography of the Celtic Sea and English Channel. In Banner, F., Collins, M., and Massie, K., editors, *The North-West European shelf seas : the sea bed and the sea in motion. 2, Physical and chemical oceanography, and physical resources*, chapter Chapter 13, pages 415–463. Elsevier Oceanography Series, Amsterdam.

Pingree, R. D. and Griffiths, D. K. (1978). Tidal fronts on the shelf seas around the British Isles. *Journal of Geophysical Research*, 83(C9):4615–4622.

Pingree, R. D. and Maddock, L. (1985). Rotary currents and residual circulation around banks and islands. *Deep Sea Research Part A, Oceanographic Research Papers*, 32(8):929–947.

Prandle, D. (1987). The fine-structure of nearshore tidal and residual circulations revealed by HF radar surface current measurements. *Journal of Physical Oceanography*, 17:231–245.

Ramos, R. J. (2006). *Analysis of wave energy evolution using wavelet transforms*. PhD thesis, University of Miami.

Ramos, R. J., Graber, H. C., and Haus, B. K. (2009). Observation of wave energy evolution in coastal areas using HF radar. *Journal of Atmospheric and Oceanic Technology*, 26(9):1891–1909.

Rapizo, H., Waseda, T., Babanin, A. V., and Toffoli, A. (2016). Laboratory experiments on the effects of a variable current field on the spectral geometry of water waves. *Journal of Physical Oceanography*, 46:2695–2717.

Rayleigh, J. (1877). *The theory of sound*. MacMillan, London.

Rice, S. O. (1951). Reflection of electromagnetic waves from slightly rough surfaces. *Communications on Pure and Applied Mathematics*, 4:351.

Ris, R. C. and Holthuijsen, L. H. (1996). Spectral modeling of current induced wave-blocking. In *Proceedings of the 25th International Conference on Coastal Engineering, Orlando*, pages 1246–1254. ASCE.

Rogers, W. E., Wittmann, P. A., Wang, D. W. C., Clancy, R. M., and Hsu, Y. L. (2005). Evaluations of global wave prediction at the Fleet Numerical Meteorology and Oceanography Center. *Weather and Forecasting*, 20(5):745–760.

Saha, S., Moorthi, S., Pan, H.-L., Wu, X., Wang, J., Nadiga, S., Tripp, P., Kistler, R., Woollen, J., Behringer, D., Liu, H., Stokes, D., Grumbine, R., Gayno, G., Wang, J., Hou, Y.-T., Chuang, H.-y., Juang, H.-M. H. a. J. S., Iredell, M., Treadon, R., Kleist, D., Delst, P. V., Keyser, D., Derber, J., Ek, M., Meng, J., Wei, H., Yang, R., Lord, S., van den Dool, H., Kumar, A., Wang, W., Long, C., Chelliah, M., Xue, Y., Huang, B., Schemm, J.-K., Ebisuzaki, W., Lin, R., Xie, P., Chen, M., Zhou, S., Higgins, W., Zou, C.-Z., Liu, Q., Chen, Y., Han, Y., Cucurull, L., Reynolds, R. W., Rutledge, G., and Goldberg, M. (2010). The NCEP Climate Forecast System Reanalysis. *Bulletin of the American Meteorological Society*, 91:1015–1057.

Saruwatari, A., Ingram, D. M., and Cradden, L. (2013). Wave-current interaction effects on marine energy converters. *Ocean Engineering*, 73:106–118.

Saulnier, J. B., Clment, A., Falco, A. F. D. O., Pontes, T., Prevosto, M., and Ricci, P. (2011). Wave groupiness and spectral bandwidth as relevant parameters for the performance assessment of wave energy converters. *Ocean Engineering*, 38(1):130–147.

Saulter, A. (2011). Assessment of significant wave height in UK coastal waters 2011 update: report for Maritime and Coastguard Agency research proposal RP626. Technical report, Met Office, Devon.

Savidge, D., Amft, J., Gargett, A., Archer, M., Conley, D., Voulgaris, G., Wyatt, L., and Gurgel, K.-W. (2011). Assessment of WERA long-range HF-radar performance from the user's perspective. In *2011 IEEE/OES/CWTM 10th Working Conference on Current, Waves and Turbulence Measurement, CWTM 2011*, pages 31–38.

Shearman, E. and Moorhead, M. (1988). PISCES: a coastal ground wave HF radar for current, wind and wave mapping to 200 km ranges. In *IEEE International Geoscience and Remote Sensing Symposium (IGARSS'88)*, pages 773–776.

Shen, C., Gill, E., and Huang, W. (2013). Extraction of swell parameters from simulated noisy HF radar signals. In *IEEE National Radar Conference - Proceedings*.

Shields, M., Woolf, D., Grist, E., Kerr, S., Jackson, A., Harris, R., Bell, M., Beharie, R., Want, A., Osalusi, E., Gibb, S., and Side, J. (2011). Marine renewable energy: The ecological implications of altering the hydrodynamics of the marine environment. *Ocean Coastal Management*, 24:2–9.

Simpson, J. and Hunter, J. R. (1974). Fronts in the Irish Sea. *Nature*, 250:404–406.

Sova, M. G. (1995). *The sampling variability and the validation of high frequency radar measurements of the sea surface*. PhD thesis, University of Sheffield.

Strong, B., Brumley, B., Terray, E., and Stone, G. (2000). The performance of ADCP-derived directional wave spectra and comparison with other independent measurements. In *OCEANS 2000 MTS/IEEE*, volume 2, pages 1195–1203.

SWRDA (2006). Wave Hub development and design phase coastal processes study report. Technical report, South West of England Regional Development Agency.

Tamura, H., Waseda, T., Miyazawa, Y., and Komatsu, K. (2008). Current-induced modulation of the ocean wave spectrum and the role of nonlinear energy transfer. *Journal of Physical Oceanography*, 38:2662–2684.

Taylor, K. E. (2001). Summarizing multiple aspects of model performance in a single diagram. *Journal of Geophysical Research: Atmospheres*, 106(7):7183–7192.

Tolman, H. L. (1990). The influence of unsteady depths and currents of tides on wind-wave propagation in shelf seas. *Journal of Physical Oceanography*, 20:1166–1174.

Tolman, H. L. (1991). Effects of tides and storm surges on North Sea wind waves. *Journal of Physical Oceanography*, 21:766–781.

Toro, V. G., Ocampo-Torres, F., Osuna, P., Garcia-Nava, H., Flores-Vidal, X., and Durazo, R. (2014). Analysis of fetch-limited wave growth using high-frequency radars in the Gulf of Tehuantepec. *Ciencias Marinas*, 40(2):113–132.

Van der Westhuysen, A. J. (2012). Spectral modeling of wave dissipation on negative current gradients. *Coastal Engineering*, 68:17–30.

Venugopal, V., Davey, T., Smith, H., Smith, G., Holmes, B., Barret, S., Prevosto, M., Maisondieu, C., Cavaleri, L., Bertotti, L., Lawrence, J., and Girard, F. (2011). Deliverable D2.2. Wave and tidal resource characterisation. Technical report, EquiMar.

Violante-Carvalho, N., Ocampo-Torres, F. J., and Robinson, I. S. (2004). Buoy observations of the influence of swell on wind waves in the open ocean. *Applied Ocean Research*, 26:49–60.

Voulgaris, G., Haus, B. K., Work, P., Shay, L. K., Seim, H. E., Weisberg, R. H., and Nelson, J. R. (2008). Waves initiative within SEACOOS. *Marine Technology Society Journal*, 42(3):68–80.

Wait, J. R. (1966). Theory of HF ground wave backscatter from sea waves. *Journal of Geophysical Research*, 71:4839–4842.

Waters, J., Wyatt, L. R., Wolf, J., and Hines, A. (2013). Data assimilation of partitioned HF radar wave data into Wavewatch III. *Ocean Modelling*, 72(August):17–31.

Wolf, J. and Prandle, D. (1999). Some observations of wave current interaction. *Coastal Engineering*, pages 471–485.

Work, P. A. (2008). Nearshore directional wave measurements by surface-following buoy and acoustic Doppler current profiler. *Ocean Engineering*, 35:727–737.

Wyatt, L. R. (1988). Significant waveheight measurement with HF radar. *International Journal of Remote Sensing*, 9(6):1087–1095.

Wyatt, L. R. (1990). A relaxation method for integral inversion applied to HF radar measurement of the ocean wave directional spectrum. *International Journal of Remote Sensing*, 11(8):1481–1494.

Wyatt, L. R. (1991). High-frequency radar measurements of the ocean wave-directional spectrum. *IEEE Journal of Oceanic Engineering*, 16(1):163–169.

Wyatt, L. R. (2000). Limits to the inversion of HF radar backscatter for ocean wave measurement. *Journal of Atmospheric and Oceanic Technology*, 17:1651–1665.

Wyatt, L. R. (2002). An evaluation of wave parameters measured using a single HF radar system. *Canadian Journal of Remote Sensing*, 28(2):205–218.

Wyatt, L. R. (2007). Wave and tidal power measurement using HF radar. In *Oceans 2007-Europe*, pages 1–5.

Wyatt, L. R. (2012). Use of HF radar for marine renewable applications. In *Ocean. 2012 MTS/IEEE Yeosu Living Ocean Coast - Divers. Resour. Sustain. Act.*

Wyatt, L. R., Burrows, G. D., and Moorhead, M. D. (1985). An assessment of a FMICW ground-wave radar system for ocean wave studies. *International Journal of Remote Sensing*, 6(1):275–282.

Wyatt, L. R. and Green, J. (2002). The availability and accuracy of HF radar wave measurements. In *IEEE International Geoscience and Remote Sensing Symposium*, volume 1, pages 515–517.

Wyatt, L. R., Green, J. J., Gurgel, K.-W., Nieto Borge, J. C., Reichert, K., Hessner, K., Günther, H., Rosenthal, W., Saetra, O., and Reistad, M. (2003). Validation and intercomparisons of wave measurements and models during the EuroROSE experiments. *Coastal Engineering*, 48(1):1–28.

Wyatt, L. R., Green, J. J., and Middleditch, A. (2008). Directional spectra comparisons between HF radar and a wave model. In *Proceedings of the IEEE Working Conference on Current Measurement Technology*, pages 211–216.

Wyatt, L. R., Green, J. J., and Middleditch, A. (2009). Signal sampling impacts on HF radar wave measurement. *Journal of Atmospheric and Oceanic Technology*, 26(4):793–805.

Wyatt, L. R., Green, J. J., and Middleditch, A. (2011). HF radar data quality requirements for wave measurement. *Coastal Engineering*, 58(4):327–336.

Wyatt, L. R., Green, J. J., Middleditch, A., Moorhead, M. D., Howarth, J., Holt, M., and Keogh, S. (2006). Operational wave, current, and wind measurements with the pisces HF radar. *IEEE Journal of Oceanic Engineering*, 31(4):819–834.

Wyatt, L. R., Liakhovetski, G., Graber, H. C., and Haus, B. K. (2005). Factors affecting the accuracy of SHOWEX HF radar wave measurements. *Journal of Atmospheric and Oceanic Technology*, 22(7):847–859.

Wyatt, L. R., Thompson, S. P., and Burton, R. R. (1999). Evaluation of high frequency radar wave measurement. *Coastal Engineering*, 37(3-4):259–282.

Zhang, J., Walsh, J., and Gill, E. (2012). Inherent limitations in HF radar remote sensing based on Bragg scattering from the ocean surface. *IEEE Journal of Oceanic Engineering*, 37(3):395–406.

Zhou, H. and Wen, B. (2014). Observations of the second-harmonic peaks from the sea surface with high-frequency radars. *IEEE Geoscience and Remote Sensing Letters*, 11(10):1682–1686.

Peer-reviewed work

Lopez, G., D. Conley, and D. Greaves, 2016: Calibration, Validation, and Analysis of an Empirical Algorithm for the Retrieval of Wave Spectra from HF Radar Sea Echo. J. Atmos. Oceanic Technol., 33, 245261, doi: 10.1175/JTECH-D-15-0159.1.